Laser-based diagnostics for investigating soot formation in combustion processes

Mannazhi, MANU

2021

Document Version:
Publisher's PDF, also known as Version of record

Laser-based diagnostics for investigating soot formation in combustion processes

MANU MANNAZHI
DEPARTMENT OF PHYSICS | FACULTY OF ENGINEERING | LUND UNIVERSITY

Laser-based diagnostics for investigating soot formation in combustion processes

Laser-based diagnostics for investigating soot formation in combustion processes

Manu Mannazhi

LUND
UNIVERSITY

DOCTORAL DISSERTATION

by due permission of the Faculty of Engineering, Lund University, Sweden.
To be defended at Rydbergsalen, Fysicum, Professorsgatan 1,
Friday, 21st May 2021 at 9:15 AM

Faculty opponent

Dr. Klaus-Peter Geigle, German Aerospace Center, Institute of Combustion Technology, Stuttgart, Germany

Organization LUND UNIVERSITY Division of Combustion Physics Department of Physics Box 118, SE-22100 Lund, Sweden	**Document name**: **DOCTORAL DISSERTATION** **Date of issue** April 26, 2021
Author: **Manu Mannazhi**	Sponsoring organization

Title and subtitle: Laser-based diagnostics for investigating soot formation in combustion processes

Abstract

In this work, laser-based diagnostic techniques were developed and applied to investigate soot formation in small-scale laboratory burners as well as in practical combustion devices.

Quantitative 2D laser-induced incandescence (LII) measurements often use a cylindrical lens to shape the beam and illuminate the planar region of interest. The varying laser fluence and sheet width in the imaged flame region created due to this focusing was found to introduce significant bias in the 2D LII signal distributions, especially for short focal length lenses combined with long imaged regions. Experimental data were recorded with variations in laser fluence and detector gate, which were reproduced through numerical simulations using a heat-and-mass-transfer-based LII model. It was shown that adequate choices of experimental parameters could minimize bias in the 2D LII signal distribution.

Combined measurements using LII and extinction as well as laser-induced fluorescence of polycylic aromatic hydrocarbons (PAH-LIF) were applied to characterize soot formation in methane-air diffusion flames at elevated pressures. A special focus was on the evaluation of optical properties of soot at various spatial locations in the flames through the analysis of LII fluence curves. The absorption function $E(m)$ was found to increase strongly with increase in pressure at the position of maximum soot volume fraction (f_v), and also along the centreline of the flame until the position of maximum f_v. It was demonstrated that an assumption of constant $E(m)$ in 2D LII measurements in sooting diffusion flames leads to large uncertainties in evaluated soot volume fractions.

Previous studies have shown that addition of potassium chloride (KCl) reduces soot concentration and primary particle size. As PAHs are precursors of soot, this work focused on the influence of potassium and sodium salt additives on PAH formation, and measurements were primarily made using PAH-LIF and elastic light scattering (ELS). Using different combinations of excitation and fluorescence wavelengths, the detected fluorescence could be classified to originate from two groups: small PAHs (~ 2-3 rings) and large PAHs ($\gtrsim$ 4 rings). Addition of potassium and sodium salts were found to have no observable influence on the formation of smaller PAHs. However, the concentration of larger PAHs decreased in the sooting flame region with the addition of these salts, where the largest effect was seen for potassium salts. Additionally, different salts of potassium (or sodium) showed similar fluorescence and scattering response, thus showing that it is the metal ion which is primarily responsible for the influence on PAH concentrations observed in this study.

Laser diagnostic techniques have also been applied in an optical diesel engine to study the effects of injector aging and oxygenated fuel additive tripropylene glycol monomethyl ether (TPGME) on spray and soot formation as well as soot oxidation. Studies in the literature have shown that aging of injectors adversely affects diesel engine combustion. TPGME has also been found to lower soot emissions. The spray and soot formation were investigated using high-speed imaging measurements of Mie scattering and natural luminosity, whereas late cycle soot oxidation was studied using semi-quantitative 2D LII and extinction measurements. Aged injector showed higher fuel injection rates resulting in higher soot formation and faster soot oxidation, predominantly at low load conditions. The fuel with added TPGME produced lesser soot in the cycle and showed faster soot oxidation rates.

Key words: Soot, laser-induced incandescence, extinction, combustion, additives, laser-induced fluorescence, polycyclic aromatic hydrocarbons

Classification system and/or index terms (if any)

Supplementary bibliographical information	**Language**: English
ISSN and key title 1102-8718	**ISBN** 978-91-7895-847-4 (print) 978-91-7895-848-1 (pdf)

Recipient's notes	**Number of pages 111**	Price
	Security classification	

Signature 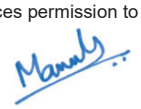 Date 2021-04-12

Laser-based diagnostics for investigating soot formation in combustion processes

Manu Mannazhi

LUND
UNIVERSITY

Cover photo by Manu Mannazhi

Department of Physics
Faculty of Engineering
Lund University

ISBN 978-91-7895-847-4 (print)
ISBN 978-91-7895-848-1 (pdf)
ISSN 1102-8718
ISRN LUTFD2/TFCP-230-SE

Printed in Sweden by Media-Tryck, Lund University
Lund 2020

Dedication:

അമ്മ, അച്ഛൻ

Table of Contents

Abstract

In this work, laser-based diagnostic techniques were developed and applied to investigate soot formation in small-scale laboratory burners as well as in practical combustion devices.

Quantitative 2D laser-induced incandescence (LII) measurements often use a cylindrical lens to shape the beam and illuminate the planar region of interest. The varying laser fluence and sheet width in the imaged flame region created due to this focusing was found to introduce significant bias in the 2D LII signal distributions, especially for short focal length lenses combined with long imaged regions. Experimental data were recorded with variations in laser fluence and detector gate, which were reproduced through numerical simulations using a heat-and-mass-transfer-based LII model. It was shown that adequate choices of experimental parameters could minimize bias in the 2D LII signal distribution.

Combined measurements using LII and extinction as well as laser-induced fluorescence of polycylic aromatic hydrocarbons (PAH-LIF) were applied to characterize soot formation in methane-air diffusion flames at elevated pressures. A special focus was on the evaluation of optical properties of soot at various spatial locations in the flames through the analysis of LII fluence curves. The absorption function $E(m)$ was found to increase strongly with increase in pressure at the position of maximum soot volume fraction (f_v), and also along the centreline of the flame until the position of maximum f_v. It was demonstrated that an assumption of constant $E(m)$ in 2D LII measurements in sooting diffusion flames leads to large uncertainties in evaluated soot volume fractions.

Previous studies have shown that addition of potassium chloride (KCl) reduces soot concentration and primary particle size. As PAHs are precursors of soot, this work focused on the influence of potassium and sodium salt additives on PAH formation, and measurements were primarily made using PAH-LIF and elastic light scattering (ELS). Using different combinations of excitation and fluorescence wavelengths, the detected fluorescence could be classified to originate from two groups: small PAHs (~ 2-3 rings) and large PAHs ($\gtrsim$ 4 rings). Addition of potassium and sodium

salts were found to have no observable influence on the formation of smaller PAHs. However, the concentration of larger PAHs decreased in the sooting flame region with the addition of these salts, where the largest effect was seen for potassium salts. Additionally, different salts of potassium (or sodium) showed similar fluorescence and scattering response, thus showing that it is the metal ion which is primarily responsible for the influence on PAH concentrations observed in this study.

Laser diagnostic techniques have also been applied in an optical diesel engine to study the effects of injector aging and oxygenated fuel additive tripropylene glycol monomethyl ether (TPGME) on spray and soot formation as well as soot oxidation. Studies in the literature have shown that aging of injectors adversely affects diesel engine combustion. TPGME has also been found to lower soot emissions. The spray and soot formation were investigated using high-speed imaging measurements of Mie scattering and natural luminosity, whereas late cycle soot oxidation was studied using semi-quantitative 2D LII and extinction measurements. Aged injector showed higher fuel injection rates resulting in higher soot formation and faster soot oxidation, predominantly at low load conditions. The fuel with added TPGME produced lesser soot in the cycle and showed faster soot oxidation rates.

Popular Summary

Since the beginning of the industrial revolution, fossil fuels such as coal, oil and natural gas have been in the forefront of various sources of energy. However, concerns about the emissions from these fossil fuel-based combustion systems causing atmospheric pollution and global warming started to form a few decades ago, and these concerns have been intensified as time progressed. Out of the various emission products from a combustion system, carbon dioxide and soot are two of the main contributors of global warming. In this thesis, we focus on soot. Soot particles are extremely small carbon-based nanoparticles with sizes often smaller than one hundredth of the thickness of a hair. They are formed due to the incomplete combustion of hydrocarbon fuels (fuels primarily composed of carbon and hydrogen) such as fossil fuels, biomass, etc. The yellow colour in a candle flame is coming from heated soot particles in the flame. Soot upon inhalation, has also been found to be detrimental to human health. Since the technological solutions alternate to combustion systems can not satisfy the growing energy demands of the world now, we must find ways to improve combustion systems in reducing their emissions. Carbon-neutral combustion alternatives − such as biofuels − must be further improved, for example regarding the reduction of soot emissions.

Developing accurate measurement or diagnostic techniques is an important step in understanding any process. Optical diagnostic techniques such as laser-based diagnostic techniques use the emission or absorption of light by the system to study it. Although optical diagnostic techniques usually offer high spatial and temporal resolutions, they can only be performed in open systems or in systems with optical access (transparent components). Laser-induced incandescence (LII) is one of the main optical diagnostic technique used for studying soot formation, where one can obtain soot concentrations upon combining with other techniques such as laser extinction or elastic light scattering (ELS). LII can also be used for measuring different properties of the soot such as primary particle size, optical properties (how soot interacts with light), etc. For this purpose, a heat and mass transfer based numerical model called the LII model is commonly used, in combination with the measurements. Techniques such as laser extinction, ELS, laser-induced

fluorescence of polycyclic aromatic hydrocarbon molecules (PAHs, considered as the precursors of soot), etc. are some of the other diagnostic techniques used in the works reported in this thesis.

A fundamental study on improving quantitative two-dimensional (2D) LII measurements based on focusing of a laser beam or sheet was performed. Experimental measurements and supporting calculations using the numerical LII model showed that it is important to have a large value of the ratio between the focal length and the length of the imaging region. Another fundamental study related to soot formation at high pressures was performed to study how soot evolves from less light absorbing less mature soot to more mature soot with higher light absorption efficiency. Using experimental data together with simulations using the LII model, it was found that for methane-air diffusion flames, soot maturity increased with pressure and with height above the burner surface. Another study relevant for biomass (renewable fuel based on plant or animal material) combustion using PAH-LIF and ELS showed that addition of potassium chloride in a flame reduced the formation of larger PAHs. Further investigations using different salts of potassium (K) and sodium (Na) showed that only the metal ions in the salt, K^+ and Na^+ in our cases, significantly influence the PAH and soot formation process. Applied measurements of LII and extinction combined with high-speed imaging of flame luminosity and scattering was performed in an optical diesel engine (one with transparent components). The effects of the fuel injection system in the car getting old was studied, and it was found that aging of injectors result in higher soot formation and emissions. Additionally, the effect of the fuel additive TPGME was studied, which showed lesser soot formation and faster soot oxidation.

Although several interesting results discussed here have shone some light into the enigmatic topic of soot formation, some of these results pose interesting questions to explore further. Laser diagnostic techniques such as the ones mentioned here certainly has a role to play in helping to find those answers.

Populärvetenskaplig Sammanfattning

Sedan början av den industriella revolutionen har fossila bränslen som kol, olja och naturgas varit dominerande bland energikällorna i världen. Utsläppen från fossilbränslebaserade förbränningssystem orsakar luftföroreningar och bidrar till global uppvärmning. Koldioxid och sotpartiklar är två förbränningsprodukter som starkt bidrar till den globala uppvärmningen. I denna avhandling fokuserar vi på sot. Sotpartiklar är extremt små kolbaserade nanopartiklar med storlekar som oftast är mindre än en hundradel av hårets tjocklek. De bildas på grund av ofullständig förbränning av kolvätebränslen (bränslen huvudsakligen sammansatta av kol och väte) såsom fossila bränslen, biomassa, etc. Den gula färgen i en ljuslåga kommer från uppvärmda sotpartiklar i lågan. Om sotet inte förbränns i lågan utan når omgivande luft så kan det vid inandning vara skadligt för människors hälsa. Även om fossila bränslen med tiden kommer att fasas ut och ersättas, så kommer andra förbränningsalternativ såsom biobränslen att vara betydelsefulla även i framtiden för att täcka det snabbt växande energibehovet. Även biobränsleförbränning producerar sot och dessa förbränningssystem måste förbättras för att minska utsläppen.

Att använda noggranna mättekniker är ett viktigt steg för att förstå en process. Optiska mättekniker, t.ex. laserbaserade tekniker, använder ljus för att studera ett system. Dessa tekniker påverkar vanligtvis inte systemet som studeras och möjliggör ofta hög tids- och rumsupplösning. Det krävs dock optisk access till mätområdet, vilket betyder att slutna system såsom motorer måste göras optiskt tillgängliga genom att ersätta motordelar med transparenta glaskomponenter.

Laserinducerad inkandescens (LII) är en av de viktigaste optiska diagnostiska teknikerna som används för att studera sotbildning genom att kunna mäta sotkoncentrationer. I kombination med andra tekniker som mäter ljusabsorption och ljusspridning kan man också bestämma till exempel sotpartikelstorlekar. LII kan också användas för att mäta optiska egenskaper för partiklarna, dvs hur effektivt de kan absorbera och sprida ljus. En matematisk modell har använt för att simulera de mätresultat som erhållits med LII-tekniken, och god överensstämmelse har erhållits.

Samtliga här nämnda tekniker – LII, absorption och spridning – har använts i det experimentella arbetet presenterat i denna avhandling för att mäta egenskaper för sotpartiklar och få en ökad förståelse för sotbildningsprocesser. Även förstadierna till sotpartiklar, s.k. polycykliska aromatiska kolväten (PAHs), kan studeras med lasermätteknik. I avhandlingsarbetet har laserinducerad fluorescens (LIF) använts för att mäta koncentrationer av två olika storleksklasser av PAHs.

En grundläggande laboratoriestudie utfördes om hur förbättring av kvantitativa tvådimensionella LII-mätningar kan göras då laserstrålen fokuseras till ett laserark. Såväl experimentella mätningar som den numeriska modellen visade att det är viktigt att ha ett stort värde på förhållandet mellan fokuseringslinsens brännvidd och längden på avbildningsregionen. En annan grundläggande studie relaterad till sotbildning vid höga tryck utfördes för att studera hur sot utvecklas från mindre moget sot till mer ljusabsorberande svart sot. Utifrån experimentella mätningar och den numeriska LII-modellen framkom att för metan-luftdiffusionslågor ökade sotmognaden med såväl tryck som höjd över brännarytan. En annan studie undersökte hur tillsatser av kalium- och natriumsalter påverkade bildningen av polycykliska aromatiska kolväten (PAHs), alltså förstadierna till sotpartiklar. Med hjälp av LIF observerades att framförallt tillsatser av kalium ledde till en lägre koncentration av större PAHs, medan koncentrationen av mindre PAHs verkade vara opåverkad. Denna studie är relevant för förbränning av biomassa då dessa bränslen innehåller kalium- och natriumsalter i varierande grad. Tillämpade optiska mätningar utfördes i en optisk dieselmotor (med transparenta komponenter). Teknikerna som användes var höghastighetsavbildning av flamemission och ljusspridning och LII kombinerat med ljusabsorption. Resultaten visade att åldrande injektorer resulterade i högre sotbildning i motorcylindern. Dessutom studerades effekten av bränsletillsatsen, TPGME, och denna tillsats ledde till mindre sotbildning och snabbare sotoxidation.

Även om flera intressanta resultat har presenterats här finns det fortfarande många obesvarade frågor i det gåtfulla ämnet sotbildning. Optiska mättekniker är också fortsättningsvis viktiga för att finna dessa svar.

Nomenclature

B	Burner
BP320	Band-pass filter at 320 nm
BS	Beam splitter
c	Speed of light in vacuum (~ 3 x 10^8 m/s)
c_s	Heat capacity of soot particle
CAD	Crank angle degree
CW	Continuous wave (laser)
d_p	Primary particle diameter of soot
DM	Dichroic mirror
EGR	Exhaust gas recirculation
ELS	Elastic light scattering
EOI	End of injection
$E(m)$	Absorption function
F	Laser fluence
F	Optical filters
fps	Frames per second
FWHM	Full width at half maximum
$F(m)$	Refractive index function for scattering
f_v	Soot volume fraction
f500	Cylindrical lens with a focal length of +500 mm
f2000	Cylindrical lens with a focal length of +2000 mm (f1000 ≡ +1000 mm)
FM	Free molecular (regime)
G	Geometry-dependent heat transfer factor
$g(t)$	Normalised temporal distribution of the laser energy
h	Planck's constant (6.626 x 10^{-34} J-s)
HAB	Height above burner
HACA	Hydrogen-abstraction-carbon-addition (mechanism)
I_0	Intensity of reference beam
I_t	Intensity of transmitted beam
IMEPg	Gross indicated mean effective pressure
k	Imaginary part of the complex refractive index of soot
K_{ext}	Extinction coefficient
k_g	Thermal conductivity of the gas
Kn	Knudsen number
$K_{scatter}$	Scattering coefficient
L	Absorption length
LIF	Laser-induced fluorescence
LII	Laser-induced incandescence
LP385	Long-pass filter with cut-off wavelength at 385 nm
m	Complex refractive index of soot
M	Mass of the soot particle
M	Molar
N	Number density of soot
n	Real part of the complex refractive index of soot
N_p	Aggregate size
NL	Natural luminosity
OD	Optical density (filter)
P	Pressure
PD	Photodiode
PM	Particulate matter
ppm	Parts per million
ppb	Parts per billion
Q_{abs}	Heat transfer due to absorption
Q_{con}	Heat transfer due to conduction
Q_{rad}	Heat transfer due to radiation
Q_{sub}	Heat transfer due to sublimation
SOI	Start of injection
SP450	Short-pass filter - cut-off at 450 nm
SP425	Short-pass filter - cut-off at 425 nm
T	Temperature
T_g	Temperature of the gas
TDC	Top dead centre
TPGME	Tripropylene glycol monomethyl ether
U_{int}	Internal energy of soot particle
x	Thickness of the laser sheet

Greek symbols

α_T	Thermal accommodation coefficient	ρ_s	Density of soot particle
β	Mass accommodation coefficient	λ_{MFP}	Mean free path of gas molecules
γ	Ratio of specific heats ($\gamma = C_p/C_v$)	ρ_{sa}	Scattering to absorption ratio
δ_{FM}	Thickness of the free molecular regime	σ_{abs}	Absorption cross section
λ	Wavelength	σ_{sca}	Scattering cross section
		ϕ	Equivalence ratio
		Γ	Diffusion coefficient of soot vapour

List of Papers

I. **M. Mannazhi** and P.-E. Bengtsson, *Two-dimensional laser-induced incandescence for soot volume fraction measurements: Issues in quantification due to laser beam focusing*, Applied Physics B, (2020) 126:194.

II. **M. Mannazhi**, S. Török, J. Gao and P.-E. Bengtsson, *Soot maturity studies in methane-air diffusion flames at elevated pressures using laser-induced incandescence,* Proceedings of the Combustion Institute 38 (2021) 1217 – 1224.

III. **M. Mannazhi**, S. Bergqvist and P.-E. Bengtsson, *Influence of potassium chloride on PAH concentration during soot formation studied using laser-induced fluorescence*, Submitted to Combustion & Flame (Review process ongoing)

IV. X. Zhu, **M. Mannazhi**, N. Palazzo, P.-E. Bengtsson and Ö. Andersson, *High-speed imaging of spray formation and combustion in an optical engine: Effects of injector aging and TPGME as a fuel additive*, Energies 13 (12), 3105.

V. **M. Mannazhi**, X. Zhu, Ö. Andersson and P.-E. Bengtsson, *Soot oxidation studies in an optical diesel engine using laser-induced incandescence and extinction: the effects of injector ageing and fuel additive,* Submitted to SAE International Journal of Engines (Accepted for publication)

Related Work

RW-I. S. Török, V. B. Malmborg, J. Simonsson, A. Eriksson, J. Martinsson, **M. Mannazhi**, J. Pagels and P.-E. Bengtsson, *Investigation of the absorption Ångström exponent and its relation to physicochemical properties for mini-CAST soot*, Aerosol Science and Technology 2018, vol. 52, no. 7, 757–767.

RW-II. A. Gunnarsson, J. Simonsson, D. Bäckström, **M. Mannazhi**, P.-E. Bengtsson and Klas Andersson, *Radiative heat transfer modeling and in-situ diagnostics of soot in an 80 kw_{th} propane flame with varying feed-gas oxygen concentration*, Journal of Industrial & Engineering Chemistry Research 2018, 57, 36, 12288–12295

RW-III. J. Simonsson, A. Gunnarsson, **M. Mannazhi**, D. Bäckström, K. Andersson and P.-E. Bengtsson, *In-situ soot characterization of propane flames and influence of additives in a 100 kW oxy-fuel furnace using two-dimensional laser-induced incandescence*, Proceedings of the Combustion Institute 37 (2019) 833 – 840.

RW-IV. P. Tóth, C. Brackmann, Y. Ögren, **M. Mannazhi**, J. Simonsson, A. Sepman, P.-E. Bengtsson and Henrik Wiinikka, *Experimental and numerical study of biomass fast pyrolysis oil spray combustion: Advanced laser diagnostics and emission spectrometry*, Fuel 252, 125 – 134.

RW-V. N. Palazzo, M. Kögl, P. Bauer, **M. Mannazhi**, L. Zigan, F. J. T. Huber, S. Will, *Investigation of soot formation in a novel diesel fuel burner*, Energies 12 (10), 1993 (2019)

RW-VI. E. Fooladgar, C. Brackmann, **M. Mannazhi**, Y. Ögren, P.-E. Bengtsson, Henrik Wiinikka, Pál Tóth, *CFD modeling of pyrolysis oil combustion using finite rate chemistry*, Submitted to Fuel (Review process ongoing)

Author Contributions

Paper I. Experiments were planned by myself along with Per-Erik Bengtsson (PEB). I carried out the measurements, data evaluation and modelling. I was the main responsible for writing the manuscript with help from PEB.

Paper II. I planned the experiments with PEB. Jinlong Gao taught me the operating procedure of the high-pressure burner. I performed the measurements and data evaluation. I had several discussions with Sandra Török on the application of the numerical LII model. I wrote the manuscript with help from PEB, JG and ST.

Paper III. I planned the experiments with PEB and Saga Bergqvist (SB). Myself and SB performed the measurements. I performed the data evaluation and was responsible for the writing of the manuscript where PEB and SB helped in reviewing the manuscript.

Paper IV. Xinda Zhu (XZ), myself, Öivind Andersson (ÖA) and PEB planned the experiment. XZ and myself performed the experiments, where Natascia Palazzo was also part of some measurements. I was responsible for setting up the optical diagnostics part and XZ was responsible for operating the optical engine. XZ performed most of the data evaluation and was the main responsible for writing the paper. I also contributed to the data evaluation.

Paper V. Myself, XZ, ÖA and PEB planned the experiment. XZ and myself performed the experiments. I was responsible for the optical diagnostics part and XZ was responsible for operating the optical engine. I performed the major part of the data evaluation, with contributions from XZ. All the other authors contributed to the paper reviewing.

1 Introduction

From time immemorial, the enigma of combustion and flames have sparked human curiosity tremendously. The ability to tame fire and extract energy from it can be regarded as two of the main driving factors of human civilization. Discovery and use of fossil fuels such as coal, oil and natural gas for energy have also significantly improved the economy and life of a vast majority of the human population. However, in the past several decades, these processes have been found to have devastating side-effects [1]. Although humans have come a long way in mastering ways for sapping energy from combustion, there is still a lot to be done in terms of mitigating these shortcomings.

One of the main disadvantages of combustion systems based on hydrocarbon fuels such as fossil fuels is the production of unwanted emissions in the forms of various molecular species and particulate matter (PM). These harmful emissions commonly contain soot, carbon monoxide, unburned hydrocarbons, nitrogen oxides (NOx), etc., which have detrimental effects on human health and the climate [1-6]. Soot, which is the main topic of this thesis, is primarily composed of carbon and hydrogen, and is one of the most important components out of these harmful emissions. Other than fossil fuel-based combustion systems, atmospheric soot sources include forest fires, local field burning, waste incineration, wood-fired ovens, etc. Soot particles can be present as aerosols, and due to their small sizes (order of tens to hundreds of nanometers), these particles can be transported deep into the lungs when inhaled, and also penetrate the cells and circulatory system to cause asthma, lung cancer and cardiovascular diseases [5, 6]. Soot particles often have surface coatings consisting of polycyclic aromatic hydrocarbon molecules (PAHs), which are considered as the precursors of soot [7, 8]. PAHs are found to be carcinogenic and mutagenic to human cells [9].

In addition to the harmful effects on human health, soot particles are also destructive for the environment. They efficiently absorb light, are refractory, and are insoluble in water. Due to these properties, soot has also been found to be one of the main contributors of global warming along with carbon dioxide and methane. The

presence of these highly absorbing soot particles on polar ice caps has been causing the melting of ice at an alarming rate [2, 6]. However, soot particles are short-lived in the atmosphere, with lifetimes of the order of a few days to weeks [2]. As a result of this, a reduction of soot emissions can have an immediate impact in climate change.

Due to their harmful effects on human health and climate, we must get rid of fossil-fuel-based combustion systems very fast. Increased investments in more eco-friendly and renewable sources of energy such as solar, wind and hydropower have been made to reduce the environmental impact of fossil fuel-based combustion systems. In addition to these, there has been growing interest in biomass as one of the contributors in replacing fossil-fuels [10-12], although biomass combustion also generates soot emissions. Regardless of the presence of these alternates, the rate of consumption of fossil fuels has been increasing steadily in the past few decades [13, 14]. This is primarily due to the alternate energy sources not being able to cope with the increasing energy demands of the world. It has also been predicted that the consumption of fossil fuels is not going to significantly drop in the coming decades [13, 14]. Hence, it is essential to find ways to improve the current combustion systems to reduce the emissions. To accelerate this process, increasingly stricter regulations on emissions have been placed in the transportation sector. Improving our understanding on soot and soot formation is essential to find solutions to reduce the emissions. In the short term, this helps us to comply with these strict emission regulations, and in the long term, it is critical to keep our planet habitable for the coming generations.

Developing accurate diagnostic tools is an important step in improving our understanding of soot formation. As it is a complex process, a short introduction on soot formation is given in Chapter 2. Soot formation and the properties of soot formed are sensitive to its state of evolution in the flame, the fuel, and ambient conditions. The newly formed incipient soot particles evolve further in the flame changing their size, morphology, and optical properties, by a process called soot maturation. For the prediction of climate and health effects, these are all important attributes. Salts of metals such as potassium (K) and sodium (Na), which are commonly present in biomass, also influence the formation of PAH and soot (Paper III). As another example, the diesel additive tripropylene glycol monomethyl ether (TPGME) has also been found to influence soot formation and oxidation (Paper IV, V). Furthermore, ambient pressure has been found to influence the soot maturation process (Paper II). This thesis involves with the development and use of laser-based

diagnostic techniques for investigating the formation, and properties of soot in various combustion systems.

Soot formation was studied in different combustion systems ranging from small scale laboratory burners to an optical diesel engine. These combustion systems have been discussed in Chapter 2. Multiple laser-based diagnostic techniques were employed to study different aspects of soot formation. Laser-induced incandescence (LII), extinction, laser-induced fluorescence of PAHs (PAH-LIF) and elastic light scattering (ELS) were some of the techniques used. In addition to these, a heat-and-mass-transfer-based LII model [15] was also used to both develop the quantitative LII measurements and to study the soot maturation process. More details on all the diagnostic techniques used and the LII model are given in Chapter 3. The main results of the investigations in Papers I-V are discussed in Chapter 4. Finally, the work is summarised in Chapter 5 along with an outlook.

2 Combustion and Soot

In this chapter, an introduction is given about the concept of combustion and its types, soot formation and a brief discussion on the various sources of soot.

2.1 Combustion Fundamentals

Combustion can be simply defined as an exothermic reaction between a fuel and an oxidizer. Common fuels involved in combustion processes are carbon-based solid, liquid, or gaseous fuels and the oxidizers are usually air or oxygen. The chemical equation of an ideal combustion process of one such fuel ethylene (C_2H_4) with air can be written as

$$C_2H_4 + 3(O_2 + 3.76\,N_2) \rightarrow 2CO_2 + 2H_2O + 11.28N_2, \qquad (2.1)$$

where the composition of air is assumed to be (21 % O_2 and 79 % N_2). *Ideal* refers to that the only net products formed are CO_2 and H_2O. It can also be called a *complete* or *stoichiometric* reaction as the only net products formed are CO_2 and H_2O without any excess of fuel or oxidizer or any other species remaining. The global reaction in Eq. 2.1 does not describe the chemistry on a detailed scale, for which chemical mechanisms involving hundreds of species and elementary reactions are needed.

Combustion processes can generally be classified into two in terms of how the reactants are transported to the reaction zone. *Premixed* and *non-premixed flames*, where the latter is often referred to as a diffusion flame. For a premixed flame, the fuel and oxidizer are mixed before the reaction zone. The flames studied in Papers I, III, in a spark-ignition engine, etc. are examples of premixed flames. In a diffusion flame, the fuel and oxidizer are kept separate and forms the reaction zone at the interface. Flames studied in Paper II, and most often the combustion process inside a Diesel engine (Papers IV and V) are examples of diffusion flames.

Premixed flames are usually characterized by the parameter called the *equivalence ratio* (ϕ). Equivalence ratio is defined as,

$$\phi = \frac{(n_f/n_o)_{actual\ mix}}{(n_f/n_o)_{stoic.\ mix}}, \tag{2.2}$$

where, n_f and n_o represent the number of moles of fuel and oxidizer, respectively. By definition, a stoichiometric reaction has an equivalence ratio, $\phi = 1$. Combustion processes or flames with $\phi > 1$ are termed as *fuel rich* flames and those with $\phi < 1$ are called as *fuel lean* flames. For diffusion flames the fuel and oxidizer are not mixed before combustion, and a global equivalence ratio cannot be defined. However, one can define local equivalence ratios at the reaction zones.

2.2 Soot and its Formation

Soot is a product of incomplete combustion of hydrocarbon-based fuels which consists primarily of carbon and to some extent also hydrogen [16]. Figure 2.1 from Michelsen et al. [7] shows a brief summary of the soot formation process.

At high temperatures, the fuel and oxidizer molecules dissociate into smaller radicals OH, O, H, CH, CH_2, etc., which lead to reactions that result in the formation of larger hydrocarbon radicals and polycyclic aromatic hydrocarbon (PAH) species. PAHs are considered as the precursors of soot [7, 17]. These PAHs nucleate, react, and combine, or grow to form incipient soot particles. One likely pathway of this growth process of PAHs is the hydrogen-abstraction-carbon-addition (HACA) mechanism [18, 19]. These liquid-like incipient soot particles have carbon-to-hydrogen (C/H) ratios in the range of 1.4 – 2.5 and generally have a disordered fine structure. These particles grow further in size by coalescence (merging or coagulating) and surface growth to form larger primary particles with diameters ranging from 10 – 50 nm. Further on, these primary particles aggregate together to form chain-like structures, which can be several hundred nanometers in size with hundreds of almost spherical primary particles. During this growth process, the C/H ratios increase to the range between 10 – 20, soot fine structure becomes more ordered, the optical band gap and interlayer spacing decreases, and the electrical conductivity increases [7]. This process is called *soot maturation* where the less mature incipient particles transform into more graphitic or more *mature* soot particle.

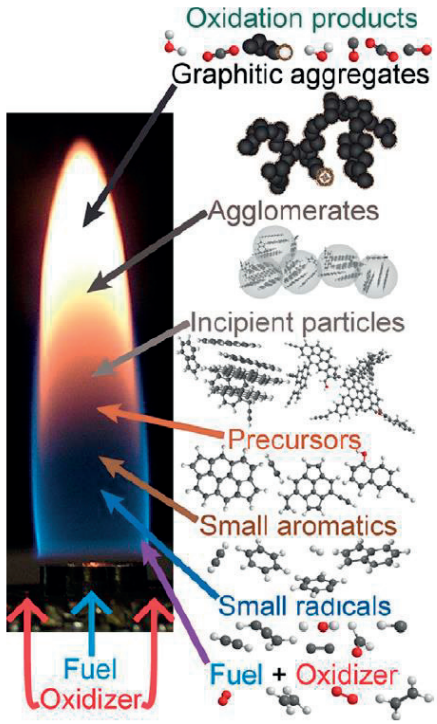

Figure 2.1: Schematic representation of soot formation and evolution in a flame [7].

2.2.1 Soot Properties

Knowledge on the various properties of soot particles is important to understand and predict the impact of soot on both the climate and human health. Soot particles can be characterized using several parameters. Some of the important ones are discussed here.

During the evolution of soot, small soot particles coagulate and aggregate to form large soot aggregates. Individual particles in this aggregate are called primary particles. Primary particles are approximately spherical in shape and are generally characterized by their diameters (d_p). Usually, the sizes of primary particles in an aggregate follow a distribution, which sometimes is assumed to have lognormal or normal distributions [17]. Another geometric parameter related to soot aggregates is the aggregate size, N_p, which is defined as the number of primary particles per aggregate. Over a region across the flame, aggregate size also follows a distribution.

Soot density (ρ_s) and specific heat capacity (c_s) are two of the important physical properties of soot. The parameters ρ_s and c_s are dependent on temperature and maturity and hence, usually temperature-dependent expressions are used for these parameters, for example in the modelling of time-resolved LII signals as described in Chapter 3. However, their product, the volumetric heat capacity, $\rho_s c_s$, was found to be fairly constant at temperatures close to flame temperatures ($\gtrsim$ 1500 K) [20]. The volumetric heat capacity was found to be independent to soot maturity as well [20].

When describing the interaction between light and soot particles, such as absorption, emission and scattering of laser light, the optical properties of soot are essential. The thermal radiation from the soot particles also depends on the optical properties of soot.

In the simplest model of a soot particle with respect to its optical properties, soot particles are assumed to be homogenous spheres with a complex refractive index m.

$$m = n + \mathrm{i}k, \tag{2.3}$$

where, n is the refractive index of the particle related to the phase velocity in the medium ($n = \mathrm{c}/v_{phase}$, where c is the speed of light in vacuum and v_{phase} is the phase velocity in the medium or particle), and k is a related to the particle's absorption. The complex refractive index of soot has been found to vary with chemical composition and temperature of soot, and the wavelength of the light [17, 21]. It is also important in measurements involving absorption or scattering of light by the particle via the refractive index functions,

$$E(m) = -\mathrm{Im}\left\{\frac{m^2-1}{m^2+2}\right\} \text{ and, } F(m) = \left|\frac{m^2-1}{m^2+2}\right|^2. \tag{2.4}$$

$E(m)$, known as the absorption function, appears in expressions involving absorption and emission, whereas $F(m)$, is present in the expression for scattering [17]. The value of $E(m)$ of a soot particle has been shown to increase with increase in soot maturity. Although, the value of $E(m)$ for mature soot has been deduced to be between 0.29 and 0.52 in the literature [22]. In some recent studies a value of 0.35 has been reported for the most mature soot [23, 24]. The values of $E(m)$ were estimated in methane-air diffusion flames at elevated pressures in the work presented in Paper II.

2.2.2 Combustion and Soot Formation in Diesel Engines

A typical conventional diesel engine has four stages in its combustion process as shown in Fig. 2.2 [25]. The first stage called the ignition delay period is the time gap between the start of injection (SOI) and the start of combustion. Here, fuel is injected at high pressure into the cylinder with compressed and thereby heated air. Due to the intense momentum exchange between the liquid fuel and the ambient air, the liquid fuel jet breaks down into small droplets which then later atomize and subsequently vaporize. This fuel vapour mixes with air to reach a flammable equivalence ratio, and when the temperature inside the combustion chamber is sufficiently high, auto-ignition occurs. The second stage of premixed combustion starts afterwards where the initial ignition locations rapidly cause the ignition of the rest of the mixture. Afterwards, the mixing-controlled combustion phase occurs when most of the mixture formed during the ignition delay gets consumed, while the fuel injection still goes on. Here, the heat release rate is primarily controlled by the fuel-air mixing. Generally, the peak heat release rate in this phase drops after the end of injection (EOI). After the EOI, the heat release is continued at a lower rate into the expansion stroke where most of the combustion products undergo oxidation, although at a much lower rate due to reduced mixing rate and temperature.

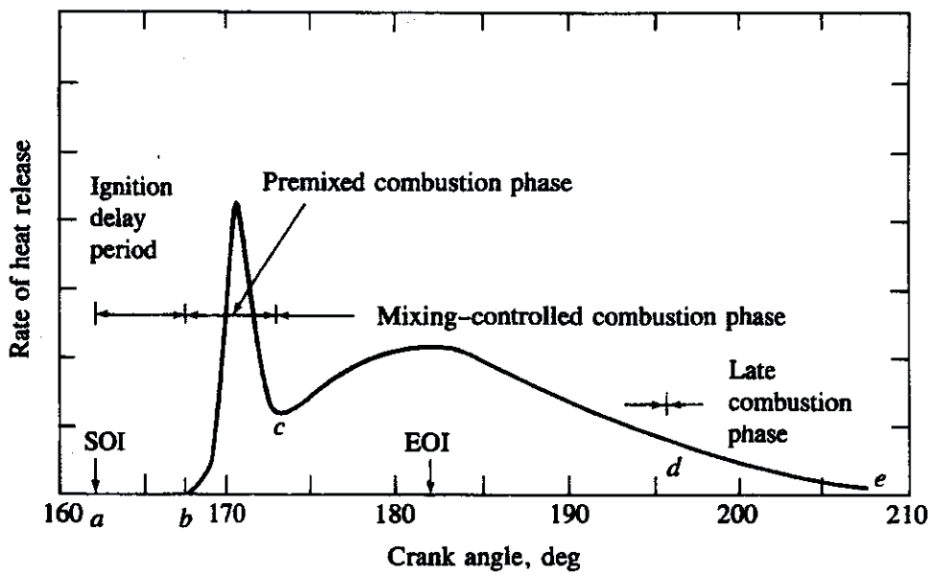

Figure 2.2: Heat release rate from a conventional diesel engine combustion process [25].

With the help of various optical diagnostic techniques applied in an optically accessible engine, Dec et al. has devised a detailed in-cylinder process model from the SOI to a quasi-steady reacting diesel jet [26], shown in Fig. 2.3.

The liquid fuel jet starts to break up immediately after leaving the injector nozzle and the ambient air is entrained. This hot ambient air vaporizes the liquid fuel droplets to form a rich mixture layer surrounding the liquid jet. As the fuel injection and air entrainment continue, the liquid fuel jet reaches its maximum penetration when the injection and vaporization rates balance out. A rich gaseous mixture zone surrounded by a thin layer of premixed combustion is formed when the fully evaporated mixture is driven further downstream. Near this premixed combustion region, the initial soot formation process starts. The intermediate combustion products including most of the incipient soot is driven outwards from the centre of the jet by the jet flow and diffusion. Here, it mixes with the ambient air to oxidise and form a high temperature diffusion flame layer in near stoichiometric conditions. The unoxidized initial soot particles, propagate to the tip of the jet along with other intermediate species to form a vortex region. During this transport, soot particle growth and aggregation occur, leading to high soot concentrations in this tip region [26].

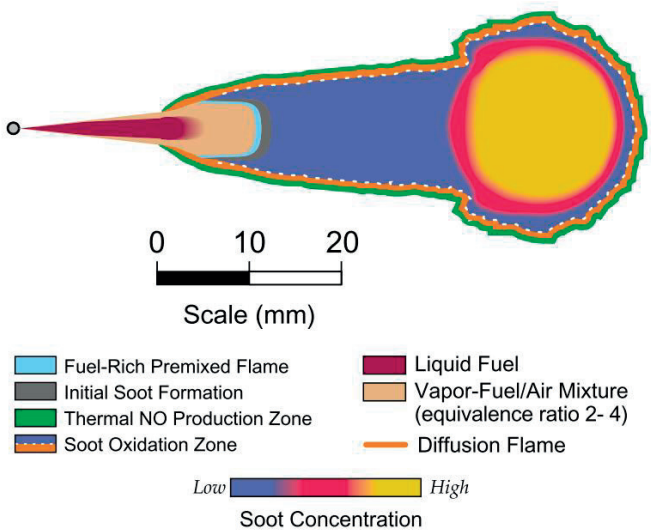

Figure 2.3: A conceptual model of quasi-steady reacting diesel jet by Dec et al. [26].

2.3 Experimental Soot Sources

Soot formation has been investigated in both small-scale laboratory burners and a diesel engine, which is a practical combustion device. Basic descriptions of all the combustion systems studied in Papers I-V are given here.

2.3.1 Laboratory Burners

The McKenna Burner

The McKenna burner, manufactured by Holthius & Associates, is a gas burner used to produce flat premixed flames. A photograph along with a schematic of the McKenna burner is shown in Fig. 2.4. From the schematic, it can be seen that the burner has a central porous plug region (diameter = 60 mm) through which, the fuel/oxidizer mixture exits. Just outside the central porous plug, there is a co-annular porous plug through which a shielding co-flow exits. This co-flow is used to shield or protect the flame from the disturbances caused due to the movement of air in the room. The gas for the fuel/oxidizer mixture and the co-flow are supplied through pipes connected at the bottom of the burner. It can also be seen from Fig. 2.4b that the burner is water cooled. Additionally, a stainless-steel flame stabilizer with a diameter of 60 mm is placed 21 mm over the burner surface to achieve a stable flame suitable for measurements.

The laminar premixed ethylene-air flame (ϕ = 2.1) stabilized on a bronze plug McKenna burner was used for the work in Paper I and is one of the target flames in the LII community [27]. The total flow rate of the ethylene-air mixture through the central porous plug is kept at 10 l/min (at 273 K and 1 atm). The stabilization plate should also be placed so that the lower surface is 21 mm over the burner surface. Although details about the co-flow have not been specified in the target flames, a co-flow of air with a flow rate of 9 l/min (at 273 K and 1 atm) was used in the work presented in Paper I. In such a flame, the incipient soot particles start to form at an HAB of 4 mm, which grow with increasing HAB.

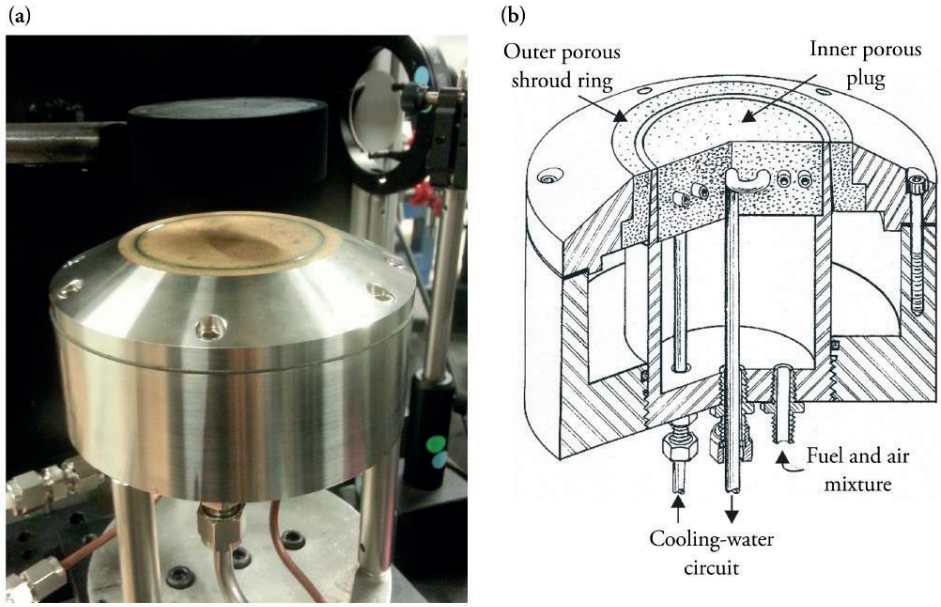

Figure 2.4: **(a)** The McKenna burner along with the stainless-steel stabilizer plug placed so that its lower surface is 21 mm above the burner surface. **(b)** Schematic representation of the burner [28].

Figure 2.5 shows the flame luminosity image of the target flame studied in Paper I. The McKenna burner is considered to produce one-dimensional flames (also known as *flat* flames), where the properties only vary with height above burner (HAB) and remain fairly constant in the horizontal plane. However, some studies have shown that flames produced in the McKenna burner are not perfectly one-dimensional, and the main deviations are caused due to edge effects [29, 30]. However, the variation was found to be larger for flames where nitrogen was used as the co-flow, while it showed a more even soot distribution when air was used as the co-flow [30]. In the investigations presented in Paper I, air was used as the co-flow, and based on Fig. 5 in the paper, the flames can be considered to be fairly one-dimensional. Additionally, this flame was found to be low-sooting (maximum f_v < 60 ppb [31]). Hence, this particular flame was used for the work presented in Paper I. In this flame, the incipient soot particles start to form at an HAB of ~ 4 mm, which grow with increasing HAB. In such a flame, one can also study soot formation by investigating various properties at different heights using multiple laser diagnostic techniques.

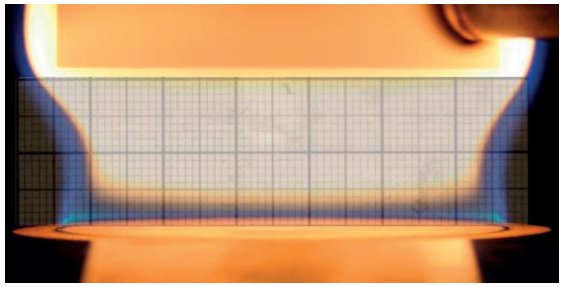

Figure 2.5: Flame luminosity image of premixed ethylene-air flame (ϕ = 2.1) stabilized on the McKenna burner. The smallest separation between the lines in the superimposed grid is 1 mm.

The Modified Perkin-Elmer Burner

The modified Perkin-Elmer burner produce similar and fairly one-dimensional flames like the McKenna burner. However, the flames are physically smaller than those produced by the McKenna burner. Figure 2.6 shows the images of the burner setup. The modified Perkin-Elmer burner has the capability to seed solutions into the flame directly through the fuel-air mixture. The air from one of the air inlets aspirates the solution from an external container through a thin pipe (inner diameter < 1 mm). The solution then hits on an impact bed to form an aerosol with small water droplets. These small droplets are transported up towards the burner head along with the fuel-air mixture while large droplets are removed using a drain and collected in a container. It is important to keep the drain tube immersed in a liquid to avoid the leakage of gases through the drain. The air, fuel and co-flow gases exit the burner through a mesh with a diameter of 45 mm, where the mesh has a depth of 20 mm and a hole diameter of 1 mm. The fuel-air mixture along with the seeded liquid droplets exit through the central region of the mesh with a diameter of 23 mm.

For the investigations presented in Paper III, a premixed ethylene-air flame (ϕ = 2.6) was used. Ethylene and premixing air were set to flow rates of 0.27 l/min and 1.5 l/min (273 K, 1 atm), respectively. A significantly large flow of 9 l/min (273 K, 1 atm) was used for the co-flow air as the flame was sensitive to disturbances in the ambient air flows. Additionally, a stainless-steel stabilizer plug of diameter 20 mm was placed so that the lower surface is 21 mm above the burner surface. Solutions with 1 M, 0.1 M and 0.01 M of KCl, NaCl, KOH and NaOH, and 0.5 M, 0.05 M and 0.005 M solutions of K_2CO_3 were aspirated into the flames in this work. The flow rates of the salt solutions were approximately 3 ml/hour, which corresponds to a salt concentration of ~ 700 ppm for the 1 M case. This work was performed to investigate the influence of various metal salts on PAH and soot formation. The

commonly used McKenna burner was not used for this study as it was not possible to seed the flames with salts/salt solutions without the salt particles getting stuck in the porous plug.

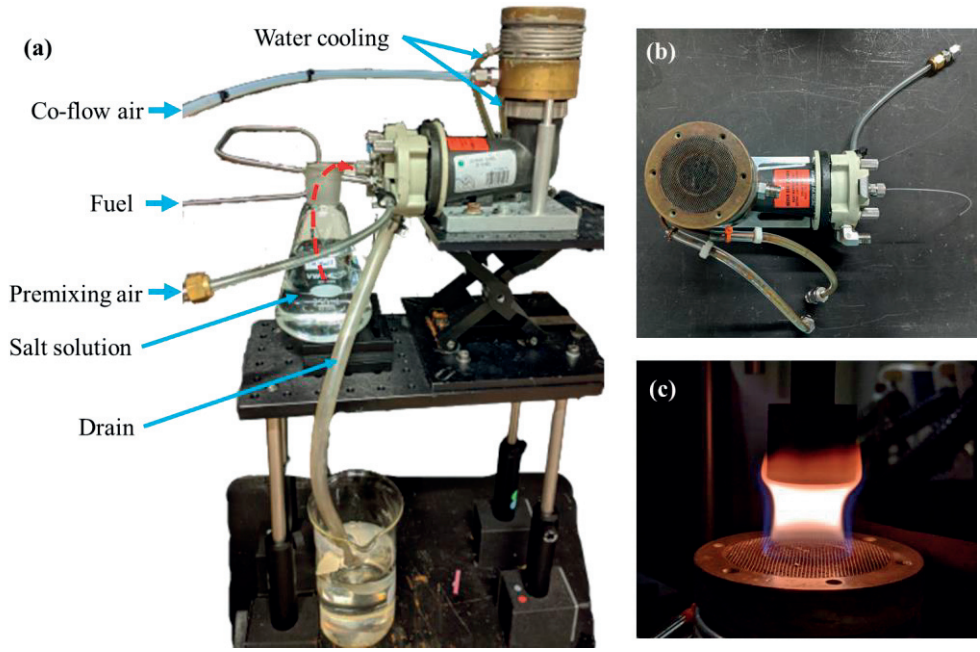

Figure 2.6: **(a)** Image of the modified Perkin-Elmer burner with the connectors to the burner marked. **(b)** Top view of the burner showing the mesh for fuel-air mixture. **(c)** Image with the flame and the stabilizer plug.

High-Pressure Burner

Figure 2.7 shows a photograph and a schematic representation [32] of the high-pressure burner used in the investigation presented in Paper II. The burner is cylindrical in shape, and can operate up to a pressure of 36 bar and a maximum ambient temperature of 220 °C. The cylindrical combustion chamber has an inner height of 500 mm and an inner diameter of 254.5 mm. There are optically accessible windows placed equidistantly along the circumference. The pressure inside the chamber is kept constant by regulating the exiting gas flow rate electronically with the use of back-pressure regulators.

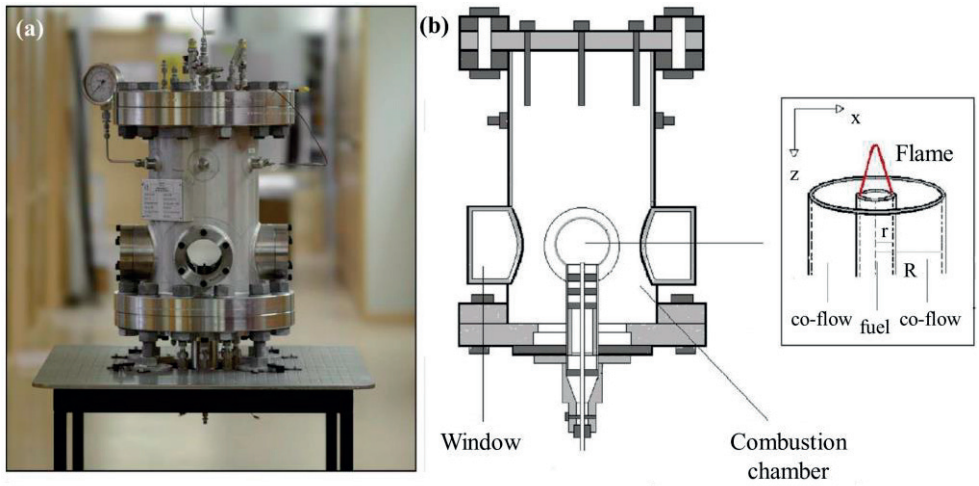

Figure 2.7: **(a)** Photograph of the high-pressure burner. **(b)** Schematic representation of the burner [32].

Methane-air co-flow diffusion flames at 0.1 to 0.5 MPa were investigated in the study presented in Paper II. A central tube with an inner diameter of 5 mm carried methane, while a co-axial tube with an inner diameter of 35 mm carried air into the combustion chamber. Methane and air mass flow rates were set to 1.1 mg/s and 0.2 g/s respectively. The flames were continuously monitored using a digital camera (Nikkor, D7100) equipped with an f = 200 mm AF Micro Nikkor camera lens. Figure 2.8 shows the flame luminosity images captured using this camera at pressures ranging from 0.1 to 0.5 MPa. The visible flame height remains fairly constant with increase in pressure, although a small decrease can be observed for the 0.5 MPa case. Increase in pressure also resulted in a drastic increase in soot concentrations. More details about the burner can be found here [32-34].

Figure 2.8: Flame luminosity images of methane-air co-flow diffusion flames at 0.1 MPa to 0.5 MPa.

2.3.2 Practical Combustion Devices

Optical Diesel Engine

A multi-cylinder light-duty Volvo diesel engine was operated as a single-cylinder optical engine using a Bowditch design for the investigations presented in Papers IV and V. A schematic representation of an optical engine is given in Fig. 2.9. Four quartz windows in the cylinder liner provide optical access from the sides of the top volume of the cylinder. The transparent quartz piston mounted on a piston extension provides optical access from below. The optical piston has the same geometry as the one in a production engine. The combustion chamber can also be visualized through the quartz piston by using a 45° mirror as shown in Fig. 2.9.

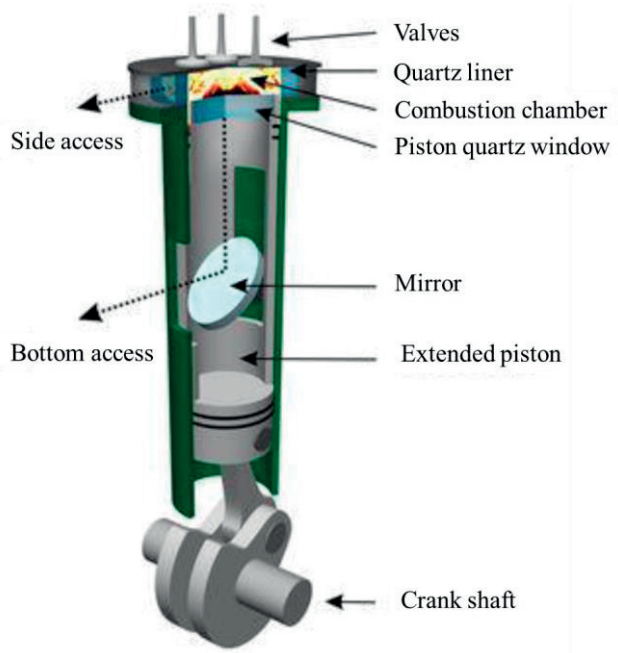

Figure 2.9: Schematic representation of an optical engine [35].

Combustion and soot formation in a diesel engine were introduced in section 2.2.2. One of the main topics discussed in Papers IV and V is the effects of aging of injectors on the formation of spray, and the formation and late cycle oxidation of soot. To study this, two sets of differently aged injectors were selected. The first set contains new injectors, which only have been used for a couple of hours of test run. The second set, being the aged ones, have been used over 100,000 km of field test.

Both the sets of injectors are Denso's 4th generation solenoid injectors used in light-duty diesel engines. They have 8 tapered nozzle holes with outlet diameters of 125 µm and umbrella angles of 155°. For the investigation of spray formation, a non-reactive environment is created using exhaust gas recirculation (EGR). This is achieved by using a diesel burner as an external EGR source. The oxygen level inside the combustion chamber can be as low as 5 % to prevent the occurrence of combustion.

The second topic of investigation is related to the influence of the soot reducing additive tripropylene glycol monomethyl ether (TPGME) on soot formation and late-cycle oxidation. For studying this, two sets of fuel blends were used in the optical engine. The first one termed as baseline diesel meets the CEC RF-79-07 standard. The second fuel is a blend of the baseline diesel and a 5 % vol. TPGME. The fuel blend with TPGME is calculated to have around 1.5 % oxygen concentration by weight assuming there is no oxygen content in the baseline fuel. Other important properties of the tested fuels are given in Table 2.1.

Table 2.1: Properties of the baseline fuel (BL) and the blend with TPGME additive [36].

	Baseline (BL)	TPGME
Composition	CEC RF-79-07 Pure diesel	Baseline fuel + 5 % vol. TPGME
Density @ 15 °C (kg/m^3)	833.8	837.6
Net heating value (MJ/kg)	43.2	42.76
Flash point (°C)	84	84

The engine was operated without exhaust gas recirculation (EGR) and at a speed of 1200 rpm, which accommodates the repetition rate of the laser system (10 Hz, Paper V). Additionally, a 1:9 skip fire sequence was incorporated for the measurements. The operating points of the optical engine were devised by adapting the two reference points provided by Volvo for metal engines. Both the reference points involve two pilot injections, followed by one main injection and one post injection. These two reference points are termed as the low load and mid load conditions. More details on these operating conditions are given in Table 2.2 and in Papers IV and V.

Table 2.2: Operating conditions of the optical engine for both loads used in this study. (IMEPg – Gross indicated mean effective pressure. TDC – Top dead centre.)

	Low load	Mid load
Injection pressure [bar]	450	850
Intake pressure [bar]	1.27	1.83
Intake temperature [°C]	75	75
Engine speed [rpm]	1200	1200
Engine load $IMEP_g$ [bar]	~ 4	~ 9
EGR [%]	0	0
Estimated TDC density [kg/m^3]	~ 15	~ 22
Estimated TDC temperature [K]	~ 880	~ 890

3 Diagnostic Techniques & Numerical Models

Sooting flames have been studied using both probing and optical diagnostic techniques. Probing techniques use a probe either to measure a property at the location of insertion or to collect samples for further analysis using a specific instrument. Temperature measurements using thermocouples and sampling of soot from flames and further analysis using instruments, such as *transmission electron microscope* (TEM), *scanning mobility particle sizer* (SMPS), *single particle soot photometer* (SP2) are examples of probing techniques [7, 17]. These techniques are intrusive in nature as they tend to disturb the processes they are investigating. Additionally, they are often limited by low spatial and temporal resolutions.

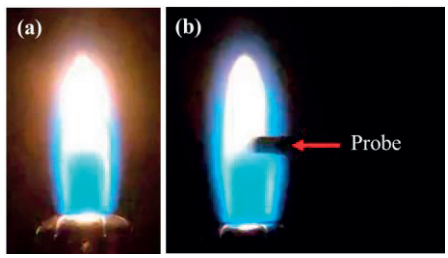

Figure 3.1: Effects of intrusive probe measurements. The stable flame **(a)** gets disturbed upon the insertion of the probe **(b)**.

Optical diagnostic techniques, such as laser-based diagnostic techniques, can be considered as a non-intrusive alternative to probing techniques [7]. Optical diagnostic techniques generally involve the use of electromagnetic radiation either emitted, scattered or absorbed by the system under study. The emitted radiation could be in the form of natural luminosity emission, chemiluminescence, fluorescence, incandescence, etc. which, for instance, could give information on temperature, species concentration, or several other properties in the flame [7]. Absorption measurements have also been used for obtaining species [37-40] and

soot concentrations [31]. Contrary to probing diagnostics, optical diagnostics can provide high temporal resolution, and often also high spatial resolution.

There are several diagnostic techniques which can be used for studying soot formation. However, this chapter only revolves around the various diagnostic techniques and mathematical models relevant to the works reported in this thesis. A brief description of the technique along with its applications and generic experimental setups are discussed. In addition to these, this chapter also include discussions on the various limitations and uncertainties of these techniques. A discussion on the heat and mass transfer model for laser-induced incandescence (LII), which was used in the work presented in Papers I and II, has also been included.

3.1 Laser Extinction

3.1.1 Theory

Laser extinction or *extinction* is a technique where a laser beam is sent through a medium and the laser energy absorbed by the medium is measured [31]. The decrease in light intensity through the absorbing medium can be related to the extinction coefficient K_{ext}, using the Beer-Lambert law as

$$I_t = I_0 e^{-K_{ext} L}, \tag{3.1}$$

where I_0 and I_t are respectively the incident and transmitted light intensities, and L, the length of the absorbing medium. In addition to absorption, scattering could also contribute to the total extinction. The total extinction coefficient is given as, $K_{ext} = K_{abs} + K_{sca}$, where K_{abs} and K_{sca} are respectively the absorption and scattering coefficients.

Extinction measurements performed under appropriate conditions, while involving certain assumptions, can be used for obtaining soot volume fractions. Soot volume fraction (f_v) is defined as the fraction of volume occupied by soot particles in unit volume. Assuming spherical and monodisperse particles, f_v can be written as,

$$f_v = N \frac{\pi {d_p}^3}{6}, \tag{3.2}$$

where N is the number density and d_p is the primary particle size (expressed as the diameter) of soot in the medium. Primary particle diameters of soot particles found in flames are usually in the range of 5 – 30 nm, and are often investigated using light with wavelengths in the visible and infrared regimes. If the soot particles have sizes much smaller that the wavelength used for the extinction measurements, the Rayleigh criterion is fulfilled [41]. For the measurements performed in the Rayleigh regime the scattering contribution to the extinction is commonly assumed to be negligible [41]. Hence, under such circumstances, K_{ext} is equal to K_{abs}. According to Rayleigh theory for isotropic spheres, the absorption coefficient of individual particles is given by,

$$K_{abs} = -\frac{\pi^2}{\lambda}\mathrm{Im}\left\{\frac{m^2-1}{m^2+2}\right\}N{d_p}^3, \tag{3.3}$$

where λ and m are respectively the laser wavelength and the complex refractive index of soot. The factor $-\mathrm{Im}\left\{{(m^2-1)}/{(m^2+2)}\right\}$, which represents the imaginary part of the expression inside the curly brackets, is often denoted as the absorption function $E(m)$, which is discussed in section 2.2.

Combining Eq. 3.1 – 3.3 while using the assumption $K_{ext} = K_{abs}$ and the expression for $E(m)$, the soot volume fraction can be expressed as,

$$f_v = \frac{K_{ext}\lambda}{6\pi E(m)} = \frac{\lambda}{6\pi E(m)}\ln\left(\frac{I_0}{I_t}\right)\frac{1}{L}\,. \tag{3.4}$$

3.1.2 Experimental Setup

A typical experimental setup used for extinction measurements is shown in Fig. 3.2. A continuous wave (CW) diode laser operated at a certain wavelength (850 nm in Paper II, and 690 nm in Paper V), which is long enough to avoid absorption from PAHs is ideal for extinction measurements. It has been shown in the literature that PAHs do not fluoresce when excited using wavelengths $\gtrsim$ 680 nm [8]. Another study has also shown that PAHs have negligible influence to extinction for wavelengths $\gtrsim$ 700 nm [31].

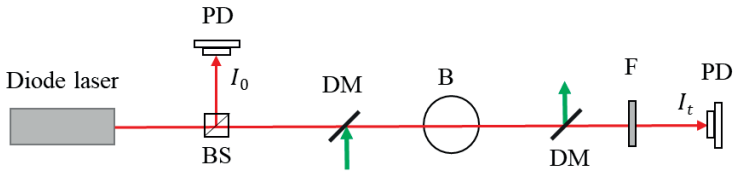

Figure 3.2: Schematic of the experimental setup for extinction. Abbreviations: BS – Beam splitter, PD – Photodiode, DM – Dichroic mirror, B – Burner, F – Optical filter(s). The green arrows represent the spatially overlapped laser sheet used for other 2D diagnostics like LII.

The laser beam from the CW laser was split into two components using a beam splitter cube (BS), where one of the components was used as the reference (I_0) and the other (I_t) was sent through the flame. The beams I_0 and I_t finally terminate at photodiodes (PD), which measure their energies. The relation between I_0 and I_t with and without the flame is used to estimate the net extinction and subsequently the soot volume fraction using Eq. 3.4. Simultaneous measurement of I_0 with I_t improves the accuracy of the results as they can overcome the problems due to fluctuation in laser energy over time. A band-pass filter (F) corresponding to the respective laser wavelength is used to minimise background radiation. Additionally, ON-OFF modulations were introduced into the laser beam (500 Hz and 72 kHz in the works presented in Papers II and V, respectively). This has been discussed in detail in Paper V. These modulations allow the possibility to acquire background signals in between the measurement points for efficient background subtraction. The procedure of background subtraction and the calculation of soot volume fractions have been discussed in detail in Paper V. Fast modulations of 72 kHz were achieved by using an acousto-optic modulator and was used for optical engine measurements to obtain crank-angle resolved data, see details in Paper V.

Extinction, when used in combination with 2D LII measurements can provide absolute 2D f_v distributions, which is discussed in section 3.2. For this, the extinction laser beam and the laser sheet used for 2D LII measurements are spatially overlapped at the desired height using a dichroic mirror (DM). Both the laser beam and sheet are separated after the flame region using another dichroic mirror. More details about the extinction setup can be found in [28] and in Papers II and V.

3.1.3 Uncertainties

The main uncertainty involved with extinction measurements and evaluating soot volume fractions is the absorption function, $E(m)$, which can be interpreted as the

absorption efficiency of the soot. The value of $E(m)$ increases with increase in soot maturity [17]. It is tricky to evaluate the value of $E(m)$ accurately, and as discussed in Paper II, soot maturity can vary spatially in the same flame or across flames. In addition to this variation, the values reported of $E(m)$ in the literature for mature soot alone has a large spread between 0.29 to 0.52 [22]. It can also change with wavelength as the refractive index m is wavelength dependent [31, 42]. The magnitude of error in the measurements would depend on the value chosen for $E(m)$ compared to the actual optical properties of the particles under investigation.

Another source of uncertainty lies in the estimation of absorption length. Although the absorption length does not influence the total amount of soot calculated along the beam path, it is critical in the estimation of soot volume fraction (Eq. 3.4). While it is possible to measure it with fairly good accuracy in small-scale laboratory systems, measurements in large scale and transient systems would pose challenges. In small scale systems such as the McKenna or Perkin-Elmer burners, the absorption length can be estimated either from the natural luminosity images or from the LII signal images by using a threshold in the signal intensity level. However, for the optical engine measurements (Paper V), the error in estimating absorption lengths could be much larger due to a variety of reasons. For example, as the flames in these systems were turbulent, it would be difficult to know if soot was present in the entire beam path. In these studies, the absorption length was evaluated using the mean LII signal image which would have uncertainties related to the turbulent nature of the flame.

Presence of other absorbing species in the region of interest is yet another source of uncertainty. In sooting flames, the presence of polycyclic aromatic hydrocarbons (PAHs) could potentially cause this uncertainty unless care is taken to avoid this. PAHs are found to strongly absorb in the UV and visible regimes up to ~ 680 nm [8] and not to absorb beyond 700 nm [31]. Use of a laser with wavelength above 680 nm could mitigate this issue of unwanted absorption by PAHs. Extinction measurements in all the works discussed in this thesis were performed using lasers with wavelengths above 680 nm.

The assumption of negligible scattering contribution to extinction was discussed in section 3.1.1. The scattering contribution in small-scale flames are generally small to not inflict large uncertainties in extinction measurements. However, for larger soot particles the scattering-to-absorption ratio, ρ_{sa} has been estimated to be between 0.2 to 0.4 depending on the fuel and wavelength [23, 43]. This could result in an uncertainty of 20 – 40 % in the corresponding estimations of soot volume

fractions. Flames similar to those investigated by Simonsson et al. [44] were studied by Bäckström et al. [45, 46]. Single-scattering albedos (SSA) which is the ratio of scattering and total extinction were estimated and it showed a reduction in SSA with increasing wavelengths. For 781 nm a value of 0.03 was obtained for SSA, which indicates a low influence of scattering in the measurements.

3.2 Laser-induced Incandescence (LII)

Laser-induced incandescence (LII) is a diagnostic technique that can be applied to particles, where the most common application is to measure on soot [17]. Initially, the soot particles are heated up to high temperatures (~ 3500 – 4000 K) using laser pulses. The resulting enhanced Planck radiation from the heated soot particles, called the LII signal is acquired using a detector. The LII signal is found to be proportional to soot volume fraction to a first approximation [17, 47].

In addition to soot volume fraction measurements, LII can be used for obtaining parameters such as the primary particle size [47, 48], soot optical properties [24, 34, 49]. The procedure for primary particle size evaluation will not be discussed in this context as it has not been used in the studies mentioned in this thesis. However, applications of LII in evaluating soot optical properties are discussed in section 3.2.2 and in Paper II.

3.2.1 Energy and Mass Balance of Heated Soot

LII process can be theoretically described in terms of several physical processes related to heat and mass transfer phenomena [17]. Some of these processes are absorption, radiation, conduction, sublimation, oxidation, annealing, and thermionic emission. Among these physical processes, absorption, heat conduction, radiation and sublimation are the most predominant ones. The energy-balance equation including these heat and mass transfer processes can be written as

$$\frac{\mathrm{d}U_{int}}{\mathrm{d}t} = \frac{\mathrm{d}Q_{abs}}{\mathrm{d}t} + \frac{\mathrm{d}Q_{rad}}{\mathrm{d}t} + \frac{\mathrm{d}Q_{cond}}{\mathrm{d}t} + \frac{\mathrm{d}Q_{sub}}{\mathrm{d}t}, \tag{3.5}$$

where $\frac{\mathrm{d}U_{int}}{\mathrm{d}t}$, $\frac{\mathrm{d}Q_{abs}}{\mathrm{d}t}$, $\frac{\mathrm{d}Q_{rad}}{\mathrm{d}t}$, $\frac{\mathrm{d}Q_{cond}}{\mathrm{d}t}$ and $\frac{\mathrm{d}Q_{sub}}{\mathrm{d}t}$ respectively represent the rate of change of internal energy and heat transfer rates due to absorption, radiation, conduction, and sublimation of the soot particle. While absorption increases the internal energy

of the particle, the other processes are heat loss processes. Additionally, the sublimation term also involves mass loss.

Absorption

The rate of absorption can be easily evaluated if the absorption cross section is known. Absorption cross section is the geometric cross section of a particle multiplied by the so-called absorption efficiency, which represents the ratio between the true and the geometric cross section. For a primary particle, with diameter d_p, in the Rayleigh regime ($d_p \ll \lambda$, the laser wavelength), the absorption cross section is given by,

$$\sigma_{abs} = \frac{\pi^2 {d_p}^3 E(m)}{\lambda}. \tag{3.6}$$

Absorption cross section for small particles, scales with particle volume. For soot particles, if their sizes are in the regime where RDG theory [41] is valid, it can be stated that even if there are differences in their particle size, they will reach the same temperature if they are heated by uniform laser irradiance. The rate of absorption can be written using the absorption cross-section σ_{abs} as,

$$\frac{\mathrm{d}Q_{abs}}{\mathrm{d}t} = \sigma_{abs} \times F \times g(t), \tag{3.7}$$

where, F is the laser fluence (laser energy per unit area of cross-section) and $g(t)$ is the normalised temporal distribution of the laser energy.

Internal Energy

The rate of change of internal energy of the soot particle can be expressed as,

$$\frac{\mathrm{d}U_{int}}{\mathrm{d}t} = \frac{\pi}{6}\rho_s c_s {d_p}^3 \frac{dT}{dt} = M c_s \frac{\mathrm{d}T}{\mathrm{d}t}, \tag{3.8}$$

where, ρ_s, c_s, M and $\frac{\mathrm{d}T}{\mathrm{d}t}$ are respectively the density, specific heat capacity, mass, and the rate of change of temperature of the soot particle. The volumetric heat capacity, $\rho_s c_s$, was found to be independent of soot maturity and was found to be fairly constant at temperatures close to flame temperatures ($\gtrsim$ 1500 K) [20]. Thus, for a certain amount of absorbed energy, soot particles will be heated to the same temperature regardless of their maturity. Furthermore, when soot aggregates are considered, the expression for the rate of change of internal energy is multiplied by N_p, the aggregate size. This is under the assumption that the energy is uniformly

distributed in the aggregate. However, for large aggregates, this could create errors during the cooling down process of the aggregate when different parts of the aggregate might have different cooling rates due to shielding effects [50].

Heat Conduction

Heat conduction losses occur when the molecules in the ambient gas interact with the hot surface of the soot particle taking away some heat from it. Theoretically, heat conduction from particles have been represented by three regimes, which are characterised using the Knudsen number [51]. The Knudsen number, Kn, is defined as

$$Kn = \frac{\lambda_{MFP}}{L_s}, \tag{3.9}$$

where λ_{MFP} is the mean free path [52] of the gas molecules and L_s is a characteristic length scale of the particle, which is usually chosen as the diameter of the particle. The mean free path is defined as the average distance a molecule travels before it collides with another molecule. The three regimes characterizing the heat conduction are the free-molecular, the transition and the continuum regimes. In the free-molecular regime, for which $Kn \gtrsim 10$, the gas molecules that interact with the particle travel a long distance from the particle before starting to exchange the energy to other gas molecules. The continuum regime is characterised by $Kn \lesssim 0.1$, where the surrounding gas can be considered as a viscous fluid with respect to the particle. The transition regime is between these two regimes, i.e., $0.1 \lesssim Kn \lesssim 10$. Transition regime is the most interesting one with regards to LII applications mentioned in this study (atmospheric and high-pressure applications).

Heat conduction from a spherical particle to the surrounding gas in the transition regime was proposed by McCoy and Cha [53] to be described as,

$$\left\{\frac{\mathrm{d}Q_{cond}}{\mathrm{d}t}\right\}_{MC} = \frac{2k_g(T - T_g)\pi {d_p}^2}{d_p + G\lambda_{MFP}}, \tag{3.10}$$

where k_g and T_g are respectively the thermal conductivity and temperature of the gas. Meanwhile, T and G are respectively the soot temperature and geometry-dependent heat transfer factor. G is a function of heat-capacity ratio, $\gamma = C_p/C_v$ and is given by,

$$G = \frac{2(9\gamma - 5)}{\alpha_T(\gamma - 1)}, \tag{3.11}$$

where α_T is the *thermal accommodation coefficient*. Thermal accommodation coefficient represents the extent to which gas molecules exchange vibrational, rotational, and translational energy with a surface (here, surface of the soot particle) during surface-scattering events. Completely elastic gas-surface collisions (no energy transfer) result in a value of 0 for α_T. Meanwhile, when the gas molecules are fully in equilibrium with the surface, α_T takes a value of 1. This parameter has a significant influence in the conductive cooling rate [17].

The McCoy and Cha model has a closed form expression, and it can be helpful in understanding the approximate effects of various parameters on heat conduction. However, this model has limitations for LII measurements as it is valid only if there a small difference between the temperatures of the gas and the particle.

The heat conduction model by Fuchs [54] was extended by Filippov and Rosner [55], and for this model, there is no limitation to the assumption of a small temperature difference between the particle and the gas. In this model, the gas surrounding the spherical particle has been approximated to two layers. In the inner layer having a thickness of δ_{FM}, heat conduction takes place in the free-molecular regime. Here, the soot particle is at a temperature T and the boundary sphere is at a temperature T_δ. However, in the outer layer which stretches to infinity, heat conduction occurs in the continuum regime. Here, the temperature varies between T_δ at the boundary sphere to T_g, the ambient gas temperature. For this approximation to work, heat flux away from the free-molecular regime must be equal to the heat flux into the continuum regime. This is obtained by iterating the values for δ_{FM} and T_δ until $\left\{\frac{\mathrm{d}Q_{cond}}{\mathrm{d}t}\right\}_{FM} = \left\{\frac{\mathrm{d}Q_{cond}}{\mathrm{d}t}\right\}_{Continuum}$ at the boundary sphere. The Fuchs model does not have a closed-form expression. This model has been discussed in detail in Liu et al. [56].

Sublimation

When soot particles are laser heated up to temperatures above around 3500 K [24], they sublimate forming gas-phase carbon, mostly as C, C_2 and C_3 [57]. This occurs at laser fluences $\gtrsim$ 0.3 J/cm^2 for mature soot for the laser wavelength 1064 nm. Sublimation results in both mass and energy loss. The rate of sublimation depends on the heat of sublimation for soot, the particle surface area and the molecular flux of sublimated carbon. Although sublimation and vaporization are respectively, the transformations of solid and liquid phases to gas, for soot, these terms have been used interchangeably across various studies in the literature [17, 58-60]. In this

thesis, the term sublimation is predominantly used. The heat loss rate expression can be written as,

$$\frac{\mathrm{d}Q_{sub}}{\mathrm{d}t} = -\frac{\Delta H_v}{M_v}\frac{\mathrm{d}m_p}{\mathrm{d}t}, \tag{3.12}$$

where ΔH_v, M_v and m_p are the heat of sublimation (enthalpy of formation of the sublimed carbon clusters), molecular mass of the soot vapour and mass of the soot particle, respectively (subscript 'v' in the terms M_v, ΔH_v, etc. represent vaporization). Furthermore, the rate of mass-loss can be expressed as [61],

$$\frac{\mathrm{d}m_p}{\mathrm{d}t} = -\pi {d_p}^2 N_v \frac{M_v}{\mathrm{N_A}}, \tag{3.13}$$

where N_v and $\mathrm{N_A}$ are respectively the molecular flux of vaporized carbon and Avogadro's number ($\mathrm{N_A}$ = 6.023 x 10^{23}). N_v in Eq. 3.13 is in the transition regime, is given as

$$\frac{1}{N_v} = \frac{1}{N_C} + \frac{1}{N_{FM}}, \tag{3.14}$$

where the subscripts C and FM refers to the continuum and free molecular regimes respectively. In the FM regime,

$$\frac{1}{N_{FM}} = \beta n_v \sqrt{\frac{\mathrm{R}T}{2\pi M_v}}, \tag{3.15}$$

where β is the evaporation coefficient, for which often a value of 0.8 is chosen [61]. The molecular number density of soot vapour n_v can be written using the ideal gas equation as,

$$n_v = \frac{P_v \mathrm{N_A}}{\mathrm{R}T}, \tag{3.16}$$

where P_v, T, and R are respectively the vapour pressure and temperature of the sublimed soot vapour, and the ideal gas constant (8.314 J-mol^{-1}-K^{-1}). In the continuum regime, the soot vapour molecular flux, N_C, can be evaluated as

$$N_C = 2 n_v \frac{\Gamma}{d_p}, \tag{3.17}$$

where Γ is the diffusion coefficient of the soot vapour [53].

Radiation

Radiation is a heat loss term that in most cases is quite small in comparison with heat loss by conduction, often only of the order of a few percent [26]. This radiation is what is detected as the LII signal from the heated soot particles. The LII signal per primary particle calculated using the Planck function modified by the emissivity ε_λ as soot particles are not perfect black bodies, can be expressed as,

$$S = \Omega\pi {d_p}^2 \int_\lambda \varepsilon_\lambda \frac{2\pi hc^2}{\lambda^5 \left[\exp\left(\frac{hc}{\lambda k_B T}\right) - 1\right]} \Sigma_\lambda d\lambda, \tag{3.18}$$

where λ, h, c and k_B are respectively the emission wavelength, the Planck's constant, the speed of light and the Boltzmann constant. Ω and Σ_λ are factors to account for the solid angle detected and the wavelength-dependent efficiency of the detector. The emissivity in the Rayleigh regime is defined as,

$$\varepsilon_\lambda = \frac{4\pi d_p E(m)}{\lambda}. \tag{3.19}$$

Assuming no wavelength dependence of $E(m)$ and $\Omega = \Sigma_\lambda = 1$, the radiation heat transfer can be evaluated from Eq. 3.13 as,

$$\frac{dQ_{rad}}{dt} = -\frac{198.97\pi^3 {d_p}^3 (k_B T)^5 E(m)}{h(hc)^3}. \tag{3.20}$$

3.2.2 LII Model

This is a heat-and-mass-transfer-based numerical model developed by Henrik Bladh and Per-Erik Bengtsson [15], and further improved by Jonathan Johnsson [62]. The model, as its name suggests, has the capabilities to produce the time resolved LII signal upon the input of parameters related to the laser, signal acquisition and physical properties of soot. The LII model employs various mathematical models for the heat and mass transfer processes described in section 3.2.1. The LII model has been used in the works presented in Papers I and II for obtaining the LII fluence curves, and subsequently to evaluate the values of $E(m)$ in the work reported in Paper II. A brief description regarding the operation of the LII model and the various parameters used for model evaluation is given here. For more details, see these articles [15, 47-50, 63].

In the LII model, the temperature and the particle diameter are considered as state variables for the differential equation in Eq. 3.1 and their respective expansions. Once these variables are known as a function of time, the time resolved LII signal can also be calculated. The values of d_p and T as a function of time can be determined using Eq. 3.5 if their initial values are known.

The mass of a primary particle can be written as,

$$m_p = \frac{\pi}{6}\rho_s {d_p}^3 \tag{3.21}$$

The time derivative of this is given as,

$$\frac{\mathrm{d}m_p}{\mathrm{d}t} = \frac{\pi}{2}\rho_s {d_p}^2 \frac{\mathrm{d}d_p}{\mathrm{d}t} + \frac{\pi}{6}{d_p}^3 \frac{\mathrm{d}\rho_s}{\mathrm{d}T}\frac{\mathrm{d}T}{\mathrm{d}t}. \tag{3.22}$$

This expression can be rewritten as,

$$\frac{\mathrm{d}d_p}{\mathrm{d}t} = \frac{2}{\pi\rho_s {d_p}^2}\left(\frac{\mathrm{d}m_p}{\mathrm{d}t} - \frac{\pi}{6}{d_p}^3 \frac{\mathrm{d}\rho_s}{\mathrm{d}T}\frac{\mathrm{d}T}{\mathrm{d}t}\right). \tag{3.23}$$

Using the expression for internal energy in Eq. 3.8, the heat transfer equation given in Eq. 3.6 can be rewritten as,

$$\frac{\mathrm{d}T}{\mathrm{d}t} = \frac{6}{\pi {d_p}^3 \rho_s c_s}\left(\frac{\mathrm{d}Q_{abs}}{\mathrm{d}t} + \frac{\mathrm{d}Q_{rad}}{\mathrm{d}t} + \frac{\mathrm{d}Q_{cond}}{\mathrm{d}t} + \frac{\mathrm{d}Q_{sub}}{\mathrm{d}t}\right). \tag{3.24}$$

Equations 3.23 and 3.24 can be integrated over time using numerical methods of solving the ordinary differential equations to evaluate $d_p(t)$ and $T(t)$, starting from their initial values.

Table 3.1: LII model parameters. P-I and P-II represent Papers I and II respectively.

Parameter or model	Description	Value/model type
q_pulse	Temporal profile of laser pulse	Gaussian
t_{FWHM}	Laser pulse length (FWHM)	4 ns (P-I), 6.3 ns (P-II)
T	Flame temperature (surrounding gas temperature)	1595 K (P-I) 1580 – 1840 K (P-II)
P	Pressure	0.1 MPa (P-I) 0.1 – 0.5 MPa (P-II)
d_p	Primary particle size (diameter)	12.5 nm (P-I) 30 nm (P-II)
N_p	Aggregate size (Number of primary particles per aggregate)	1
ρ_s	Soot density	Michelsen model [57]

c_s	Soot specific heat capacity	Michelsen model [57]
α_T	Soot thermal accommodation coefficient	0.48 [24, 49]
β	Mass accommodation coefficient	0.8 [61]
$E(m)$	Soot absorption function	0.35 (P-I) 0.21 – 0.35 (P-II, estimated values)
Q_{Con}	Heat conduction model	Fuchs model [47, 54, 55]
Q_{Sub}	Sublimation model	Based on [47]

LII Signal Interpretation

The calculation of time-resolved LII signals involves multiple heat-transfer processes, which include properties of the soot as well as the ambient conditions (temperature, pressure), and the laser and detection properties. Figure 3.3 shows examples of time resolved LII signals obtained using the LII model for two primary particle sizes, along with the temporal profile of the laser pulse. Except for the differences in the primary particle diameters, the rest of the model parameters are the ones used in Paper I. A laser fluence (top-hat profile) of 0.3 J/cm^2 was used. One can observe a fast rise in the LII signal due to the absorption of laser energy to attain the peak signal intensity. The LII signal decays subsequently due to the effects of various heat loss processes. One can also notice that the LII signal decays faster for the smaller soot particle. This is primarily due to the smaller particle having a faster rate of heat conduction loss compared to the larger particle.

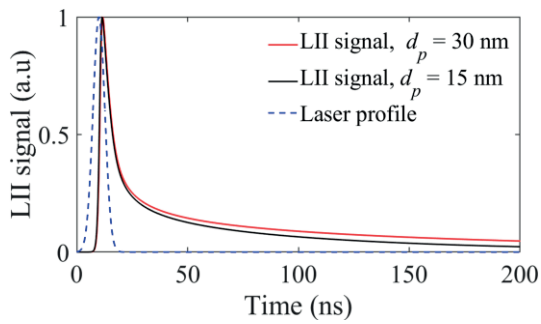

Figure 3.3: Time-resolved LII signal along with the temporal profile of the laser pulse.

The LII signal from soot in a measurement situation is highly dependent on the incident laser pulse energy, or more explicitly the laser fluence (energy per unit area), and on the spatial energy profile of the laser. Thus, it is important to investigate the response of the LII signal with respect to the laser fluence, which is called as a *fluence curve*. Fluence curve measurements are important in the selection

of a suitable laser fluence for specific LII measurements. For example, for particle sizing it is important to select a fluence avoiding sublimation, whereas for two-dimensional LII imaging of soot volume fractions a higher laser fluence can be selected to obtain spatially resolved results with lower uncertainties. Fluence curves are also sensitive to the laser spatial energy profiles. Figure 3.4 shows the three most common laser spatial intensity profiles: top-hat, Gaussian beam and Gaussian sheet profiles.

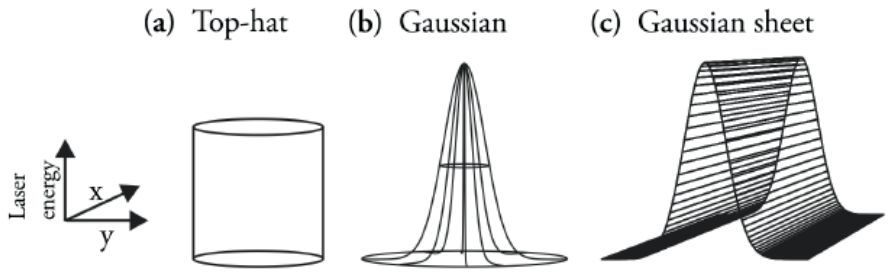

Figure 3.4: Spatial energy profiles of laser. (a) the top-hat, (b) the Gaussian beam and (c) the Gaussian sheet profiles [28].

Figure 3.5 shows the modelled LII fluence curves for top-hat, Gaussian beam and Gaussian sheet profiles normalised to their maxima. In general, the temperature of a soot particle will increase with laser fluence, and when it reaches a high enough value, the soot particle starts to sublimate. Sublimation results in mass loss of the soot particle and due to this, the LII signal decreases with further increase in laser fluence. This behaviour can be observed for the top-hat profile in Fig. 3.5, which is a case where all particles ideally are heated equally. For the Gaussian beam, the highest fluence is at the centre of the profile, and the fluence decreases towards the edges. As the mean laser fluence increases for the Gaussian beam profile, the soot in the central region (highest fluence) starts to sublime, while the soot at the edges (lower fluence) still demonstrate an increase in the LII. The overall LII signal continues to increase with an increase in laser fluence for the Gaussian beam profile. For the Gaussian sheet, which has a constant fluence along one direction and a Gaussian profile in the other direction, the decrease in the LII signal at the centre for increasing fluence gets compensated by the increase in the signal at the edges to give rise to a so-called *plateau* region. For this case, the detected LII signal in an experiment is approximately independent to the laser fluence and hence, small

variations in laser fluence do not significantly influence the resulting LII signal. Due to this behaviour, laser fluences in the plateau region are usually preferred for performing quantitative measurements of soot volume fractions in combustion systems.

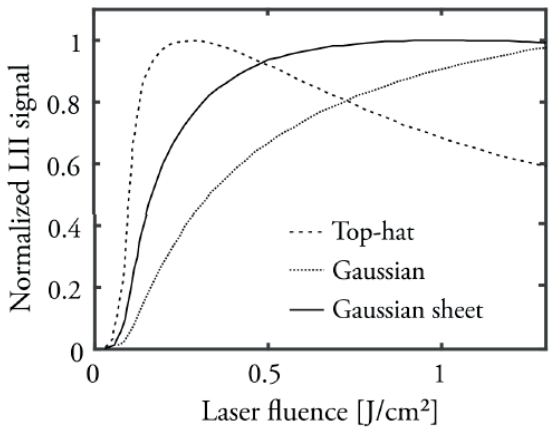

Figure 3.5: Modelled normalised LII fluence curves for top-hat, Gaussian beam and Gaussian sheet profiles [15].

Several other parameters, such as the physical and optical properties of the soot, flame conditions, and laser and detection properties, also influence the resulting LII signal and fluence curves. Figure 3.6 shows the dependence of LII fluence curves on some of these parameters numerically calculated using the LII model. All these curves are normalised to their individual maximum and use a top hat spatial profile as input in the LII model. Apart from the difference that a Gaussian spatial profile was used in the study reported in Paper I, the rest of the model parameters used for the calculations involved with Fig. 3.6 were the same as that used in the work presented in Paper I (Table 3.1). Figure 3.6a shows the fluence curves for different detection gate widths. It can be seen that the fluence curves attain the peak signal at lower fluences with increase in gate width (gw). This is due to the increasing contribution of heat-loss processes such as conduction and sublimation in the total signal with increasing gate widths. The rest of the figures 3.6b – 3.6d are based on calculations using a 30 ns detection gate width.

The influence of primary particle size on the time resolved LII signal was shown previously in Fig. 3.3. Figure 3.6b shows the influence of the same in the fluence curves. It can be seen that even a 100 % increase in primary particle size (D_p) have

minimal influence in the fluence curves. Figure 3.6c shows the influence of ambient pressure (P). It can be seen that the fluence curves shift to the right (towards high fluences) with increasing pressure. This is primarily due to the increase in conductive heat loss from the particles with increasing pressure. This is relevant for the work presented in Paper II. The influence of ambient temperature (T) on fluence curves is shown in Fig. 3.6d. It can be seen that the fluence curves shift to the left with increasing ambient temperature, as it takes lesser energy to heat up particles which are already at high temperatures. One of the most important results from Fig. 3.6 is that the largest influence among various properties of soot and ambient conditions in the simulated fluence curves is from the variation in $E(m)$, as shown in Fig. 3.6d. The sensitivity of LII fluence curves to variations in $E(m)$ have been used to evaluate values of $E(m)$ of soot in many studies in the literature [24, 64, 65] and in Paper II.

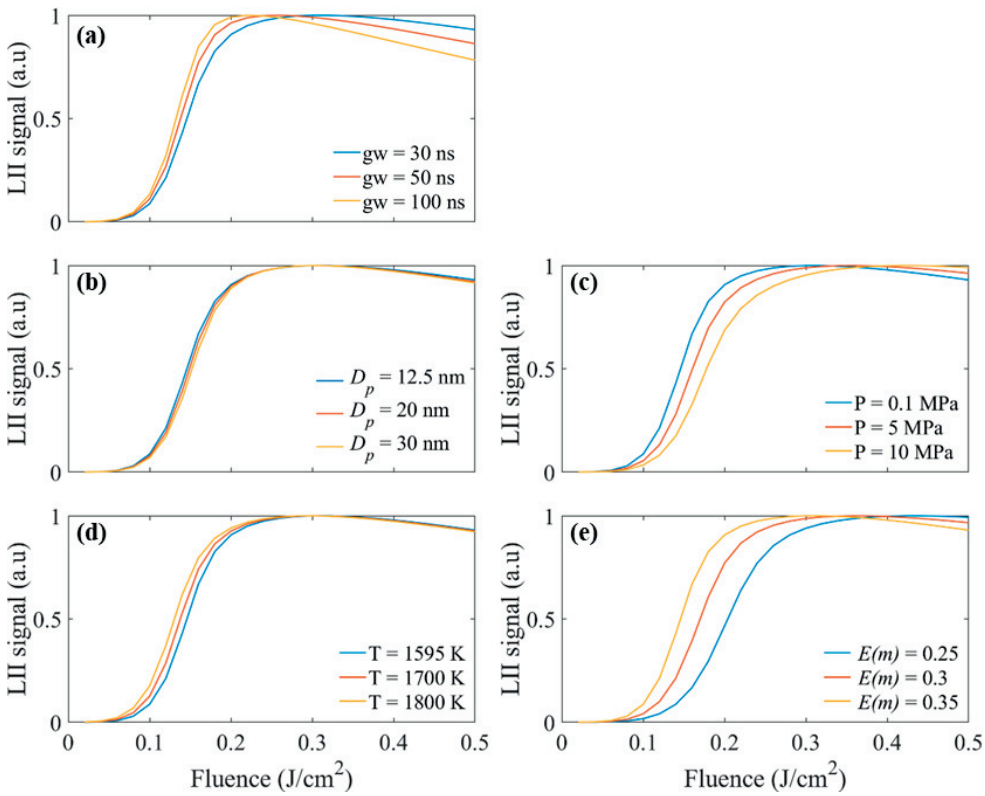

Figure 3.6: Dependence of the LII fluence curves on the model parameters such as **(a)** Detection gate width, **(b)** primary particle size, **(c)** ambient pressure, **(d)** ambient temperature and **(e)** $E(m)$ value of the soot particle.

3.2.3 Experimental Setup

A schematic representation of a representative 2D LII setup is given in Fig. 3.7. Detailed discussions on each component have been divided into different sub-sections.

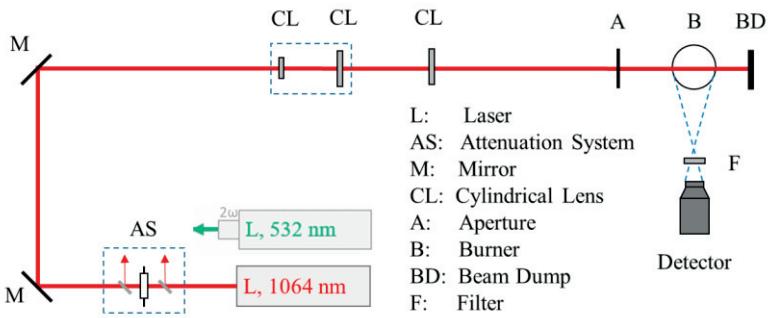

Figure 3.7: Schematic representation of an optical setup for LII.

Laser

The works in this thesis used pulsed lasers for LII measurements and hence continuous wave (CW) LII setups are not discussed here. A Nd:YAG laser (Model: Quantel Brilliant B, repetition rate 10 Hz) either operated at its fundamental mode at the wavelength 1064 nm (Papers I and V) or its frequency-doubled mode at the wavelength 532 nm (Paper II) has been used for LII measurements. In fact, lasers operated at any wavelengths in the UV, visible or near-IR with sufficiently high energy can produce soot incandescence. However, there is a drawback of using laser wavelengths below 680 nm for LII measurements. PAHs have been found to absorb radiation up to 680 nm and produce laser-induced fluorescence [8], which might interfere with the LII signal and cause uncertainties in the measurements. Hence, longer wavelengths are preferred for LII measurements. However, in Paper II LII experiments are presented, which were performed using a laser operated at 532 nm. A correction procedure was designed to remove the contribution of PAH-LIF in the LII signal which has been described in detail in section 4.2.1.

Attenuation system

The laser beam from the outlet of the Nd:YAG laser system generally has a predominant polarization, either vertical or horizontal. The attenuation system shown in Fig. 3.6 uses the polarization of the laser beam to control its pulse energy.

This system comprises of a half-wave plate placed in between two linear polarizers. A half-wave plate is an optical component which can rotate the polarization of the incident light while a linear polarizer is an optical component which transmits only a specific polarization. To understand the operation of the attenuation system, let us assume the laser output is predominantly vertically polarized. The linear polarizers are mounted such that they transmit only the vertically polarized light and reflect the horizontally polarized light. The unpolarised laser beam (although assumed to be predominantly vertically polarized) was sent through the first linear polarizer which transmits only the vertically polarized component. This vertically polarized laser beam is then sent through a half-wave plate. By adjusting the angle of rotation of the half-wave plate, one can control the proportion of the vertically and horizontally polarized light. As the second linear polarizer only transmits vertically polarized light, one can effectively control the energy of the laser just by rotating the half-wave plate. The unique advantage of using this method to control the laser energy is that one can vary the pulse energy without causing any variation in the spatial and temporal energy profile of the laser beam.

Beam Shaping System

All the LII-based studies reported here involved 2D LII measurements and hence the laser beam was shaped into a thin laser sheet focused at the centre of the burner/combustion system. First, the laser beam was expanded vertically using a negative cylindrical lens (plano-concave, f = - 20 mm) and later collimated in the height direction using a positive cylindrical lens (plano-convex, f = + 200 mm). This expanded laser beam is focused in the horizontal direction using another positive cylindrical lens (f = + 500 to + 2000 mm), so that the beam waist is formed at the centre of the burner/combustion system. A more detailed discussion of the effects of the focusing optics on LII can be found in Paper I and section 4.1. The laser sheet was also clipped in the vertical direction to the desired height using an aperture. As all the LII-based studies in this thesis used a Gaussian sheet profile, the beam or sheet was not clipped in the horizontal direction. Figure 3.8a shows the spatial intensity distribution of a Gaussian sheet at the focal plane detected using a beam profiler camera. From Fig. 3.8 b and c, it can be seen that the laser intensity follows a Gaussian profile in the horizontal direction while, the intensity remains fairly constant along the vertical direction.

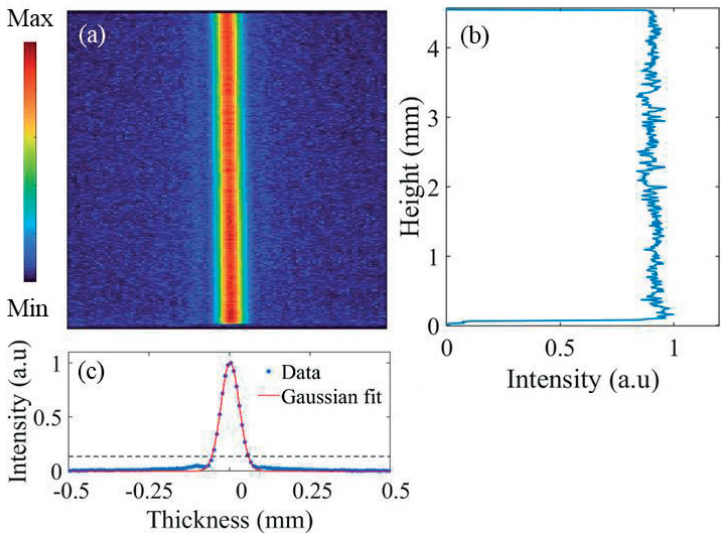

Figure 3.8: **(a)** Spatial intensity distribution of a Gaussian laser sheet imaged using a beam profiler camera. **(b)** Intensity profile along the height direction. **(c)** Intensity profile along the horizontal (thickness) direction. A Gaussian curve has been fitted to the experimental data.

LII Signal Acquisition System

As the high energy laser sheet passes through the sooting region in the flame, soot incandesces and the resulting LII signal is emitted in all directions. The radiation emitted in the direction perpendicular to the propagation direction of the laser sheet is collected using an intensified charge coupled device (ICCD camera). A Princeton Instruments ICCD (PIMAX 4) was used for all the measurements presented in this thesis. Sufficiently high quantum efficiency in visible (~ 50 % at 500 nm) and the UV (~ 15 % at 350 nm) region added with the capability to acquire signals using extremely short gate widths (minimum 1.1 ns) makes this camera a good choice for LII signal acquisition. The double-imaging feature which gives the capability to acquire 2 single-shot images in quick succession (~ 2.2 μs) is also useful for measurements in turbulent flames. Here, the first image acquires the background luminosity, while the second image acquires the LII signal. This helps in performing background subtraction on a shot-to-shot basis. This improves the accuracy of the measurement cases where the background luminosity continuously varies, for example, in turbulent flames.

Choosing an appropriate gate width is critical for gated LII measurements. Short gate widths on the order of 20 – 50 ns are preferred for LII measurements to optimise

between increasing the signal strength and reducing the interference from background flame luminosity [17]. Additionally, LII signals acquired using longer gate widths diminish the contribution of smaller soot particles to the LII signal due to their higher conduction heat losses and thereby faster decays (Fig. 3.3). This could have consequences in the quantification of the 2D LII signal. For instance, two regions with the same soot volume fraction but with different size distributions could potentially show differences in the LII signal when a considerably long gate width is used.

All the LII measurements in this thesis were done using prompt detection of the signal, i.e. detection of LII during the laser pulse. Although delayed detection is a way to remove PAH-LIF interference from the LII signal, this procedure has been found to create uncertainties in quantification [47], which has to be taken into consideration when planning for such an experiment. The correction procedure used to remove PAH-LIF interference for the work in Paper II has been described in section 4.2.1. The laser and the ICCD were synchronised using a BNC Model 575 pulse generator (average jitter = 50 ps). The approximate temporal location of the LII signal can be found either by using a PMT and oscilloscope setup or, by using the ICCD itself, but with great caution to avoid saturation of the detector. Once the approximate location of the LII signal was determined, the gate width was set to a low value (2 ns) and the position where the LII signal first start to appear was examined. The starting location of the measurement gate was chosen to be 2 ns before this temporal location.

As a general procedure, hundreds of single-shot LII images were averaged to improve the signal-to-noise ratio in the detection. Averaged background luminosity images were also acquired and were used for background subtraction. For the LII measurements performed in laminar flames (Papers I and II), background luminosity images were acquired right after the acquisition of the LII signal images. At least 300 two-dimensional single-shot LII images were acquired using the ICCD camera for each case and averaged to obtain mean LII signal images. However, for turbulent flames (Paper V), the mean background luminosity image might not be representative of the instantaneous flame structure and hence using mean image for background subtraction could lead to uncertainties in the measurement. Hence for measurements in turbulent flames, single-shot background luminosity images were acquired ~ 2.2 μs before the LII signal image and background subtraction was performed on a shot-to-shot basis (section 4.4.2). Around 70 – 80 images were only used for averaging for the LII measurements in the optical engine (Paper V) due to operational constraints.

As mentioned previously, LII signal is Planck radiation in itself and is broadband. There are a few factors to consider while choosing wavelength ranges for detection of LII signals. Soot at flame temperatures radiate strongly and gives a natural background luminosity in the LII signals. Since soot particles producing LII signals are at a much higher temperature, their Planck radiation emission shifts to shorter wavelengths compared to that of soot particles in flame which were not illuminated with the laser. Thus, it is always advisable to acquire the LII signals at low wavelengths (450 nm or below) to improve the signal-to-noise ratio.

3.2.4 Uncertainties

LII is a powerful technique to obtain quantitative information on soot in a combustion system. However, one must be careful during the measurements to avoid or mitigate the potential uncertainties. In the works mentioned in this thesis, LII has been used to evaluate soot volume fractions and, LII fluence curves are used to estimate the absorption function, $E(m)$. The uncertainty discussion here, thus primarily deals with these two aspects.

As mentioned before, laser fluence is an important parameter in LII measurements and there are several factors that could influence the uniformity of laser fluence over the whole imaging region. Depending on the fluence used for measurements, and its position in the fluence curve, this could potentially result in significant uncertainties in LII measurements. Some of the factors which influence the laser fluence are laser energy attenuation along the propagation direction of the laser, optical components in the system which distorts the laser sheet, varying thickness of the laser sheet along the propagation direction due to the focusing optics, non-uniform spatial distribution of laser sheet, pulse to pulse variation in laser energy, etc.

While using a spatial energy profile of a Gaussian sheet, small spatial variations in the laser fluence due to laser energy attenuation can be mitigated by choosing a high enough laser fluence in the plateau region of the fluence curve. It is tricky to perform corrections for this attenuation, especially when the flame is turbulent, and the attenuation is non-uniform. Uncertainties due to small non-uniformities in the spatial profile of the laser can also be mitigated by choosing a high laser fluence lying in the fluence plateau. The uncertainties due to the focusing optics in quantitative 2D LII measurements have been discussed in detail in Paper I. Uncertainties due to pulse-to-pulse fluctuations in laser energy can be minimised by averaging over large number of single-shot images.

Laser wavelengths in the visible and UV regions when used for LII measurements also induce fluorescence from PAHs which interferes with the LII signal. Using a delayed detection to avoid the short-lived PAH-LIF signals (~ 20 – 30 ns), has been suggested as one of the ways to mitigate this. However, this method will have a bias towards larger particles as the LII signals from smaller particles decay much faster [47]. Another way to make corrections for the PAH-LIF interferences in the LII signal has been discussed in detail in Paper II and in section 4.2.1.

Limited knowledge about the optical properties of soot, for example described through the absorption function ($E(m)$), is one of the major factors introducing uncertainties in quantitative LII measurements. Most of the studies in the literature assume a constant value for $E(m)$ for the whole imaging region [44, 66-72]. However, it has been shown that the value of $E(m)$ increases with increase in soot maturity [17]. Since soot maturity might vary between different locations in a flame, choosing a single value for $E(m)$ for the whole imaging region might overestimate or underestimate the derived soot volume fractions at different regions. Additionally, the $E(m)$ value of mature soot has been reported in the range from 0.29 to 0.52 in the literature [22], although several studies suggest a value of 0.35 [23, 24].

Beam steering and signal trapping are other sources of uncertainties in 2D LII measurements [66]. Beam steering is caused due to density gradients in the system causing variations in refractive indices of the medium resulting in the deviation of laser beam/sheet propagation from its intended path. Beam steering is a common source of uncertainty in high pressure systems, highly turbulent flames, systems with large temperature gradients, etc. Another source of uncertainty in highly sooty flames is signal trapping [66], which means that the signal gets trapped or absorbed by the soot particles on its way to the detector.

Effective subtraction of background luminosity is essential in performing accurate LII measurements. For a stable laminar flame, it is often adequate to acquire the background luminosity separately and subtract it from the signal. However, for a turbulent flame, this becomes tricky as background luminosity changes on a shot-to-shot basis. Hence, for the measurements in a diesel engine discussed in Paper V, background luminosity images were acquired ~ 2.2 μs before each single-shot LII signal image and subtracted on a shot-to-shot basis (section 4.4.2).

3.3 Laser-induced Fluorescence

Laser-induced fluorescence has been widely used in detecting species in flames [73-75]. The concentration level of the species can be down to hundreds of ppb. LIF has been used to detect OH [76, 77], formaldehyde [75, 76], CH [78], acetone [77], etc.

Laser-induced fluorescence is one of the most important optical diagnostic techniques for studying polycyclic aromatic hydrocarbons (PAHs). As PAHs are considered as soot precursors and hence an important step in the soot formation process, it is important to have a good understanding on PAH formation in sooting flames. PAHs have high absorption coefficients and quantum yields and hence, they are good candidates for investigations using laser-based diagnostics.

PAHs are found to fluoresce using a wide range of excitation wavelengths in the ultraviolet (UV) spectral region as low as 250 nm [79] to the visible region as high as 680 nm [8]. Generally, excitations using longer wavelengths excite larger PAHs with more aromatic rings. For example, laser excitation using 355 nm is considered to excite PAHs with more than 3 aromatic rings [80]. However, most of the PAHs, irrespective of their size, are likely to have absorption bands around 266 nm [8]. Moreover, laser excitation using 266 nm has been found to produce bimodal fluorescence spectra in sooting flames with a peak around 320 nm, and a broad emission in the visible range between 400 nm and 600 nm [81-84]. Various PAH molecules have shown to have fluorescence spectra which are broad and overlapping with each other [85]. Furthermore, PAH-LIF spectra also depend on the excitation wavelength [79], temperature [85, 86], etc., thus making it hard to determine the types of PAHs in a flame purely from the LIF spectra. However, the LIF emission in the UV region is regarded to be emitted by the PAHs with two to three rings, while those in the visible region correspond to PAH species with higher molecular weights [81, 83, 87, 88]. In general, the fluorescence response of PAHs shift towards longer wavelengths as the molecular size increases [80, 89, 90].

3.3.1 Experimental Setup

The schematic representation of a PAH-LIF setup is given in Fig. 3.9 where excitations can be performed using either 266 nm or 532 nm laser wavelengths. Nd:YAG lasers (Quantel Brilliant b, 10 Hz) operated in second and fourth harmonic modes were used for generating 532 nm and 266 nm laser beams. Potentially

remaining 1064 nm laser radiation mixed with the 532 nm laser beam, and 1064 and 532 nm laser radiation superimposed in the 266 nm laser beam, need to be removed using, for example, dichroic mirrors to avoid signal interferences in the PAH-LIF signal. This has been discussed in detail in Paper III. The attenuation system used for the 532 nm laser beam is similar to that discussed in section 3.2.3. Laser beams were shaped into a laser sheet using the combination of a UV cylindrical lens (f = -40 mm) and a UV spherical lens (f = + 500 mm).

Spectral measurements of PAH-LIF can be performed using various beam configurations. In the work presented in Paper III, spectral measurements of PAH-LIF were done using an unfocused laser beam. In such measurements, one must ensure that low laser fluences are used to avoid incandescence, especially for the 266 nm laser beam. Laser fluences of ~ 0.02 J/cm^2 and ~ 0.004 J/cm^2 were used for the excitation wavelengths of 532 nm and 266 nm, respectively.

The signal acquisition system of 2D PAH-LIF is quite similar to that of LII as described in section 3.2.3 in terms of the ICCD, finding the location of the gate, etc. A short gate width of 30 ns was used for signal acquisition of the PAH-LIF signals, as they generally have durations of the order of ~ 20 - 30 ns [17]. Wavelengths used for detection can be used for size-selection of PAHs when using 266 nm as the excitation wavelength. This has been discussed in detail in Paper III.

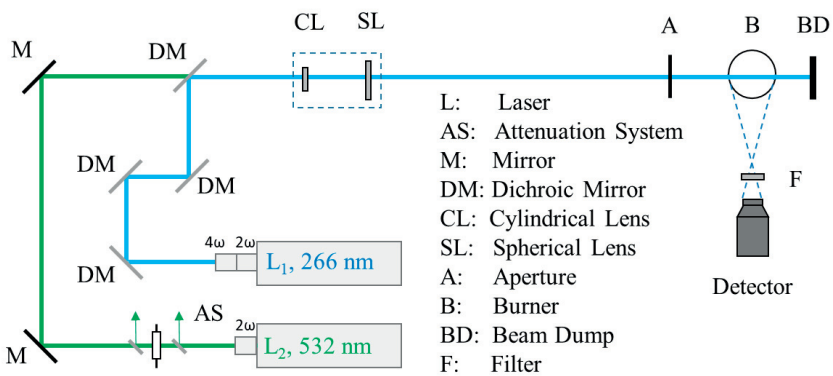

Figure 3.9: Schematic representation of a PAH-LIF set-up using the excitation wavelengths 532 nm and 266 nm.

3.3.2 Uncertainties

Quantitative PAH-LIF measurements in flames have several uncertainties due to the overlapping LIF spectra of different PAHs, lack of information about the LIF spectra of different PAHs at flame conditions (high temperatures), their dependence on temperature and excitation wavelength, etc. Several of the uncertainties associated with LII measurements mentioned in section 3.2.4 are applicable for PAH-LIF measurements as well. Issues such as the presence of spatial non-uniformities in the laser sheet profile, beam steering, signal trapping, etc. could cause uncertainties in the measurements. As measurements were performed in stable flames for the work reported in Paper III, beam steering was found to be minimal. It is difficult to characterize signal trapping as the absorption properties of PAHs at all wavelengths are not known. Despite the limitations of spectral overlap for different PAHs and uncertainties in absorption efficiencies, relative PAH concentrations can be measured and compared.

3.4 Elastic Light Scattering (ELS)

Elastic light scattering (ELS) is a process that occurs for molecules as well as for soot particles, in which the scattered light has the same wavelength as the incident light. In soot-laden media, often the ELS from soot is several magnitudes stronger than the ELS from the molecules. ELS, when combined with other techniques such as LII or extinction can be used for obtaining information on the particle size, aggregate properties, etc. [24, 30, 91]. ELS signals from soot are often presented in terms of the parameter called the *scatter factor* or Q_{vv}. Here, the two v's indicate the polarization of the scattered photons observed by the detector and the polarization of the incident beam, respectively. If one assumes soot particles to be spherical and monodisperse,

$$Q_{vv} = N\left(\frac{2\pi}{\lambda}\right)^4\left(\frac{d_p}{2}\right)^2\left|\frac{m^2-1}{m^2+2}\right|^2, \tag{3.25}$$

where N, λ and d_p are the particle number concentration, laser wavelength and the primary particle size, respectively. The parameter $|(m^2-1)/(m^2+2)|^2$ is a function of the complex refractive index of soot (m), called $F(m)$.

Calibration of the ELS signals detected by the detector (often ICCD cameras or photomultipliers) to Q_{vv} is done by performing ELS measurements on nitrogen or

air, for which the values of the Q_{vv} factors are known for a given temperature and pressure. The calibration factors are thus obtained and the ELS signals from soot measurements are later converted in terms of Q_{vv} factors.

3.4.1 Experimental Setup

A schematic representation of an optical setup used for the work presented in Paper III, is given in Fig. 3.10. This setup is similar to the LII setup shown in section 3.2.3, apart from a few differences. A laser wavelength of 532 nm is often used for ELS instead of 1064 nm, because of the availability of efficient detectors in the visible range, for example ICCD-cameras. The attenuator system can control the pulse energy while also ensuring that the laser beam is vertically polarized as this is an essential requirement for obtaining strong elastic light scattering in the orthogonal direction to the propagating laser beam. A low laser fluence of ~ 0.02 J/cm^2 was used to avoid incandescence from soot particles.

Various optical filters are placed in front of the detector while acquiring the ELS signal. A linear polarizer rotated at an angle to transmit the vertically scattered photons, along with a band-pass filter at a wavelength of 532 nm are the two important optical components used for ELS measurements. Additionally, various neutral density filters are also used to prevent signal saturation of the ICCD camera. A short gate width of 20 – 30 ns is preferred for ELS signal acquisition to minimize the contribution of flame luminosity.

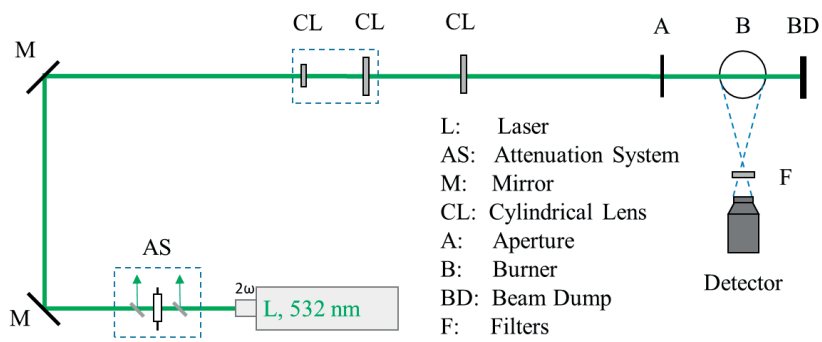

Figure 3.10: Schematic representation of an ELS setup.

3.4.2 Uncertainties

In all the works mentioned in this thesis, results from ELS measurements are reported in terms of Q_{vv} factors, and further analysis leading to obtaining primary particle sizes or aggregation properties have not been performed. Evaluating primary particle sizes using ELS and LII measurements involves several uncertainties related to the choice of the refractive index of soot, aggregation of soot, etc. More details can be found in [28]. Other common uncertainties related to laser diagnostics have been discussed in section 3.2.4.

3.5 High-Speed Imaging Measurements

High-speed imaging techniques are the ones where the image acquisition is at frame rates generally over 1 kHz. Such techniques are especially useful for studying fast processes or transient phenomena, such as the combustion processes in an internal combustion engine, fuel injection in a diesel engine, etc. [92]. In the works involved in this thesis, high-speed imaging measurements of Mie scattering, and flame luminosity have been performed.

3.5.1 Mie Scattering

Mie scattering is a useful technique to study spray formation in diesel engines. The Mie scattered signal occurs at the same wavelength as the incident light, and for light-droplet interaction, it can be described by Lorenz-Mie theory [93]. The light-droplet interaction falls into three light scattering regimes based on the size parameter 'x'. These regimes are:

$x \ll 1$: Rayleigh scattering regime,

$1 < x < 100$: Mie scattering regime, and

$x > 100$: Geometrical optics regime.

Here, x is given as,

$$x = \frac{\pi d}{\lambda} \tag{3.26}$$

where, d is the droplet diameter and λ is the wavelength of the incident light. Although quantitative evaluation of spray sizes can be done by combining the

scattering measurements with LIF measurements of sprays, Mie scattering has been used for qualitative analysis in the work presented in this thesis, see Paper IV.

Experimental Setup

As mentioned in section 2.3.2, Mie scattering measurements were performed by introducing EGR to create a non-reactive environment inside the combustion chamber. Figure 3.11 shows the schematic of the experimental setup for the high-speed imaging measurements of Mie scattering presented in Paper IV. Measurements were performed in a light-duty Volvo optical diesel engine described in section 2.3.2. A continuous wave diode laser (~ 3 W) operated at a wavelength of 452 nm was used to illuminate the combustion chamber of the optical engine. A positive cylindrical lens was used to restrict the expanding laser beam to match the shape of the optical window. The optical window acted as a diverging lens to further expand this rectangular laser beam as shown in Fig. 3.11b. The top surface of the combustion chamber was coated with graphite spray to reduce strong reflections from metal surfaces.

A Photron SA5 high-speed camera with an UV objective lens (B.Halle, f = 100 mm) was used for acquiring the 2D Mie scattering signals. The camera was operated at 25,000 frames per second (fps) with a gate width of acquisition of ~ 40 μs. Additionally, a band-pass filter at the wavelength 452 nm (FWHM = 22 nm) was placed in front of the detector.

Uncertainties

The Mie scattering measurements presented in Paper IV was used for qualitative analysis. However, there are still some uncertainties due to various factors. Firstly, the illumination might not be uniform for all sprays. Hence, it might be difficult to characterize the symmetry of a spray using the Mie scattering signals. Due to this reason, the main analysis has been performed on one of the eight sprays for which there is strong illumination at all times during the injection process. Another uncertainty is due to the image distortion caused by the shape of the optical piston. This has been corrected using a distortion correction procedure described in Paper V.

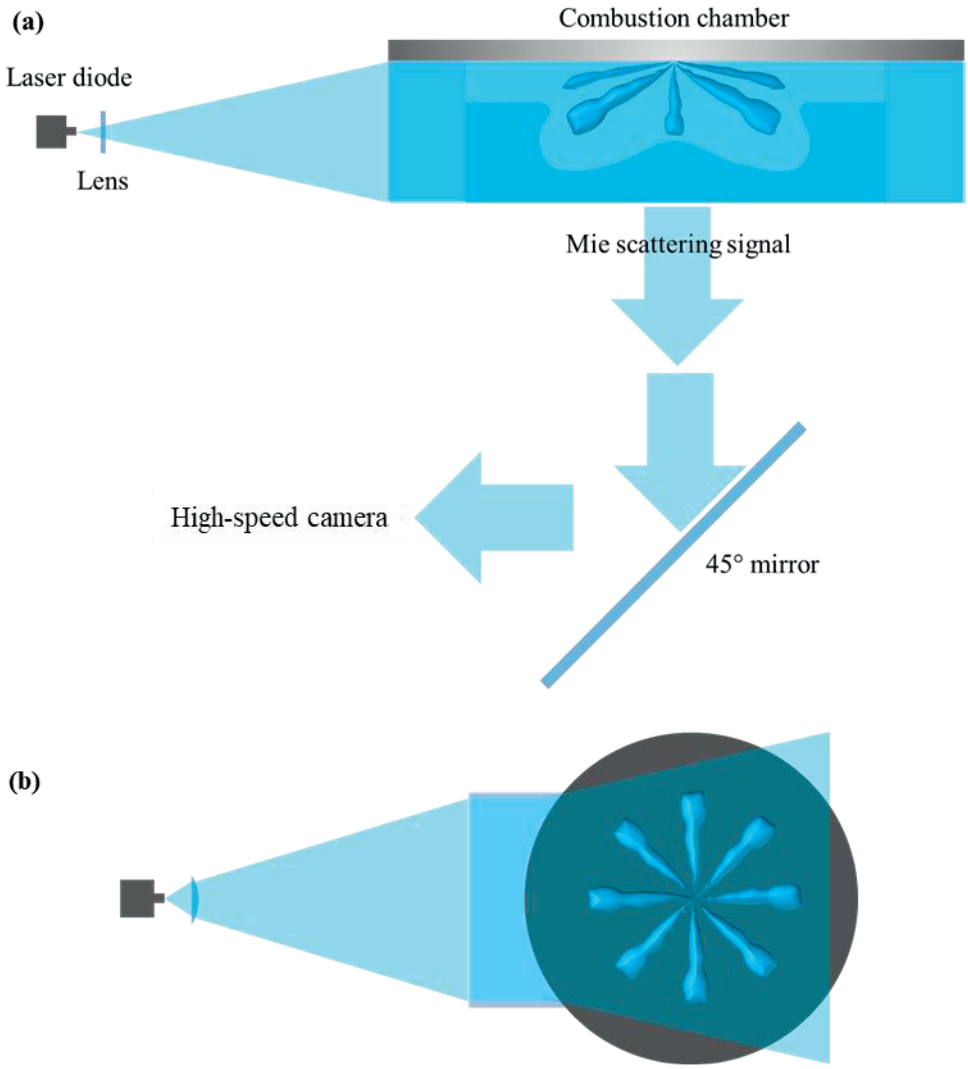

Figure 3.11: Schematic of the experimental setup for high-speed imaging measurements of Mie scattering performed in an optical diesel engine (Inspired from Lonn et al. [94])

3.5.2 Flame Luminosity

High-speed imaging of flame luminosity (or natural luminosity, NL) is another useful diagnostic tool in studying combustion processes in transient environments like in a diesel engine. Although NL from a combustion system consists of chemiluminescence as well, the predominant contribution in sooty flames as in

Diesel engines, comes from the heated soot particles. NL of hot soot in the flame is often used to characterize the global flame structure, and as a first-step diagnostic tool before using more advanced laser diagnostic techniques. This thermal emission from hot soot particles has also been used to study soot formation and oxidation, along with the evaluation of soot concentration and temperatures [95-98].

Experimental Setup

The experimental setup for the NL measurements is quite similar to that of the Mie scattering measurements described in section 3.5.1 with only a few differences. The most significant difference is that no laser source was used for the flame luminosity measurements. Also, in addition to the band-pass filter at 452 nm, various OD filters were also used to avoid saturation of the detector (Photron SA5 camera).

Uncertainties

Natural luminosity measurements in the works mentioned in this thesis were used for qualitative analysis. However, there are certain factors which might cause uncertainties in the measurements. As the NL emission from soot is sensitive to its temperature, a uniform soot distribution with a non-uniform temperature distribution will give non-uniform distribution of NL emission. This might cause uncertainties in the results if the information on temperature distribution is not available. Moreover, there might also be issues due to non-uniform signal trapping, some of the regions being out of focus in the camera (at late cycle), etc. However, the focus of the camera was optimised to minimise this effect. Natural luminosity measurements are also troubled with image distortions caused due to the curvature of the optical piston. The procedure to correct for this distortion has been discussed in Paper IV.

4 Results and Discussion

In this chapter, the main results from the works involved with the Papers I – V have been presented. Additionally, some interesting results which were not presented in the Papers have been added here. However, all results which are presented in the Papers have not been reported in this chapter to avoid repetition.

4.1 Effects of Laser Focusing Optics on LII

Two-dimensional LII has been one of the most important diagnostic tools in the past couple of decades in obtaining quantitative information on soot [17, 27]. Measurements based on 2D-LII have been commonly used for obtaining 2D soot volume fractions (f_v) [17, 47]. Although 2D LII has been widely used in laboratory scale and practical combustion systems, there are several challenges in performing accurate quantitative measurements. More details on LII, including some of these challenges such as attenuation of laser energy along the beam path, signal trapping, and beam steering have been discussed in detail in section 3.2. In this section, the issues created due to the varying laser sheet width in the imaged region along the beam propagation direction caused due to the laser sheet focusing optics have been discussed.

In this study, we used a one-dimensional flame in which a homogenous soot field was created. For this, low sooting premixed ethylene-air flames (ϕ = 2.1, maximum f_v < 60 ppb [31]) were stabilized on a McKenna burner as discussed in section 2.3.1. At the HAB of 14 mm, where the main analysis was done, the extinction of the laser beam across the flame was 1.8 %. Hence, one can assume negligible influence of laser energy attenuation along the beam path as well as negligible signal trapping.

LII measurements were performed using a Nd:YAG laser operated at 1064 nm. The LII setup was discussed in detail in section 3.2.3, and specific details on this setup can be found in Paper I. After expanding the laser beam in the height direction using two cylindrical lenses (f = - 19 mm, f = + 200 mm), a cylindrical lens with a focal

length of + 500 mm (denoted as f500 lens) was used to focus the laser sheet along the thickness direction. Along the propagation direction of the laser 'z', the thickness of the laser sheet ('x') was measured using a beam profiler camera. The location $z = 0$ represents the location of minimum thickness of the laser sheet, and this was positioned to coincide with the centre of the burner. The variation of laser sheet thickness along the propagation direction of the laser is shown in Fig. 4.1b, and the resulting fluence distribution at $z = 20$ mm and $z = 0$ is shown in Fig. 4.1a. One can notice that the laser sheet profile is fairly Gaussian. The width of the laser sheet, which was evaluated as the width at $1/e^2$ (13.5 %) of the maximum intensity has also been marked in Fig. 4.1a.

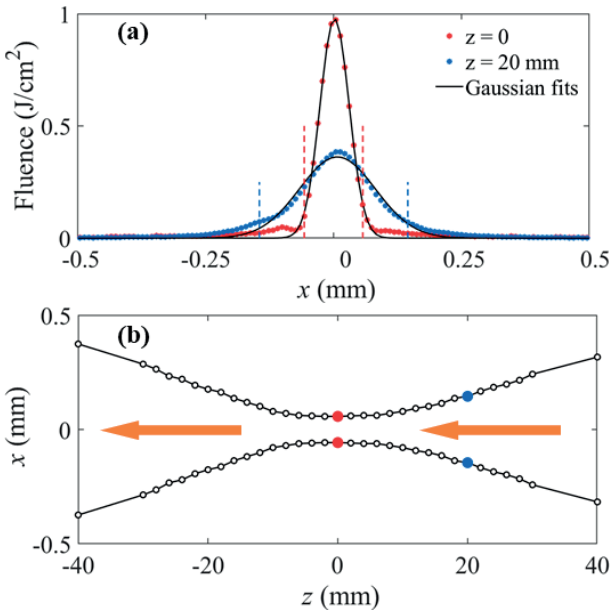

Figure 4.1: **(a)** Laser fluence profile for a pulse energy of 11.2 mJ at $z = 0$ and $z = 20$ mm, where 'z' is distance along the propagation direction of the laser (marked by arrows in (b)). Gaussian fits of the fluence distribution have also been marked along with the sheet widths. **(b)** Laser sheet profile along z. 'x' represents the width of the laser sheet.

LII measurements were performed using 10 different laser pulse energies ranging from 2.24 mJ to 22.4 mJ, which correspond to mean fluences of 0.12 J/cm^2 and 1.22 J/cm^2 respectively, at $z = 0$. The values of all the ten fluences named as F1 to F10, are given in Table 4.1. Four different gate widths (10 ns, 30 ns, 50 ns, 100 ns) were also used for acquiring the 2D LII signals.

Table 4.1: Laser pulse energies and the corresponding mean laser fluences at z = 0 used for LII measurements.

Symbol	Total pulse energy (mJ)	Mean fluence at z = 0 (J/cm^2)
F1	2.24	0.12
F2	4.48	0.24
F3	6.72	0.37
F4	8.96	0.49
F5	11.2	0.61
F6	13.4	0.73
F7	15.7	0.86
F8	17.9	0.98
F9	20.2	1.10
F10	22.4	1.22

All the remaining analysis in this work have been performed at an HAB of 14 mm. The LII model introduced in section 3.2.2, was used to simulate the LII signals obtained from measurements at 14 mm HAB, using the properties of soot and ambient conditions summarised in Table 3.1 (also Table 2 in Paper I). For the LII model evaluations, Gaussian distributions of laser fluences were generated for each z location with the sheet thickness from Fig. 4.1b. Various points in the distribution were spatially equidistant from each other (separation ~ 2.3 μm) as shown in Fig. 4.2. In order to simulate the LII signal in an imaging experiment at 90 degrees detection from the propagating laser beam, the LII signal from a z location was obtained by adding the modelled LII signals evaluated at these individual points using their corresponding laser fluences. The LII signals generated from the LII model were found to be matching with the corresponding signals obtained from measurements (Figs 4 & 6 in Paper I).

Figure 4.3 shows the measurement and modelled LII fluence curves at an HAB of 14 mm while using the f500 lens for the fluence cases F4 and F6. Ideally, the LII signal profiles should be constant along z as the soot distribution is uniform in the region shown in Fig. 4.3. The variation is mainly caused due to the variation in the thickness of the laser sheet along z. The LII signal at z = 20 mm was found to be around 2.4 and 1.9 times stronger than the signal at z = 0 for the 30 ns case. This is mainly due to a combination of two factors. The first one is the presence of a larger probe volume for z = 20 mm compared to z = 0. Meanwhile, the second factor is the presence of a much higher peak fluence for the z = 0 location compared to that at z = 20 mm, which results in a much higher sublimation at z = 0 leading to a drop

in the LII signal. Nevertheless, from Fig. 4.3, it can be seen that the use of f500 lens for LII measurements produces large bias in the signal distribution.

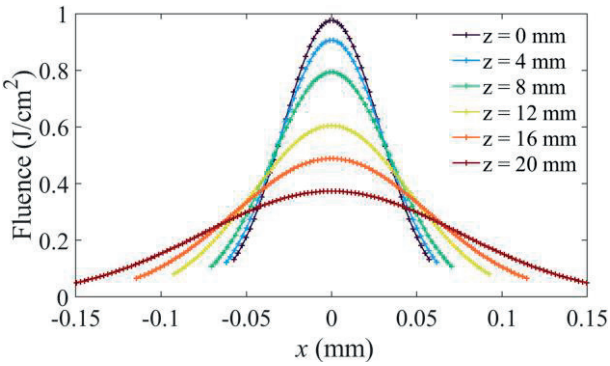

Figure 4.2: Modelled distribution of laser fluence along the thickness (x) direction for different locations along the propagation direction of the laser (z). Total LII signal at a particular z location was the sum of all the LII signals obtained at the equidistant points marked in the individual curves.

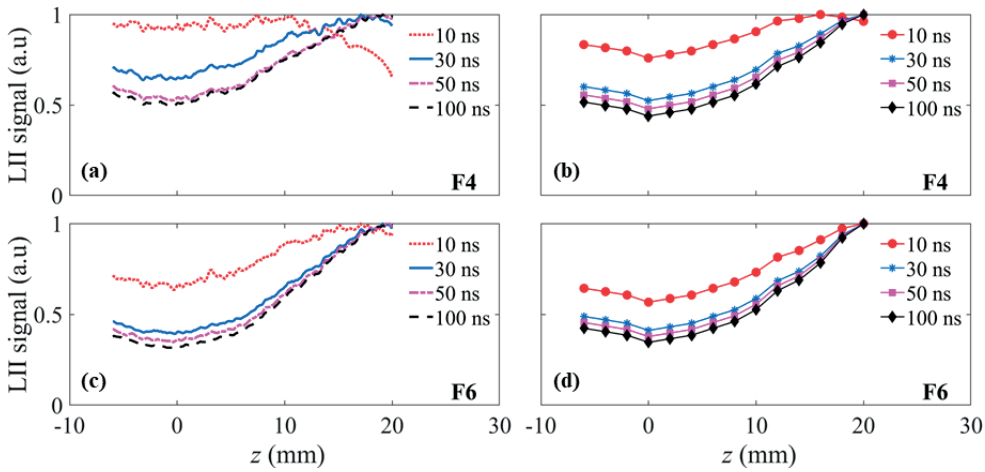

Figure 4.3: LII signal intensities at 14 mm HAB generated from measurements (left) and using the LII model (right) for the fluence cases F4 and F6, which correspond to mean fluences of 0.49 J/cm^2 and 0.73 J/cm^2 respectively, at z = 0. Various curves correspond to different acquisition gate widths. All curves are normalised to the highest signal intensity.

Figure 4.4 shows the variation of *signal ratio*, defined as the ratio between the LII signals at $z = z'$ and $z = 0$ ($2z'$ represents the *image length*, IL), with respect to the FL/IL ratio. The closer the signal ratio is to 1, the lower is the level of bias in the

corresponding LII measurement. The plots in Fig. 4.4 correspond to the fluence cases F4 and F6 for an acquisition gate width of 30 ns. The figure also includes a curve corresponding to modelled data using an f1000 lens. Here, the variation of sheet thickness along the direction of laser beam propagation was modelled using a Gaussian beam propagation model [99] for an f1000 lens (Fig. 7 in Paper I), and later its LII response was evaluated using the LII model (Fig. 8 in Paper I). A first observation from Fig. 4.4 is that, at high FL/IL ratios, the signal ratios remain close to 1. It can also be seen that the measurements and the model for the f500 case match well with each other. One can also observe that the modelled signal ratios for the f1000 lens are slightly lower compared to that of the f500 lens. Thus, for performing 2D LII measurements with minimal bias in the signal distribution due to focusing optics, the first thing to do is to select a lens with as long focal length as possible. After this, other measurement parameters such as the gate widths and laser fluence optimized to minimize the intensity bias in the image.

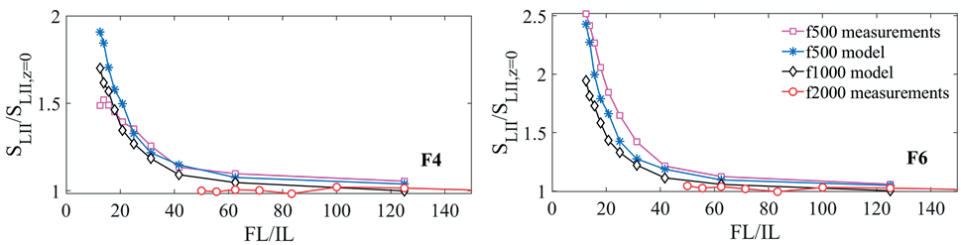

Figure 4.4: Variation of signal ratio (ratio between the LII signals at $z = z'$ and z = 0) in relation to the ratio between the focal length (FL) of the focusing lens and the image length (IL) for various lenses for the fluence cases F4 and F6 (0.49 J/cm^2 and 0.73 J/cm^2 respectively, at z = 0).

Figure 4.5 shows the variation of the signal ratio with the FL/IL ratio for different fluence cases for the modelled f1000 lens and different detection gate widths of 10 ns to 100 ns. One can observe that the low fluence cases such as F1 to F3 show variations in trends for different gate widths at low FL/IL ratios. Meanwhile, the signal ratio for the fluence case F2 remains close to 1 for some detection gate widths even for low FL/IL ratios. This might be misleading as for large image lengths, low fluence cases might be risky as there is a higher probability of laser energy attenuation along the beam path. The laser energy attenuation along the beam path could drastically lead to a strong loss in LII signal intensity across the imaged measurement region. This might create even larger uncertainties, and the trends might tend to those of F1. However, too high fluence case such as F10 also results in large bias for large image lengths. Thus, an optimal laser fluence needs to be selected based on the actual measurement situation to minimize the bias in LII signal

distribution. It can also be seen that at high fluences, for a chosen value of FL/IL ratio, the signal ratio is lower for shorter gate widths. Hence, for a chosen focal length of the lens, the bias in the LII signal distribution can be minimized by using a short detection gate width and an optimal laser fluence.

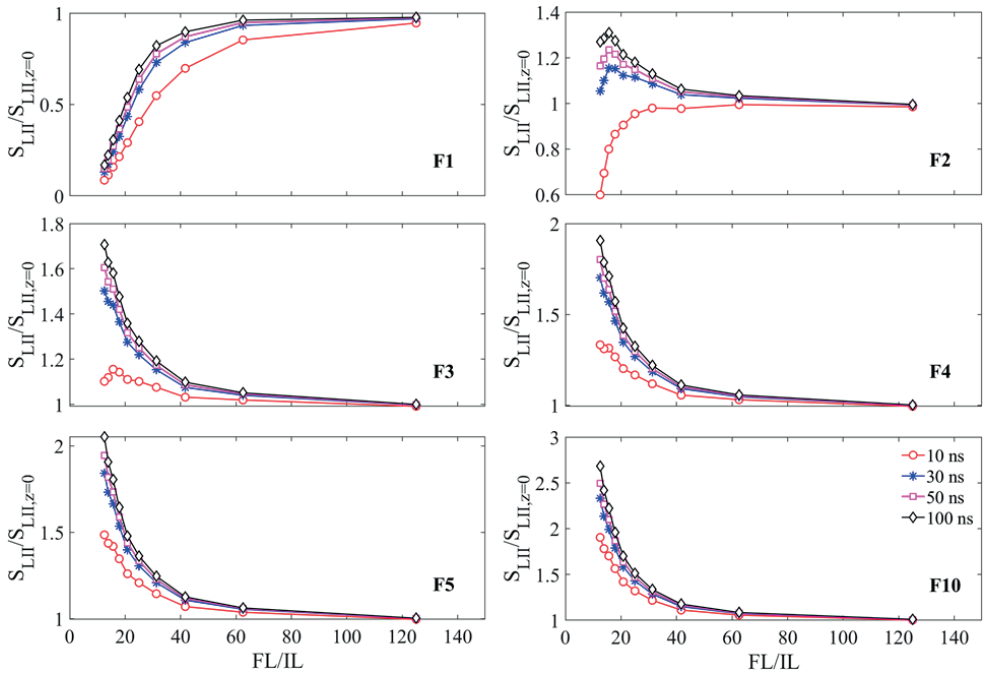

Figure 4.5: Variation of signal ratio (ratio between the LII signals at $z = z'$ and z = 0) in relation to the ratio between the focal length (FL) of the focusing lens and the image length (IL) for various detection gate widths for the modelled f1000 lens for different fluence cases.

It was found that 2D LII-based studies performed in large systems often have underestimated the uncertainties in the LII signal distribution due to the variation of laser sheet thickness along the propagation direction of the laser [44, 67, 100, 101]. For example, there are studies which used an f600 lens for an image length of 40 mm [101], and an f500 lens for an image length of 30 mm [100] resulting FL/IL ratios of 15 and ~ 17 respectively. Another study, although the 2D LII images were used for quantitative analysis used an f2000 lens for an image length of 50 mm, where the FL/IL ratio comes to ~ 13 [44]. Although these studies do not have exactly the same conditions as the present investigation, such low FL/IL ratios could potentially result in significant bias in the 2D LII signal distribution. This bias could

carry forward into the calculated 2D soot volume fraction distributions, evaluated by calibration using extinction measurements, which are generally unaffected by the laser beam width variation. This study, spreads light into the problem caused due to the varying laser sheet width in 2D LII based investigations and the significance of the bias in the spatial distributions of the LII signal. Some ways to mitigate the effects due to this have also been discussed.

4.2 Soot in Laminar Diffusion Flames at Elevated Pressures

Most of the practical combustion devices in the transportation and power generation sectors operate at elevated pressures. To mitigate the soot emissions from these systems, it is important to have a good understanding of soot formation processes at elevated pressures. In the literature, there have been detailed investigations on soot formation in laminar diffusion flames at elevated pressures to understand the effects solely due to pressure [69-72, 102-104]. Spectral soot emission (SSE) [105] and line-of-sight attenuation (LOSA) [106] of soot have been the most prominent techniques used for studying soot formation in elevated pressures to obtain temperature and soot volume fractions (f_v) [69-71, 104]. However, the assumption of constant absorption properties for soot, represented in terms of $E(m)$ values, has been stated as the main uncertainty in these measurements based on SSE+LOSA [69, 104].

As discussed in section 2.2.1, the value of $E(m)$ increases with increase in soot maturity. In the study reported in Paper II, soot absorption properties in methane-air diffusion flames up to 0.5 MPa were investigated. LII, PAH-LIF and extinction were the main diagnostic techniques used in this study. A Nd:YAG laser operated at 532 nm was used for LII and PAH-LIF measurements. As PAHs absorb visible light, the LII signals will face the problem of PAH-LIF signal interference. Delayed detection could be used to suppress the PAH fluorescence as the PAH fluorescence lifetime is on the order of tens of nanoseconds while LII signals have lifetimes on the order of microseconds. However, this procedure was ruled out due to issues with quantification of LII signal to f_v [47]. A correction procedure was devised to remove this PAH-LIF interference from the LII signals.

4.2.1 Removing PAH-LIF signal interference in LII

For removing the PAH-LIF signal interference in LII in the work reported in Paper II, two points along the centreline of the burner, termed as *reference points* were selected. These reference points were selected at low HABs as there is no soot present at these locations, but still with fairly good signal intensities in the 2D LII image. This signal must have originated primarily from the PAHs as LIF. The fluence curve at these reference points were plotted to obtain the relationship of PAH-LIF signal with laser fluence.

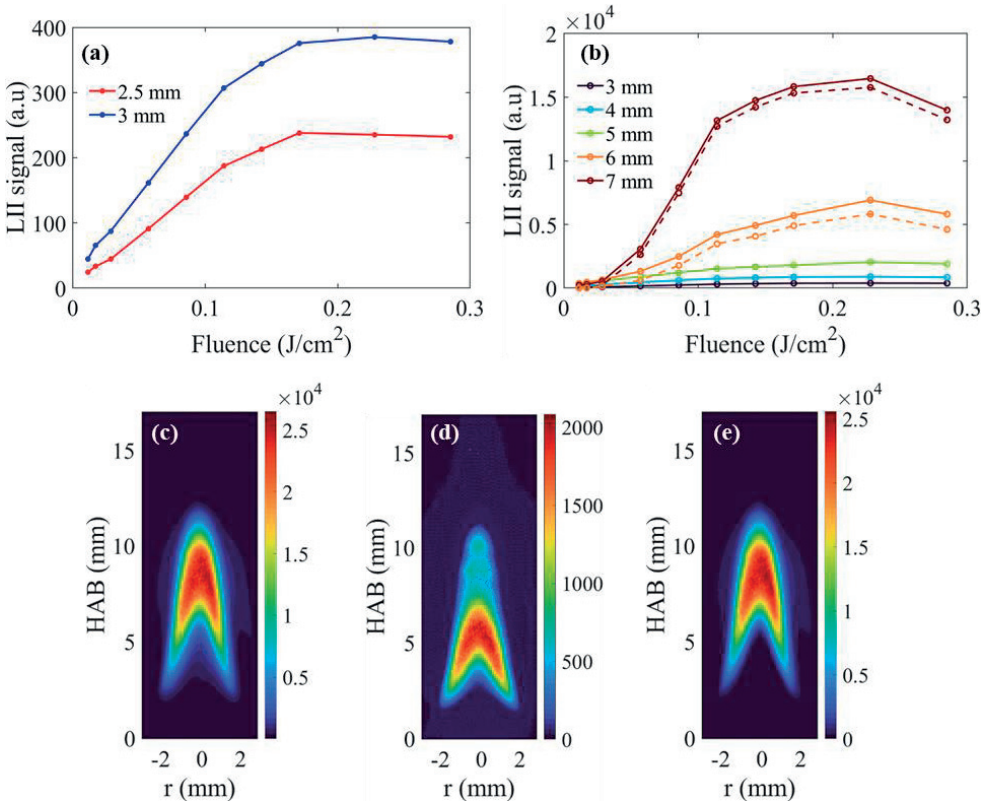

Figure 4.6: Procedure to correct for the PAH-LIF interference in 2D LII signal image for the 0.5 MPa case. **(a)** Fluence curve at the reference points showing pure PAH fluorescence. **(b)** Uncorrected (solid lines) and corrected (dotted lines) LII fluence curves at various HABs. **(c)** Uncorrected 2D LII image at a fluence of ~ 0.17 J/cm^2. **(d)** LIF contribution in the uncorrected image. (e) Corrected 2D LII image.

The fluence curves plotted at the reference points of the 0.5 MPa case are shown in Fig. 4.6a, i.e., showing only PAH fluorescence. Also, the signal intensities in the LII image corresponding to the fluences less than 0.03 J/cm^2 were assumed to be

purely PAH-LIF signals. As both the PAH contribution to LII signals could be established for low fluences and the fluence curve shape was similar for all cases, the PAH-LIF contribution at all the fluences could be estimated. Figure 4.6b shows the fluence curves for the HABs ranging from 3 mm to 7 mm. The solid lines in the plot represents uncorrected LII signals, whereas the dotted lines for the HABs 4 mm and 5 mm represent the LII signal after removing the PAH-LIF interference. Figure 4.6c – 4.6d represent the correction process in 2D LII signal images for the 0.5 MPa case at a fluence of ~ 0.17 J/cm^2. Figure 4.6c, 4.6d and 4.6e respectively represent the uncorrected 2D LII image, the PAH-LIF contribution in the uncorrected image and the corrected 2D LII image.

4.2.2 2D PAH-LIF and Soot Volume Fraction (f_v) Distributions

Figure 4.7 shows the 2D PAH-LIF and f_v distributions (derived from LII) for all the pressure cases. The colour-bars represent f_v in ppm for the right halves of individual images. The PAH-LIF signals, shown in the left halves of the figures, are normalised to the maximum signal intensities of the corresponding images. At all pressures, it can be seen that the PAH-LIF signal increases and reaches a maximum followed by its subsequent decrease. It can also be seen that f_v starts to rapidly increase around this height to reach a maximum, followed by a strong decrease related to soot oxidation. One can also notice the increase in maximum f_v with increase in pressure. Although it cannot be observed in Fig. 4.7, PAH-LIF signals also increase with an increase in pressure.

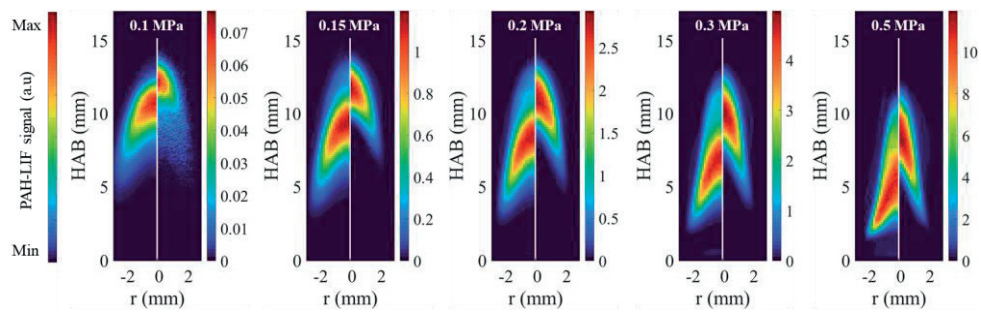

Figure 4.7: 2D PAH-LIF (left half) and f_v (right half) for all the pressure cases. The colour-bars on the right side represent f_v in ppm. PAH-LIF images are normalised to the maximum signal intensity (colour-bar on the left).

After correcting the LII signal images for the PAH-LIF interference, the LII model was employed to estimate the values of $E(m)$ at various spatial locations, as well as to study the variation of $E(m)$ with pressure. This has been discussed in detail in Paper II. It was found that $E(m)$ values of soot at the position of maximum f_v along the centreline (denoted as TP_1 in Paper II) increased with increasing pressure. Soot $E(m)$ values also increased strongly with HAB up to the point of maximum f_v. The impact of the assumption of constant $E(m)$ in SSE+LOSA based studies were also discussed in terms of the exponent x in the expression $f_v \sim P^x$. Despite large differences in $E(m)$, the impact on the pressure exponent was found to be marginal.

4.3 Influence of Salt Additives on PAH and Soot Formation

Due to the non-renewability of fossil fuels, biomass has been suggested as one of the contributors in replacing them [10-12]. It is thus important to have a deeper understanding of biomass combustion, and soot formation in such systems. It is well known that the soot formation process is sensitive to the composition of the fuel. Biomass has various concentrations of trace metals such as potassium (K) and sodium (Na) in addition to carbon, hydrogen and oxygen [107]. Salts of these metals have been found to influence the combustion, including the soot formation process [107-112]. Upon the addition of chlorides of different metal salts, KCl showed considerable reduction in primary particle sizes and soot volume fractions [109, 110]. This was the main motivation to study the influence of various salts of potassium (KCl, KOH, and K_2CO_3) on PAH and soot formation. Salts of sodium, NaCl and NaOH were also used for the study.

Various concentrations of salt solutions, KCl, NaCl, KOH, NaOH, and K_2CO_3, were aspirated into premixed ethylene air flames (ϕ = 2.6) stabilized on a Perkin-Elmer burner. Solutions with concentrations of 1 M, 0.1 M and 0.01 M were aspirated into the flame for all salts except K_2CO_3. As there are two potassium atoms in each molecule of K_2CO_3, solutions with concentrations 0.5 M, 0.05 M and 0.005 M were aspirated leading to the same metal ion concentration in the solution as the other salts. Figure 4.8 shows the flame luminosity images of the reference and salt added cases (case 1 M). Potassium-added flames show a faint bluish glow around the flame while the sodium-added flames show the strong emission corresponding to the sodium D lines (588.9950 and 589.5924 nm). More details on the burner can be

found in section 2.3.1 and in Paper III. However, Paper III only presents the investigations on the influence of the addition of KCl on PAH and soot formation. Although the data evaluation for the salts other than KCl is still ongoing, some of the results are presented here.

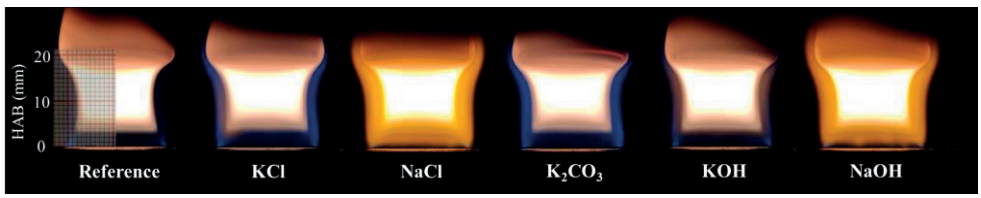

Figure 4.8: Flame images of the reference and the highest concentration cases (1 M) of various salts.

Laser-induced fluorescence of PAHs (PAH-LIF) was the main technique involved in these investigations. Nd:YAG lasers operated at the wavelengths of 266 nm and 532 nm were used for PAH-LIF excitations. Generally, excitations using longer wavelengths tend to excite larger PAHs with more aromatic rings. However, most PAHs, irrespective of their size, are likely to have absorption bands around 266 nm [8]. Furthermore, the fluorescence response of PAHs have been found to shift to longer wavelengths as their molecular size increase [80, 89, 90]. Thus, performing PAH-LIF measurements with the excitation wavelengths 266 nm and 532 nm, and detecting the resulting PAH-LIF signal at different wavelength ranges might provide interesting information on the PAH formation process. In this study, both spectral and 2D imaging measurements of PAH-LIF have been performed. For the 2D imaging measurements with excitation at 266 nm, the PAH-LIF signals have been acquired at 320 nm, and in the region above 385 nm, which are respectively termed as *LIF266-BP320* and *LIF266-LP385*. Here, BP320 and LP385 respectively represent the use of band-pass filter at 320 nm and a long-pass filter with cut-off wavelength at 385 nm. The experimental setup for PAH-LIF measurements have been discussed in detail in Paper III and in section 3.3.1.

4.3.1 Height Profiles

Excitation at 266 nm

Figure 4.9 shows the signal profiles along the centreline for the 2D LIF266-BP320 and LIF266-LP385 measurement cases for all the concentrations of all the salts used in this study. What stands out in the figure is that there are no significant differences

between the different salt concentrations for the LIF266-BP320 signal profiles at higher HABs (> 5 mm). As LIF266-BP320 signal corresponds to smaller PAHs (2 to 3 rings) [81, 83, 87, 88], it can be inferred that addition of K and Na salts do not significantly influence the PAH concentrations at increasing heights above burner (HABs). However, the highest concentration cases (1 M) of all salts show a slight shift in the PAH formation to higher HABs. This will be discussed soon using some results from the ELS measurements.

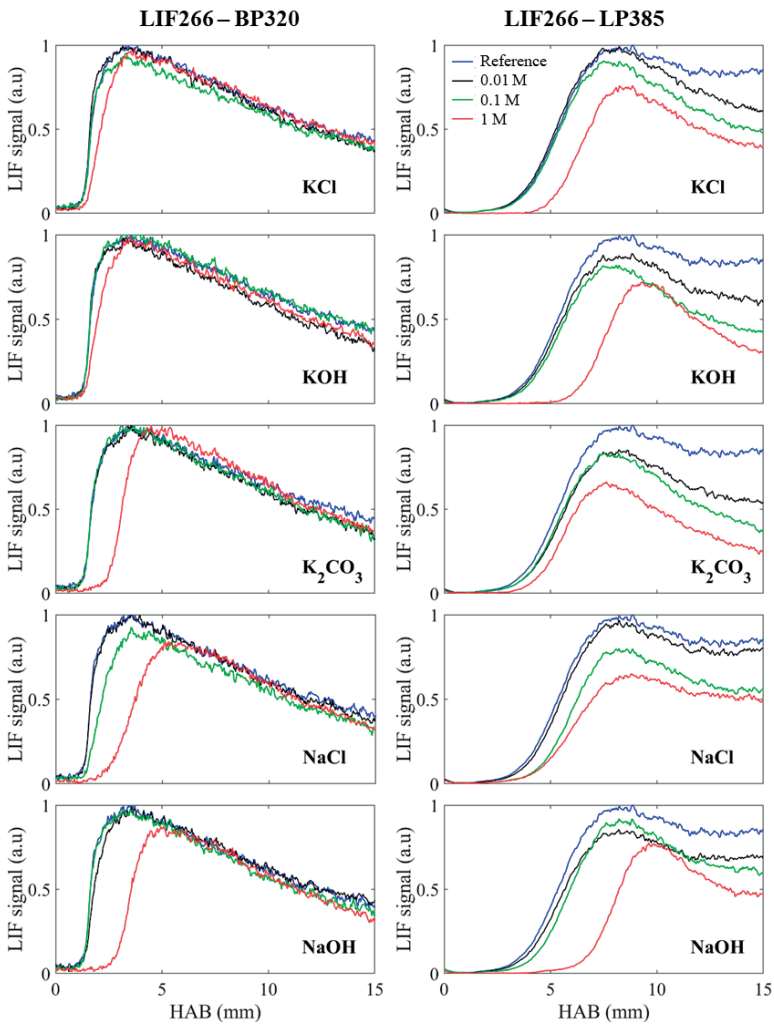

Figure 4.9: LIF266 profiles along the centreline for the BP320 (left) and LP385 (right) cases for 3 different concentrations of the salt solutions and the reference case. Note that for K_2CO_3, the concentrations are 0.5 M, 0.05 M and 0.005 M, respectively. The plots are normalised to the maximum signal of the reference cases.

The LIF266-LP385 case represents larger PAHs [81, 83, 87, 88]. Here, the PAH-LIF signal starts to form at a higher height (HAB ~ 3 – 4 mm) compared to the BP320 cases, rises steadily to reach a peak at around 8 – 10 mm HAB, and then subsequently decrease. Potassium salts show a slightly higher decrease in the PAH-LIF signal after attaining the peak compared to the sodium salts. It can also be seen that there is a successive decrease in the PAH-LIF signal with increase in the salt concentration. This indicates that the addition of potassium and sodium results in a decrease in the concentration of larger PAHs at higher HABs, where a larger influence is shown from potassium addition.

Excitation at 532 nm

The PAH-LIF signal along the centreline of the flame obtained using excitation at 532 nm (termed as *LIF532*) for all the concentrations of all the salts tested is shown in Fig. 4.10. LIF532 is also known to represent larger PAHs [80]. One can also notice that the trends generally resemble the LIF266-LP385 case (Fig. 4.9). However, these two cases do not necessarily represent the same PAH molecules, as the absorption efficiency as well as fluorescence yield of PAHs may vary with excitation wavelength.

Addition of potassium and sodium salts seem to reduce the concentrations of larger PAHs at increasing HABs, where potassium salts have the larger influence. It is also interesting to see that for the respective concentrations, the curves of all the potassium salts KCl, KOH and K_2CO_3 resemble each other irrespective of the negative ions. The same can be observed for NaCl and NaOH. It might suggest that it is primarily potassium and sodium which are responsible for the decrease in the concentration of larger PAHs at increasing HABs. Furthermore, for cases with potassium salt addition the PAH concentration decreases with HAB after attaining the peak, whereas upon the addition of sodium salts, the PAH concentration can be observed to not decrease with HAB after the peak. One can also observe the shift in the LIF signal towards higher HABs for the 1 M cases.

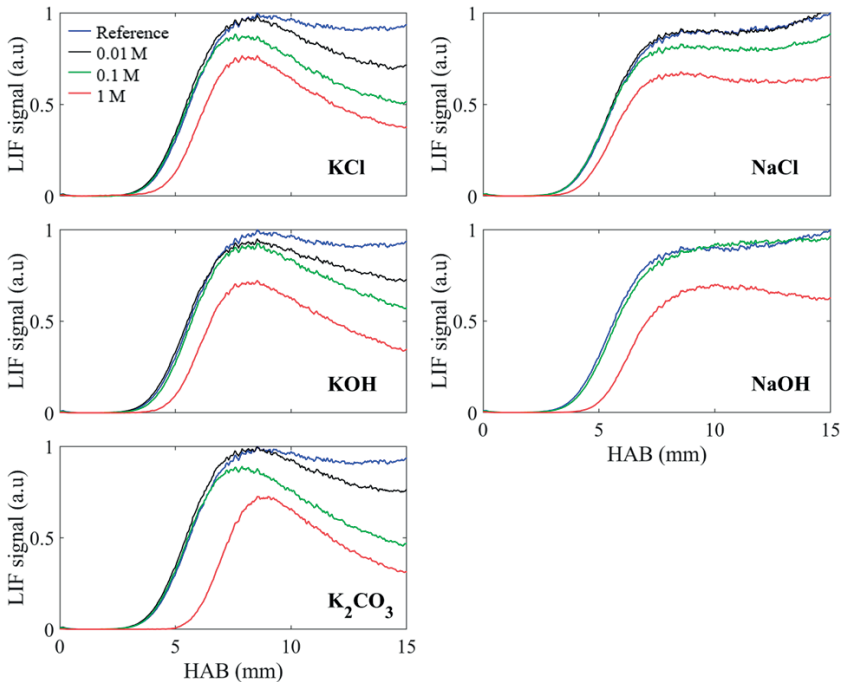

Figure 4.10: LIF532 profiles along the centreline for all concentrations of the salts and the reference case. Note that for K_2CO_3, the concentrations are 0.5 M, 0.05 M and 0.005 M, respectively. The plots are normalised to the maximum signal of the reference cases.

Elastic light scattering (ELS)

Figure 4.11a shows the ELS profiles along the centreline of the burner for the reference case and various concentrations of KCl, while Fig. 4.11b, c, and d show the same for the reference case and the 1 M case of all the salts. From Fig. 4.11a, it can be seen that there is a signal peak at the HAB ~ 1 mm for the 1 M case. From the LII images shown in these former studies [109, 110], this region is prior to the soot formation region. This signal is expected to come from salt particles before they dissociate at higher HABs. This behaviour was also observed in previous studies [109, 110]. Although the full analysis of the ELS signals from all salts is still ongoing, from Fig. 4.11c, one can observe signal peaks at HABs around 1 – 2 mm for different salts. This will be explored further in future work.

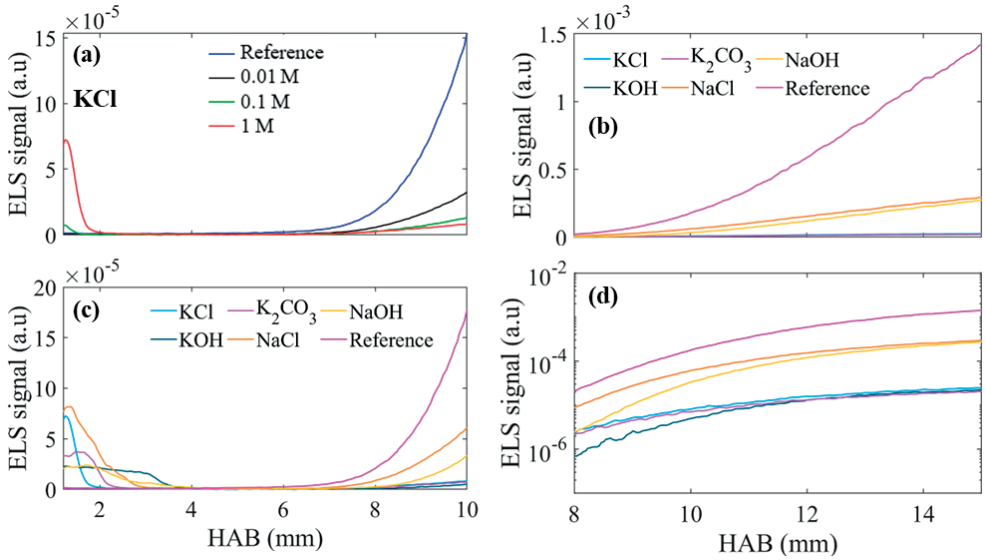

Figure 4.11: ELS signal profiles (incident and scattered light are vertically polarized) along the centreline of the burner for **(a)** the reference and different concentrations of KCl, and **(b)**, **(c)** & **(d)** for the 1 M case for all the salts. Note that the y-axis for (d) is in logarithmic scale.

Meanwhile, Fig. 4.11b and 4.11d (logarithmic y-axis) show very interesting trends in the signal profiles of various salts. On a first observation, one can notice that the ELS signal profiles of all cases with potassium salts overlap with each other at higher HABs ($\gtrsim$ 10 mm), irrespective of the type of salt. Similarly, the signal profiles of NaCl and NaOH addition also overlap with each other at higher HABs. This indicates that the ELS signals are negligibly influenced by the negative ions in these investigations, i.e. Cl^-, OH^- and CO_3^{2-}. Furthermore, in comparison with the reference case, potassium salts show a larger reduction in the ELS signal than the sodium salts. This is also congruent with a previous study, where the flames with the addition of KCl and NaCl were found to show lower ELS signals, and KCl cases subsequently showed smaller particle sizes [109, 110].

4.3.2 PAH-LIF Spectra

Spectral measurements of PAH-LIF signals were performed using both 266 nm and 532 nm excitation, termed as *LIF266 spectra* and *LIF532 spectra*, respectively. PAH-LIF spectra were acquired at the centre of the burner at different HABs for the reference case and 1 M cases of all the salts.

Excitation at 266 nm

Figure 4.12 shows the LIF266 spectra of the reference, and the 1 M cases of KCl and NaCl. The spectra show bimodal nature, which is in agreement with the literature [8, 81-84]. However, the peak in the UV region in the present study was found to be at ~ 350 nm instead of at 320 nm [81, 82, 84]. This could be due to the differences in flame conditions, such as temperatures, leading to a mixture of PAHs with different fluorescence properties. The PAH-LIF signal at longer wavelengths can be seen to increase with increase in HAB for all the cases. One can also see that the variation of LIF266 spectra with HAB matches with the height profiles presented in Figs 4.9 and 4.10 in the corresponding wavelength ranges. The addition of KCl and NaCl reduces the PAH-LIF signal at longer wavelengths ($\gtrsim$ 400 nm) without any significant change in the spectral shape. More detailed discussions on the LIF266 spectra can be found in Paper III.

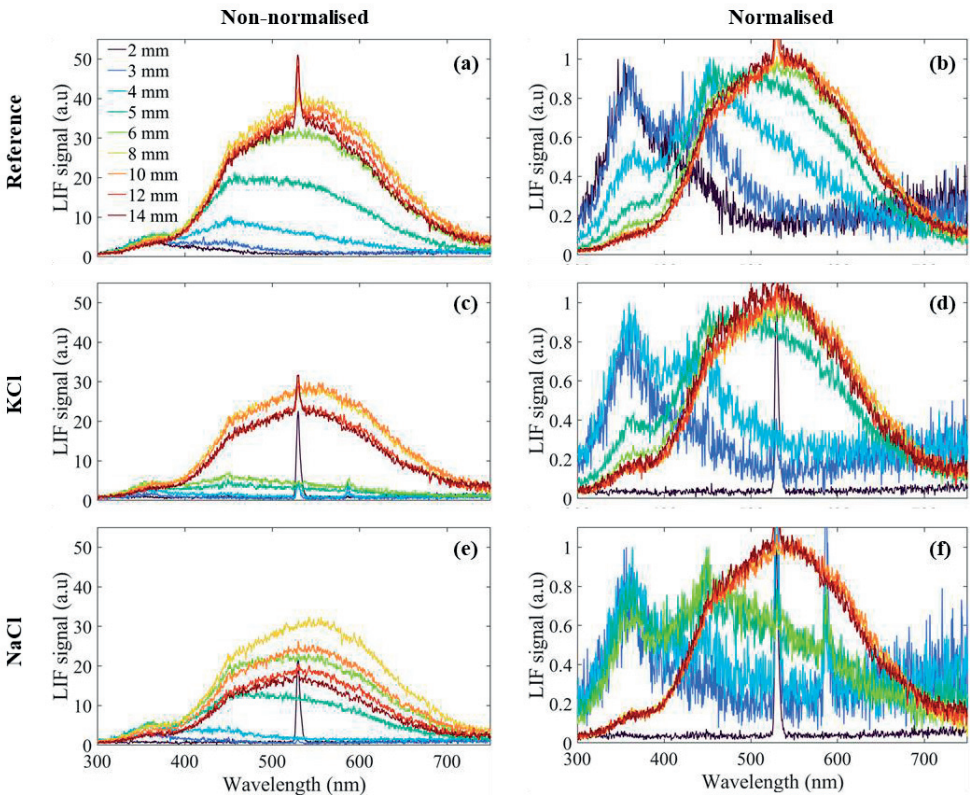

Figure 4.12: **(a, c & e)** Non-normalised LIF266 spectra of the reference, and 1 M cases of KCl and NaCl, respectively at different HABs. **(b, d & f)** Normalised spectra of the same.

Excitation at 532 nm

Figure 4.13 shows the normalised LIF532 profiles for the reference case, and 1 M cases of KCl and NaCl at various HABs. A first interesting observation is that for all the three cases, the spectral shape does not vary significantly vary with HAB. This might indicate that the composition of larger PAHs that can be excited by 532 nm is relatively constant with increasing HAB. One can also observe a drop in the LIF intensity profile at 532 nm due to the use of the notch filter positioned at 532 nm to block the strong scattering signal from soot.

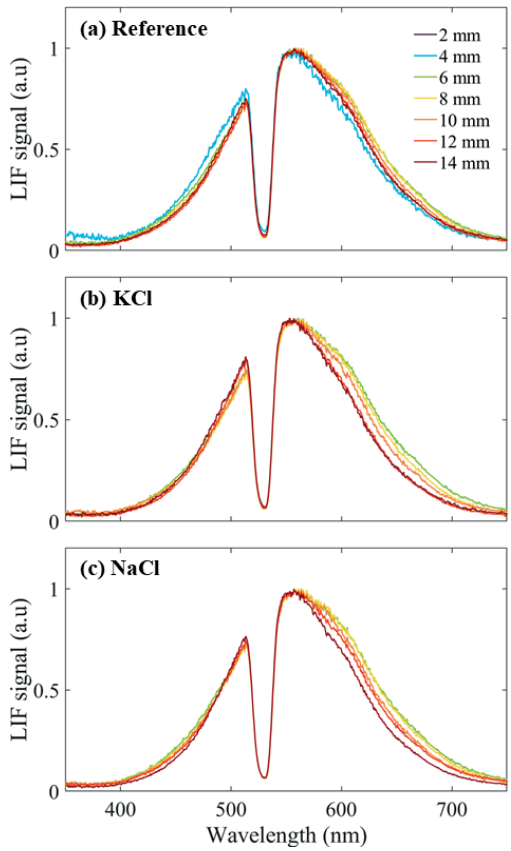

Figure 4.13: Normalised LIF532 spectra for **(a)** reference case, and 1 M cases of **(b)** KCl and **(c)** NaCl at different HABs.

The spectral measurements were found to corroborate well with the height profiles shown in Figs 4.9 and 4.10 in the corresponding wavelength ranges. In the literature, KCl and other salt additives have shown to reduce the soot concentration while

significantly increasing the particle number density (and reducing soot particle size) [112]. Like coalescence as a soot particle growth process, evidence of coalescence of smaller PAHs to form larger ones have been found experimentally [113] and has also been modelled in the study by Wang et al. [18]. This might indicate the dissociated sodium and especially potassium salts ionize the smaller PAHs and hinder their progress to form heavier PAHs [114].

This study on the influence of alkali metal salts on PAH and soot formation can be very useful for improving soot formation mechanisms in biofuel combustion. LII measurements have also been done for all these salts, and the analysis of the LII data is currently ongoing. It would also be valuable to develop a detailed chemical kinetic study on the influence of these alkali metal salts on soot formation.

4.4 Soot Diagnostics in the Optical Engine

Laser-diagnostic techniques have been successfully applied in studying soot formation in laboratory-scale burners, presented in Papers I – III. Paper IV and V presented the investigations applying optical diagnostic techniques such as high-speed imaging of Mie scattering and natural luminosity (NL), and extinction and 2D LII in a Volvo light-duty optical diesel engine. Spray and soot formation as well as late cycle soot oxidation were investigated, and especially the behaviour due to two factors; the age of injector and the use of a fuel additive.

The first factor was the aging of injectors, where a new and an aged injector (with over 100,000 km on-field usage) were used. Aging of injectors have been found to adversely affect the combustion process [36, 46, 115-118]. Also, they have shown to influence the fuel injection rates [36, 117, 119], spray penetration [118], flow field [115], and result in higher exhaust emissions [117], such as hydrocarbon [118] and soot emissions [36].

The second factor was the presence of the fuel additive tripropylene glycol monomethyl ether (TPGME) in late-cycle soot oxidation. TPGME has been shown to reduce engine out soot emissions [120], and the in-cylinder spatially integrated natural luminosity (NL, which approximately indicates the total soot formed) signal compared to the reference fuels [98]. Several investigations using line-of-sight averaged optical techniques have also indicated that TPGME can be good candidate for a fuel additive that reduces soot emissions [95-97, 121].

There were a few novelties in the investigations reported in Papers IV and V. The measurements were performed in an optical diesel engine equipped with a quartz piston with the exact geometry of a production engine. Mie scattering and NL measurements were applied at high-speed detection to study the spray and soot formation, and 2D LII and extinction were used to semi-quantitatively evaluate soot volume fractions and soot oxidation rates. Measurements were also performed at two load conditions, termed as low load and mid load cases.

In the following text, only some highlights of the results in Papers IV and V are presented in addition to some other interesting aspects of these investigations.

4.4.1 Aging of injectors

From a previous investigation in a metal engine, it was found that the aged injectors showed higher fuel injection rates, resulting in a ~ 22 % and ~ 9 % increase in load for the low load and mid load cases respectively [36]. X-ray tomography measurement on the injectors revealed that there were no distinct differences between the geometries of the new and aged injectors (Paper IV). High-speed imaging of Mie scattering signals from the diesel sprays were used to study spray formation. Figure 4.14 shows the temporal behaviour of the total Mie scattering signal for one of the well-illuminated sprays for the new and aged injectors along with the injection signal for the low load (Fig. 4.14a) and mid load (Fig. 4.14b) conditions. The injection process consists of two pilot injections, one main injection and one post injection. It can be seen that at low load, the aged injector injects more fuel for all injections (two pilot, one main and one post injections). The same is true for the mid load case except the maximum signal intensity of the main injection remains similar for both the injectors. However, from the longer duration of the scattering signal for the aged injector, it can be suggested that the needle has a delay in closing for the aged injector. The Mie scattering measurements corroborate well with the metal engine measurements [36] regarding the increase in load for the aged injector for the same injection conditions. The aged injector was also found to consistently produce larger amounts of fuel dribbles towards the end of injections.

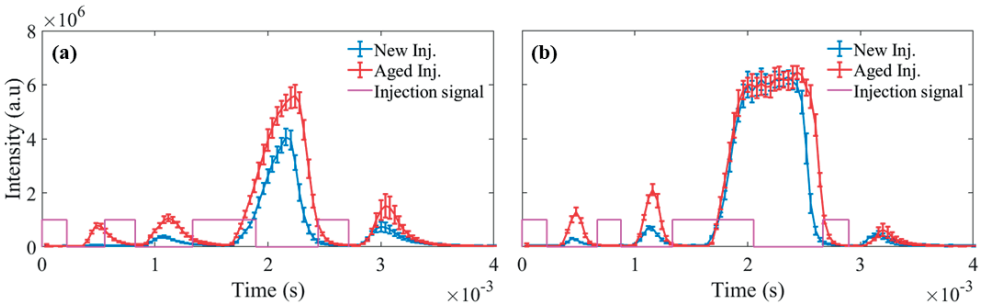

Figure 4.14: Total Mie scattering intensity of a well illuminated spray for the new and aged injectors at **(a)** low load and **(b)** mid load conditions. The corresponding injection signals are also shown.

High-speed imaging measurements of natural luminosity (NL) showed higher signals for the aged injector throughout the cycle for the low load case, primarily due to the large increase in load. However, for the high load case, the peak NL signal corresponding to the main injection at ~ 22 ° crank angle after top dead centre (°CA aTDC) was higher for the new injector, which dropped below the aged injector case at ~ 27 °CA aTDC.

Extinction measurements along with 2D LII were used to semi-quantitatively evaluate 2D soot volume fraction (f_v) distributions in the late cycle ($\geq$ 25°CA aTDC). Figure 4.15a and 4.15b show the variation of $K_{ext}L$ (represents line-integrated f_v) with CAD at low and mid load conditions respectively. Meanwhile, Fig. 4.15c and 4.15d show the variation of mean f_v with CAD at both loads. This data was later used to calculate semi-quantitative soot oxidation rates, represented using half-lives. It was found that the aged injector produced higher f_v compared to the new injector at both loads, potentially due to the higher fuel injection rates in the aged injector. Aged injector also showed higher soot oxidation rates compared to the new injector at low load conditions, while showing similar values at mid load conditions. The faster soot oxidation at low load might be due to the larger percentage increase in load for the aged injector compared to the mid load conditions. This might cause in a more predominant late cycle mixing driven by the increased momentum transfer from the spray, subsequently increasing the late cycle soot oxidation rate.

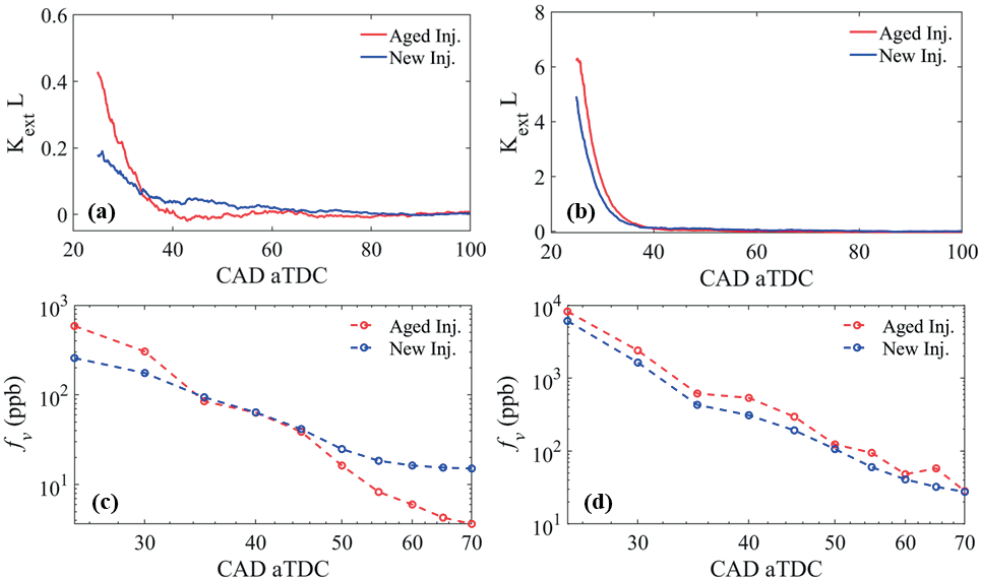

Figure 4.15: $K_{ext}L$ derived from extinction measurements vs crank angle degree after top dead center (CAD aTDC) for **(a)** low load and **(b)** mid load conditions for the aged and new injectors; Mean f_v evaluated from LII measurements along the region of the laser sheet over the piston top vs CAD aTDC at **(c)** low and **(d)** mid load conditions for the same cases.

4.4.2 Issues of LII measurements in the Optical Engine

Soot Deposit Formation

As there is a large amount of soot formed inside the combustion chamber during the cycle, soot deposit formation on the surfaces of the optical piston and windows are frequent. These soot deposits absorb the NL and LII signals on its way to the detector. This will create uncertainties in the results. To mitigate these, the optical piston and windows were cleaned regularly using ethanol. The rate of deposit formation on windows was much slower compared to the deposit formation on the piston.

Figure 4.16 shows mean natural luminosity images, or background luminosity images acquired at 30°CA aTDC for the aged injector at mid load. Figure 4.16a and 4.16b correspond to the mean of the first 5 and last 5 background luminosity single-shot images in between the cleaning of the piston and windows. It can be seen that the signal from inside the piston bowl has dropped. This lower intensity is primarily due to the formation of deposits on the piston surface, although there are cycle-to-cycle variations and a low number of images are included in the mean image.

Frequent cleaning after ~ 15 fired cycles were chosen in order to obtain sufficiently good statistical data while keeping the formation of deposits on an acceptably low level.

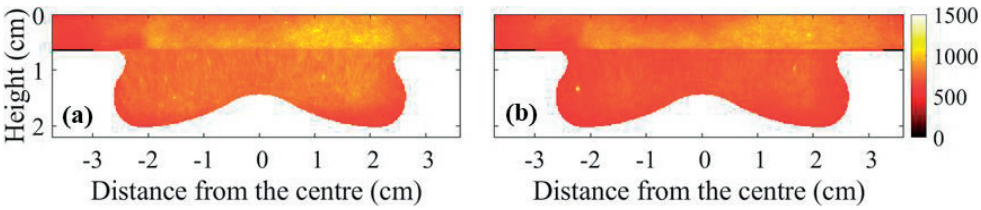

Figure 4.16: Mean natural luminosity images (background image of LII) acquired using the ICCD camera through the side windows using a gate width of 20 ns. **(a)** Mean of the first 5 single-shot images after the cleaning of the piston. **(b)** Mean of the last 5 single-shot images before the cleaning. The colour-bar represents signal intensity (a.u).

Semi-Simultaneous Background Subtraction

Background luminosity images were acquired ~ 2.2 µs before the acquisition of the LII signal on a single-shot basis. This procedure improves the accuracy of the LII measurements as the background luminosity distribution varies from cycle-to-cycle due to the turbulent nature of the flame and due to the build-up of soot deposits. Figure 4.17 can be used to show some insights into this issue. Figure 4.17a and 4.17b are respectively, single-shot and mean background luminosity images at 30°CA aTDC for the aged injector at mid load. The mean image in Fig. 4.17b is obtained by averaging 60 single-shot images. Although the mean image seems to represent the distribution well, there are differences between the images, for example, the maximum signal intensities. Figure 4.17c shows the mean LII signal image (of 30 single-shot images) where background subtraction was performed on a shot-to-shot basis. A mean background luminosity image obtained from a different set of 30 single-shot images was subtracted from the mean of the same 30 single-shot LII images used in Fig. 4.17c, and the resulting LII image is shown in Fig. 4.17d. When comparing these two figures (c and d) a first conclusion is that the main features can be seen in both images. Figure 4.17e shows the difference between Fig. 4.17c and 4.17d, and it can be seen that this signal intensity is not negligible. The differences could be due to shot-to-shot variation in flame shapes and due to deposits, which will get carried forward in the calibration to f_v and in the evaluation of soot oxidation rates. This underlines the use of semi-simultaneous background subtraction for LII measurements in turbulent flames.

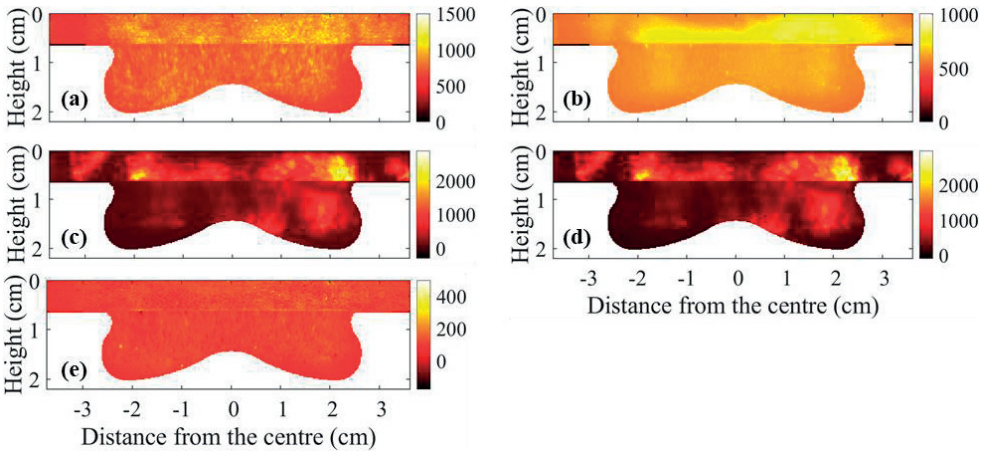

Figure 4.17: **(a)** Single-shot background luminosity image at 30°CA aTDC for the aged injector at mid load. **(b)** mean background luminosity image for the same case. **(c)** Mean LII image obtained after performing background subtraction on a shot-to-shot basis. **(d)** Mean LII image obtained after subtracting the mean background luminosity image from a different set of signal images from the LII images used in (c). **(e)** Difference between (c) and (d). The colour-bars represent signal intensity (a.u).

5 Summary, Conclusions & Outlook

In this chapter, a summary and the most relevant conclusions of the conducted work is presented. A discussion on the implications of this work along with the future possibilities is also included.

5.1 Summary and Conclusions

In the works involved in this thesis, multiple diagnostic techniques were used to investigate soot formation. Laser-induced incandescence (LII), extinction and laser-induced fluorescence of polycyclic aromatic hydrocarbons (PAH-LIF) have provided important information about soot characteristics in the works in Papers I-V. These techniques have been applied on small-scale laboratory burners (McKenna and Perkin-Elmer burners) to practical combustion devices (diesel engines). Additionally, the heat-and-mass-transfer-based LII model was used to compliment the measurements through improved understanding of the LII signal behaviour.

In the work presented in Paper I, the effects of focusing optics on quantitative 2D LII measurements were investigated. 2D LII measurements were performed using a cylindrical lens with a focal length of 500 mm on flat premixed ethylene air flames (ϕ = 2.1) stabilized on a McKenna burner. The bias in the 2D LII signal resulting from the variation of laser sheet width in the imaging region along the propagation direction of the laser was found to be significant (several tens of percent). Numerical calculations using the LII model were used to estimate LII signals across 2D LII images for various combinations of focal lengths (FL), image lengths (IL), gate widths and laser fluences. The ratio between FL and IL termed as the FL/IL ratio, was introduced as a valuable parameter to estimate the LII signal response to soot volume fraction over the whole image length. It was found that high FL/IL ratios minimize the bias, which suggests using a focusing lens with a very long focal length. After choosing a long focal length lens, this bias can be further minimized

using optimal choices of detection gate width and laser fluence for the actual experimental situation and based on supporting LII model calculations.

In Paper II, work is presented where the diagnostic techniques LII, extinction, and PAH-LIF were used to study soot maturity in methane-air diffusion flames at elevated pressures up to 0.5 MPa. It is well known that the value of the soot absorption function ($E(m)$) increases during the soot maturation process. The assumption of constant $E(m)$ values for soot while performing spectral soot emission (SSE) and line-of-sight attenuation (LOSA) measurements, which are commonly used for flames in elevated pressures, has been reported as a prime source in creating measurement uncertainties. The LII fluence curves generated from the measurements at various locations in the flames were used in a fitting procedure using the numerical LII model, in which $E(m)$ was the fitting variable. It was found that the soot $E(m)$ values at the maximum soot volume fraction (f_v) location along the centreline of the burner increases significantly (~ 66 % increase between 0.1 – 0.5 MPa) with increase in pressure. Another result was that soot $E(m)$ values increased along the centreline with height above burner during the soot formation process. The pressure exponent x in the expression $f_v \sim P^x$ evaluated using the assumption of constant $E(m)$ of 0.27 and the $E(m)$ values estimated in this study did not show considerable differences given the significant variation in $E(m)$ values. This study emphasizes the problems with the use of constant $E(m)$ for all the soot under study for the evaluation of temperature and f_v using SSE + LOSA while investigating sooting high pressure flames.

PAH and soot formation processes relevant to biomass combustion were investigated primarily using PAH-LIF and elastic light scattering (ELS) (Paper III). It is well-known that biomass contains trace metals such as potassium and sodium, which motivates improved understanding of the influence of these metals on the PAH and soot formation processes. Water solutions of several salts of potassium and sodium at various concentrations were aspirated into premixed ethylene-air flames (ϕ = 2.6) stabilized on a Perkin-Elmer burner. From the PAH-LIF measurements, it was found that the addition of salts had negligible influence in the formation of smaller PAHs (2 – 3 rings). However, there was a decrease in the concentration of larger PAHs throughout the flame region monitored in the lower LIF signal. It was also found that the fluorescence and scattering signal response for all the potassium salt (KCl, KOH and K_2CO_3) additives were similar to each other irrespective of the negative ions. The corresponding signal responses for the two sodium salts (NaCl and NaOH) additives were similar to each other, and differed

from the potassium salt additives. This indicates that it is primarily the metal ion that influences the PAH and soot formation process. The results from this study can be useful for developing chemical kinetic models on the influence of alkali metal salts on soot formation.

Soot formation and oxidation studies were also performed in an optical diesel engine (Papers IV and V). This work composed of two investigations. Firstly, to study the effects of injector aging on spray and soot formation and late cycle soot oxidation, as previous studies have shown that aging of injectors adversely affect the combustion and pollutant emissions in diesel engines. The second investigation was to study the effects of the oxygenated fuel additive tripropylene glycol monomethyl ether (TPGME) on soot formation and late cycle soot oxidation, as this additive was found to lower soot emissions in some previous studies. Measurements were performed at two load conditions termed as low and mid load conditions. The spray and soot formation were visualized using high-speed imaging measurements of Mie scattering and natural luminosity, whereas semi-quantitative estimation of f_v and soot oxidation rates late in the cycle were estimated using 2D LII and extinction measurements. It was found that the aged injector has a higher fuel flow rate compared to the new injector, especially at the low load conditions. The increase in loads estimated from measurements in a metal engine using the same pair of injectors showed a ~ 22 % and ~ 9 % increase in load at low and mid load conditions respectively, compared to the new injector. The aged injector also produced higher amount of soot at both loads and showed faster late cycle soot oxidation rates at low load. Additionally, fuel with the TPGME additive showed lower soot concentrations at both loads and faster soot oxidation rates at mid load.

5.2 Outlook

The most important findings relevant to the LII community are the effects of laser focusing optics on 2D LII measurements, presented in Paper I. It was found that the effects due to the varying laser sheet width across the imaging region leads to significant bias in the 2D LII signal distribution, which might carry forward to f_v distributions upon calibration using extinction measurements. This result will be helpful in choosing focusing lens with appropriately long focal lengths for performing quantitative 2D LII measurements, especially in large flames. If all the properties in the flame are known, the method used in this study can potentially be used to correct for the bias caused due to the focusing optics. This thesis also has

other contributions to the diagnostic community in general. For example, the strategy for removal of PAH-LIF signal interference from the LII signal while using the laser wavelength 532 nm (Paper II).

The main contribution of this thesis towards the combustion community, especially the biomass combustion community, are the results reported in section 4.3 and in Paper III. As biomass contains traces of alkali metals, such as sodium and potassium, information on their influence on PAH and soot formation is vital in improving the current biomass combustion systems. The finding that the addition of salts does not influence the concentration of small PAHs while decreasing the concentration of larger PAHs is especially interesting. The implication that the negative ions in the salt molecule have negligible effect in PAH and soot formation is also of great interest. Additionally, there were no significant changes in the shapes of the PAH-LIF spectra upon the addition of potassium and sodium salts. It would also be interesting to try out probe sampling from the flame and perform much more selective diagnostics such as gas chromatography, molecular beam mass spectrometry, atomic force microscopy, etc. Collaborations with soot modellers on developing chemical kinetic models for spreading light on the influence of alkali metal salts on PAH and soot formation is planned to be done in the future. Additionally, more detailed analysis of the ELS data from the measurement campaign will be performed. Moreover, a detailed analysis of LII data acquired for all the cases with salt additives will also be done in the future.

Acknowledgements

There are so many people whom I would like to thank for being part of this journey of mine. Kindly forgive me if I have missed to mention someone.

I would like to start by acknowledging my main supervisor, Per-Erik Bengtsson for giving me this opportunity to pursue my PhD studies at the Division of Combustion Physics. I feel lucky to have you as my supervisor as you have been a role model in terms of character as well as scientific aptitude. I would also like to thank my co-supervisor Öivind Andersson who have been immense in guiding me through the engine campaign. Your quick wittedness and the ability to give feedback has always amazed me.

I would like to thank all the present and former members of the *Soot group* for being so kind and supportive to me. Thanks to Johan Simonsson for helping me out as a beginner, Sandra Török for being the nicest person ever, Thi Kim Cuong Le for inspiring me with your hard work, Saga Bergqvist for teaching me fun Swedish sayings and Jian Wu for the great time during the LII workshop 2018.

I would also like to acknowledge my IPPAD family for giving an amazing experience in the first 3 years of my PhD life, especially Prof. Manolis Gavaises and Nikolaos Chatziarsenis for coordinating the project, and Prof. Stefan Will for hosting me at LTT Erlangen. I would like to thank Xinda Zhu for always being the coolest lab-partner even during the never-ending process of cleaning the soot. I would like to thank Natascia Palazzo for being the best host during my time in Erlangen. I would also like to thank Vikrant Mahesh and Jawad Rezaei, and other colleagues at LTT, Philip Bauer, Dr. Lars Zigan, Dr. Franz Huber and Dr. Matthias Kögl for all the help. I would also like to thank Mijo Tvrdojevich for the 'Ambassad' talks. All the others in the IPPAD program are also thankfully acknowledged.

I am grateful to all the colleagues at Combustion Physics in making my PhD studies so enjoyable. I would like to thank Marcus Alden for being the charismatic leader of the division for so long, Minna Ramkull for being the kind and helpful person you are, Cecilia Bille for patiently clarifying my doubts on economy matters

countless number of times, Igor Buzuk for the fun conversations and all the help related to the IT, and Robert Collin for informing me about the safety issues.

I would also like to thank other colleagues at the division, Mattias Richter for the laser diagnostics course and letting me borrow countless number of components from your reservoir of a lab, Christian Brackmann for always lending a helping hand in the lab, Zhongshan Li, Sven-Inge Möller, Frederik Ossler and Edouard Berrocal for the nice conversations and help. I would also like to thank Yogeshwar Nath Mishra for all the help in starting my life in Sweden, and Arman Ahamed Subash for all the help and for our countless lunches at Govindas. I would like to thank Dina Hot on being the most caring person, Meena Raveesh on being able to crack Malayalam chalis at work, Christoffer Pichler for inviting me to your activities when I started here, and Gianluca Capriolo, Torsten Methling, Pengji Ding, Jim Larsson and Karolina Dorozynska for all the fun conversations and help. I want to thank Wubin Weng, Jinlong Gao, Zhenkan Wang, Maria Ruchkina and Alexios Matamis for your immense help during my measurement campaigns. I would also like to thank Haisol Kim, Joakim Jönsson, Yupan Bao, Ali Hosseinia, Qingshuang Fan, Henrik Feuk, Sebastian Nilsson, Adrian Roth, Shen Li, Lisa Rämish, David Sanned, Panagiota Stamatoglou, Meng Li, Ruike Bi and the others for all the help and for being the friendly faces at work.

I was also able to make some good friends during these past few years who have helped me greatly. I would like to thank Vedangi Pathak and Ludovica Luise for being my first friends in Sweden, and Christian Binder on being a good friend to plan a road trip with, to places where wild horses run alongside the car. I would like to thank my corridor mates, especially Robin Kratz and Jennie Karlsson for all the conversations and movie nights at Delphi 55D. I want to thank Gösta Petersen, and all the members of Lund International Students' Choir in filling my time in Lund with music. I would like to thank Marco Lubrano Lavadera on being a great friend since the past few years, to have discussions on football, life, and everything else. I would also like to thank Saeed Derafshzan for being another great friend, and wish to thank you and Sara for hosting countless football watch-parties. Finally, I wish to thank Xin Liu for being my amazing office-mate and friend, for all the long conversations we had, and the positive cheerfulness you radiate.

I would like to acknowledge the organizations and foundations that made this research possible; EU Horizon 2020 research and innovation program under the Marie-Sklodowska-Curie grant agreement No. 675528 (IPPAD project), and the Energimyndigheten through the Swedish Gasification Centre (34721-3).

Last but not the least, I would like to thank my family from the bottom of my heart. You have always encouraged my endeavours, apart from the few months after the cricket world cup in 2003, when I wanted to be cricketer. I would also like to thank Anu for being the happy soul as you are, and being patient with me during the time of thesis writing. I am also thankful to my friends Irfan Habeeb, Jadhav Dattatreya, Arjun BJ and Nigam Krishna for all the help and support.

Bibliography

1. O. Edenhofer, R. Pichs-Madruga, Y. Sokona, J. Minx, E. Farahani, K. Susanne, K. Seyboth, A. Adler, I. Baum, S. Brunner, AR5 climate change 2014: Mitigation of climate change, IPCC, New York, USA, Tech. Rep (2014).
2. T.C. Bond, S.J. Doherty, D.W. Fahey, P.M. Forster, T. Berntsen, B.J. DeAngelo, M.G. Flanner, S. Ghan, B. Kärcher, D. Koch, Bounding the role of black carbon in the climate system: A scientific assessment, Journal of geophysical research: Atmospheres 118 (11) (2013) 5380-552.
3. C.K.B. Ferrari, E. Luzia França, A.C. Honorio-Franca, Nitric oxide, health and disease, Journal of Applied Biomedicine 7 (4) (2009) 163-73.
4. R. Prasad, V.R. Bella, A review on diesel soot emission, its effect and control, Bulletin of Chemical Reaction Engineering & Catalysis 5 (2) (2010) 69.
5. I.M. Kennedy, The health effects of combustion-generated aerosols, Proc. Combust. Inst. 31 (2) (2007) 2757-70.
6. E.J. Highwood, R.P. Kinnersley, When smoke gets in our eyes: The multiple impacts of atmospheric black carbon on climate, air quality and health, Environment international 32 (4) (2006) 560-6.
7. H. Michelsen, Probing soot formation, chemical and physical evolution, and oxidation: A review of in situ diagnostic techniques and needs, Proc. Combust. Inst. 36 (1) (2017) 717-35.
8. S. Bejaoui, X. Mercier, P. Desgroux, E. Therssen, Laser induced fluorescence spectroscopy of aromatic species produced in atmospheric sooting flames using UV and visible excitation wavelengths, Combust. Flame 161 (10) (2014) 2479-91.
9. K.-H. Kim, S.A. Jahan, E. Kabir, R.J. Brown, A review of airborne polycyclic aromatic hydrocarbons (PAHs) and their human health effects, Environment international 60 (2013) 71-80.
10. A. Khan, W. de Jong, P. Jansens, H. Spliethoff, Biomass combustion in fluidized bed boilers: Potential problems and remedies, Fuel processing technology 90 (1) (2009) 21-50.
11. R. Saidur, E. Abdelaziz, A. Demirbas, M. Hossain, S. Mekhilef, A review on biomass as a fuel for boilers, Renewable and sustainable energy reviews 15 (5) (2011) 2262-89.
12. R. Van den Broek, A. Faaij, A. van Wijk, Biomass combustion for power generation, Biomass and Bioenergy 11 (4) (1996) 271-81.

13. N. Abas, A. Kalair, N. Khan, Review of fossil fuels and future energy technologies, Futures 69 (2015) 31-49.
14. S. Shafiee, E. Topal, An econometrics view of worldwide fossil fuel consumption and the role of US, Energy policy 36 (2) (2008) 775-86.
15. H. Bladh, P.-E. Bengtsson, Characteristics of laser-induced incandescence from soot in studies of a time-dependent heat-and mass-transfer model, Appl. Phys. B 78 (2) (2004) 241-8.
16. I. Glassman. Combustion. 4th Edition ed: Academic Press, San Diego; 2008.
17. H. Michelsen, C. Schulz, G. Smallwood, S. Will, Laser-induced incandescence: Particulate diagnostics for combustion, atmospheric, and industrial applications, Prog. Energy Combust. Sci. 51 (2015) 2-48.
18. H. Wang, Formation of nascent soot and other condensed-phase materials in flames, Proc. Combust. Inst. 33 (1) (2011) 41-67.
19. M. Frenklach, Reaction mechanism of soot formation in flames, Physical chemistry chemical Physics 4 (11) (2002) 2028-37.
20. H.A. Michelsen, Effects of maturity and temperature on soot density and specific heat, Proc. Combust. Inst. (2020).
21. T.C. Bond, R.W. Bergstrom, Light absorption by carbonaceous particles: An investigative review, Aerosol Sci. Technol. 40 (1) (2006) 27-67.
22. F. Liu, J. Yon, A. Fuentes, P. Lobo, G.J. Smallwood, J.C. Corbin, Review of recent literature on the light absorption properties of black carbon: Refractive index, mass absorption cross section, and absorption function, Aerosol Sci. Technol. 54 (1) (2020) 33-51.
23. A.R. Coderre, K.A. Thomson, D.R. Snelling, M.R. Johnson, Spectrally resolved light absorption properties of cooled soot from a methane flame, Appl. Phys. B 104 (1) (2011) 175-88.
24. N.-E. Olofsson, J. Simonsson, S. Török, H. Bladh, P.-E. Bengtsson, Evolution of properties for aging soot in premixed flat flames studied by laser-induced incandescence and elastic light scattering, Appl. Phys. B 119 (4) (2015) 669-83.
25. J.B. Heywood. Internal Combustion Engine Fundamentals: McGraw-Hill; 1988.
26. J.E. Dec, A conceptual model of DL diesel combustion based on laser-sheet imaging, SAE transactions (1997) 1319-48.
27. C. Schulz, B.F. Kock, M. Hofmann, H. Michelsen, S. Will, B. Bougie, R. Suntz, G. Smallwood, Laser-induced incandescence: recent trends and current questions, Appl. Phys. B 83 (3) (2006) 333.
28. J. Simonsson. Laser Diagnostics for Soot in Small-Scale and Practical Systems: Lund University; 2018.
29. F. Migliorini, S. De Iuliis, F. Cignoli, G. Zizak, How “flat” is the rich premixed flame produced by your McKenna burner?, Combust. Flame 153 (3) (2008) 384-93.
30. N.-E. Olofsson, H. Bladh, A. Bohlin, J. Johnsson, P.-E. Bengtsson, Are sooting premixed porous-plug burner flames one-dimensional? A laser-based

experimental investigation, Combustion science and technology 185 (2) (2013) 293-309.
31. J. Simonsson, N.-E. Olofsson, S. Török, P.-E. Bengtsson, H. Bladh, Wavelength dependence of extinction in sooting flat premixed flames in the visible and near-infrared regimes, Appl. Phys. B 119 (4) (2015) 657-67.
32. S. Hu, J. Gao, C. Gong, Y. Zhou, d.X. Bai, Z. Li, M. Alden, Assessment of uncertainties of laminar flame speed of premixed flames as determined using a Bunsen burner at varying pressures, Applied energy 227 (2018) 149-58.
33. P.H. Joo, J. Gao, Z. Li, M. Aldén, Experimental apparatus with full optical access for combustion experiments with laminar flames from a single circular nozzle at elevated pressures, Rev. Sci. Instruments 86 (3) (2015) 035115.
34. M. Mannazhi, S. Török, J. Gao, P.-E. Bengtsson, Soot maturity studies in methane-air diffusion flames at elevated pressures using laser-induced incandescence, Proc. Combust. Inst. (2020).
35. H. Bladh. On the use of laser-induced incandescence for soot diagnostics: from theoretical aspects to applications in engines: Lund University; 2007.
36. X. Zhu, Ö. Andersson, Performance of new and aged injectors with and without fuel additives in a light duty diesel engine, Transportation Engineering (2020) 100007.
37. C.L. Hagen, S.T. Sanders, Investigation of multi-species (H2O2 and H2O) sensing and thermometry in an HCCI engine by wavelength-agile absorption spectroscopy, Measurement Science and Technology 18 (7) (2007) 1992.
38. J. Langridge, T. Laurila, R. Watt, R. Jones, C. Kaminski, J. Hult, Cavity enhanced absorption spectroscopy of multiple trace gas species using a supercontinuum radiation source, Optics Express 16 (14) (2008) 10178-88.
39. R. Mihalcea, M. Webber, D. Baer, R. Hanson, G. Feller, W. Chapman, Diode-laser absorption measurements of CO2, H2O, N2O, and NH3 near 2.0 μm, Appl. Phys. B 67 (3) (1998) 283-8.
40. A. Thompson, H. Northern, B. Williams, M. Hamilton, P. Ewart, Simultaneous detection of CO2 and CO in engine exhaust using multi-mode absorption spectroscopy, MUMAS, Sensors and Actuators B: Chemical 198 (2014) 309-15.
41. C.F. Bohren, D.R. Huffman: Absorption and Scattering of Light by Small Particles, WileyVCH. Weinheim; 1998.
42. F. Migliorini, K. Thomson, G. Smallwood, Investigation of optical properties of aging soot, Appl. Phys. B 104 (2) (2011) 273-83.
43. S. Krishnan, K.-C. Lin, G. Faeth, Extinction and scattering properties of soot emitted from buoyant turbulent diffusion flames, J. Heat Transfer 123 (2) (2001) 331-9.
44. J. Simonsson, A. Gunnarsson, M.N. Mannazhi, D. Bäckström, K. Andersson, P.-E. Bengtsson, In-situ soot characterization of propane flames and influence of additives in a 100 kW oxy-fuel furnace using two-dimensional laser-induced incandescence, Proc. Combust. Inst. 37 (1) (2019) 833-40.
45. D. Bäckström, A. Gunnarsson, D. Gall, X. Pei, R. Johansson, K. Andersson, R.K. Pathak, J.B. Pettersson, Measurement of the size distribution, volume

fraction and optical properties of soot in an 80 kW propane flame, Combust. Flame 186 (2017) 325-34.
46. X. Pei. A Soot Transformation Study: Interactions Between Soot, Sulfuric Acid and Secondary Organic Aerosol (SOA)2018.
47. H. Bladh, J. Johnsson, P.-E. Bengtsson, On the dependence of the laser-induced incandescence (LII) signal on soot volume fraction for variations in particle size, Appl. Phys. B 90 (1) (2008) 109-25.
48. H. Bladh, J. Johnsson, P.-E. Bengtsson, Influence of spatial laser energy distribution on evaluated soot particle sizes using two-colour laser-induced incandescence in a flat premixed ethylene/air flame, Appl. Phys. B 96 (4) (2009) 645-56.
49. H. Bladh, J. Johnsson, N.-E. Olofsson, A. Bohlin, P.-E. Bengtsson, Optical soot characterization using two-color laser-induced incandescence (2C-LII) in the soot growth region of a premixed flat flame, Proc. Combust. Inst. 33 (1) (2011) 641-8.
50. H. Bladh, J. Johnsson, J. Rissler, H. Abdulhamid, N.-E. Olofsson, M. Sanati, J. Pagels, P.-E. Bengtsson, Influence of soot particle aggregation on time-resolved laser-induced incandescence signals, Appl. Phys. B 104 (2) (2011) 331-41.
51. L.S. Ruzer, N.H. Harley. Aerosols handbook: measurement, dosimetry, and health effects: CRC press; 2012.
52. F. Liu, M. Yang, F.A. Hill, D.R. Snelling, G.J. Smallwood, Influence of polydisperse distributions of both primary particle and aggregate size on soot temperature in low-fluence LII, Appl. Phys. B 83 (3) (2006) 383-95.
53. B. McCoy, C. Cha, Transport phenomena in the rarefied gas transition regime, Chemical Engineering Science 29 (2) (1974) 381-8.
54. N. Fuchs, On the stationary charge distribution on aerosol particles in a bipolar ionic atmosphere, Pure Appl. Geophys. 56 (1) (1963) 185-93.
55. A. Filippov, D. Rosner, Energy transfer between an aerosol particle and gas at high temperature ratios in the Knudsen transition regime, International journal of heat and mass transfer 43 (1) (2000) 127-38.
56. F. Liu, K. Daun, D.R. Snelling, G.J. Smallwood, Heat conduction from a spherical nano-particle: status of modeling heat conduction in laser-induced incandescence, Appl. Phys. B 83 (3) (2006) 355-82.
57. H.A. Michelsen, Understanding and predicting the temporal response of laser-induced incandescence from carbonaceous particles, J. Chem. Phys. 118 (15) (2003) 7012-45.
58. C.J. Dasch, Continuous-wave probe laser investigation of laser vaporization of small soot particles in a flame, Appl. Opt. 23 (13) (1984) 2209-15.
59. K.A. Thomson, K.P. Geigle, M. Köhler, G.J. Smallwood, D.R. Snelling, Optical properties of pulsed laser heated soot, Appl. Phys. B 104 (2) (2011) 307-19.
60. G.D. Yoder, P.K. Diwakar, D.W. Hahn, Assessment of soot particle vaporization effects during laser-induced incandescence with time-resolved light scattering, Appl. Opt. 44 (20) (2005) 4211-9.

61. D.R. Snelling, F. Liu, G.J. Smallwood, Ö.L. Gülder, editors. Evaluation of the nanoscale heat and mass transfer model of LII: prediction of the excitation intensity. Proceedings of the 34th National Heat Transfer Conference; 2000; Pittsburg, PA.
62. J. Johnsson. Laser-induced incandescence for soot diagnostics: theoretical investigation and experimental development: Lund University; 2012.
63. S.T. Manu Mannazhi, Jinlong Gao, Per-Erik Bengtsson, Soot maturity studies in methane-air diffusion flames at elevated pressures using laser-induced incandescence, Proc. Combust. Inst. 38 (2021).
64. X. López-Yglesias, P.E. Schrader, H.A. Michelsen, Soot maturity and absorption cross sections, J. Aerosol Sci. 75 (2014) 43-64.
65. K. Johansson, F. El Gabaly, P. Schrader, M. Campbell, H. Michelsen, Evolution of maturity levels of the particle surface and bulk during soot growth and oxidation in a flame, Aerosol Sci. Technol. 51 (12) (2017) 1333-44.
66. Z. Sun, Z. Alwahabi, D. Gu, S. Mahmoud, G. Nathan, B. Dally, Planar laser-induced incandescence of turbulent sooting flames: the influence of beam steering and signal trapping, Appl. Phys. B 119 (4) (2015) 731-43.
67. C.R. Shaddix, T.C. Williams, The effect of oxygen enrichment on soot formation and thermal radiation in turbulent, non-premixed methane flames, Proc. Combust. Inst. 36 (3) (2017) 4051-9.
68. L.M. Pickett, D.L. Siebers, Fuel effects on soot processes of fuel jets at DI diesel conditions, SAE transactions (2003) 2044-66.
69. E.A. Griffin, M. Christensen, Ö.L. Gülder, Effect of ethanol addition on soot formation in laminar methane diffusion flames at pressures above atmospheric, Combust. Flame 193 (2018) 306-12.
70. H.I. Joo, Ö.L. Gülder, Soot formation and temperature structure in small methane–oxygen diffusion flames at subcritical and supercritical pressures, Combust. Flame 157 (6) (2010) 1194-201.
71. P.M. Mandatori, Ö.L. Gülder, Soot formation in laminar ethane diffusion flames at pressures from 0.2 to 3.3 MPa, Proc. Combust. Inst. 33 (1) (2011) 577-84.
72. K.A. Thomson, D.R. Snelling, G.J. Smallwood, F. Liu, Laser induced incandescence measurements of soot volume fraction and effective particle size in a laminar co-annular non-premixed methane/air flame at pressures between 0.5–4.0 MPa, Appl. Phys. B 83 (3) (2006) 469-75.
73. A.C. Eckbreth. Laser diagnostics for combustion temperature and species: CRC press; 1996.
74. J.W. Daily, Laser induced fluorescence spectroscopy in flames, Prog. Energy Combust. Sci. 23 (2) (1997) 133-99.
75. K. Gabet, R. Patton, N. Jiang, W. Lempert, J. Sutton, High-speed CH 2 O PLIF imaging in turbulent flames using a pulse-burst laser system, Appl. Phys. B 106 (3) (2012) 569-75.

76. Z. Wang, P. Stamatoglou, Z. Li, M. Aldén, M. Richter, Ultra-high-speed PLIF imaging for simultaneous visualization of multiple species in turbulent flames, Optics express 25 (24) (2017) 30214-28.
77. A.M. Elbaz, W.L. Roberts, Experimental study of the inverse diffusion flame using high repetition rate OH/acetone PLIF and PIV, Fuel 165 (2016) 447-61.
78. Z. Li, B. Li, Z. Sun, X.-S. Bai, M. Aldén, Turbulence and combustion interaction: High resolution local flame front structure visualization using simultaneous single-shot PLIF imaging of CH, OH, and CH2O in a piloted premixed jet flame, Combust. Flame 157 (6) (2010) 1087-96.
79. F. Beretta, V. Cincotti, A. D'alessio, P. Menna, Ultraviolet and visible fluorescence in the fuel pyrolysis regions of gaseous diffusion flames, Combust. Flame 61 (3) (1985) 211-8.
80. I. Berlman. HANDBOOK OF FLUORESCENCE SPECTRA OF AROMATIC MOLECULES. 1971; 1971.
81. A. Ciajolo, R. Ragucci, B. Apicella, R. Barbella, M. De Joannon, A. Tregrossi, Fluorescence spectroscopy of aromatic species produced in rich premixed ethylene flames, Chemosphere 42 (5-7) (2001) 835-41.
82. A. Ciajolo, A. Tregrossi, R. Barbella, R. Ragucci, B. Apicella, M. De Joannon, The relation between ultraviolet-excited fluorescence spectroscopy and aromatic species formed in rich laminar ethylene flames, Combust. Flame 125 (4) (2001) 1225-9.
83. P. Liu, Z. He, G.-L. Hou, B. Guan, H. Lin, Z. Huang, The diagnostics of laser-induced fluorescence (LIF) spectra of PAHs in flame with TD-DFT: special focus on five-membered ring, The Journal of Physical Chemistry A 119 (52) (2015) 13009-17.
84. L. Sgro, P. Minutolo, G. Basile, A. D'Alessio, UV-visible spectroscopy of organic carbon particulate sampled from ethylene/air flames, Chemosphere 42 (5-7) (2001) 671-80.
85. Y. Zhang, Y. Li, L. Wang, P. Liu, R. Zhan, Z. Huang, H. Lin, Investigation on the LIF spectrum superposition of gas-phase PAH mixtures at elevated temperatures: potential for the analysis of PAH LIF spectra in sooting flames, Appl. Phys. B 125 (5) (2019) 72.
86. F. Ossler, T. Metz, M. Aldén, Picosecond laser-induced fluorescence from gas-phase polycyclic aromatic hydrocarbons at elevated temperatures. I. Cell measurements, Appl. Phys. B 72 (4) (2001) 465-78.
87. A. Ciajolo, R. Barbella, A. Tregrossi, L. Bonfanti, editors. Spectroscopic and compositional signatures of PAH-loaded mixtures in the soot inception region of a premixed ethylene flame. Symposium (International) on Combustion; 1998: Elsevier.
88. S. Lee, S. Yoon, S. Chung, Synergistic effect on soot formation in counterflow diffusion flames of ethylene–propane mixtures with benzene addition, Combust. Flame 136 (4) (2004) 493-500.
89. L. Petarca, F. Marconi, Fluorescence spectra and polycyclic aromatic species in a n-heptane diffusion flame, Combust. Flame 78 (3-4) (1989) 308-25.

90. G. Zizak, F. Cignoli, G. Montas, S. Benecchi, R. Donde, Detection of aromatic hydrocarbons in the exhaust gases of a gasoline ic engine by laser-induced fluorescence technique, Rec. Res. Dev. Appl. Spectrosc 1 (1996) 17-24.
91. N.-E. Olofsson, J. Johnsson, H. Bladh, P.-E. Bengtsson, Soot sublimation studies in a premixed flat flame using laser-induced incandescence (LII) and elastic light scattering (ELS), Appl. Phys. B 112 (3) (2013) 333-42.
92. V. Sick, High speed imaging in fundamental and applied combustion research, Proc. Combust. Inst. 34 (2) (2013) 3509-30.
93. M. Hartmann: Light scattering by small particles. By HC van de Hulst. New York (John Wiley and Sons), London (Chapman and Hall); 1957.
94. S. Lonn, A. Matamis, M. Tuner, M. Richter, O. Andersson. Optical study of fuel spray penetration and initial combustion location under PPC conditions. SAE Technical Paper; 2017. Report No.: 0148-7191.
95. C.E. Dumitrescu, A. Cheng, E. Kurtz, C.J. Mueller, A Comparison of Methyl Decanoate and Tripropylene Glycol Monomethyl Ether for Soot-Free Combustion in an Optical Direct-Injection Diesel Engine, Journal of Energy Resources Technology 139 (4) (2017).
96. C.E. Dumitrescu, C.J. Mueller, E. Kurtz, Investigation of a tripropylene-glycol monomethyl ether and diesel blend for soot-free combustion in an optical direct-injection diesel engine, Applied Thermal Engineering 101 (2016) 639-46.
97. J. Manin, S. Skeen, L. Pickett, E. Kurtz, J.E. Anderson, Effects of oxygenated fuels on combustion and soot formation/oxidation processes, SAE International Journal of Fuels and Lubricants 7 (3) (2014) 704-17.
98. C.J. Mueller, G.C. Martin, Effects of oxygenated compounds on combustion and soot evolution in a DI diesel engine: broadband natural luminosity imaging, SAE Transactions (2002) 518-37.
99. S.A. Self, Focusing of spherical Gaussian beams, Appl. Opt. 22 (5) (1983) 658-61.
100. S. Balusamy, M.M. Kamal, S.M. Lowe, B. Tian, Y. Gao, S. Hochgreb, Laser diagnostics of pulverized coal combustion in O 2/N 2 and O 2/CO 2 conditions: velocity and scalar field measurements, Experiments in Fluids 56 (5) (2015) 108.
101. M. Köhler, K. Geigle, W. Meier, B. Crosland, K. Thomson, G. Smallwood, Sooting turbulent jet flame: characterization and quantitative soot measurements, Appl. Phys. B 104 (2) (2011) 409-25.
102. W. Lee, Y.D. Na, Soot study in laminar diffusion flames at elevated pressure using two-color pyrometry and Abel inversion, JSME Int. J. Ser. B 43 (4) (2000) 550-5.
103. A.E. Karataş, Ö.L. Gülder, Soot formation in high pressure laminar diffusion flames, Prog. Energy Combust. Sci. 38 (6) (2012) 818-45.
104. K.A. Thomson, Ö.L. Gülder, E.J. Weckman, R.A. Fraser, G.J. Smallwood, D.R. Snelling, Soot concentration and temperature measurements in co-

annular, nonpremixed CH4/air laminar flames at pressures up to 4 MPa, Combust. Flame 140 (3) (2005) 222-32.
105. D.R. Snelling, K.A. Thomson, G.J. Smallwood, -Oslash, L. G-uacute, lder, E. Weckman, R. Fraser, Spectrally resolved measurement of flame radiation to determine soot temperature and concentration, AIAA journal 40 (9) (2002) 1789-95.
106. D.R. Snelling, K.A. Thomson, G.J. Smallwood, Ö.L. Gülder, Two-dimensional imaging of soot volume fraction in laminar diffusion flames, Appl. Opt. 38 (12) (1999) 2478-85.
107. H.P. Nielsen, F. Frandsen, K. Dam-Johansen, L. Baxter, The implications of chlorine-associated corrosion on the operation of biomass-fired boilers, Prog. Energy Combust. Sci. 26 (3) (2000) 283-98.
108. R.K. Sharma, M.R. Hajaligol, Effect of pyrolysis conditions on the formation of polycyclic aromatic hydrocarbons (PAHs) from polyphenolic compounds, Journal of Analytical and Applied Pyrolysis 66 (1-2) (2003) 123-44.
109. J. Simonsson, N.-E. Olofsson, H. Bladh, M. Sanati, P.-E. Bengtsson, Influence of potassium and iron chloride on the early stages of soot formation studied using imaging LII/ELS and TEM techniques, Proc. Combust. Inst. 36 (1) (2017) 853-60.
110. J. Simonsson, N.-E. Olofsson, A. Hosseinnia, P.-E. Bengtsson, Influence of potassium chloride and other metal salts on soot formation studied using imaging LII and ELS, and TEM techniques, Combust. Flame 190 (2018) 188-200.
111. Y.-L. Wei, Effect of potassium hydroxide on PAH formation during toluene incineration, Chemosphere 37 (3) (1998) 509-21.
112. B. Haynes, H. Jander, H.G. Wagner, editors. The effect of metal additives on the formation of soot in premixed flames. Symposium (international) on Combustion; 1979: Elsevier.
113. J. Happold, (Auth.), H.-H. Grotheer, (Auth.), M. Aigner, (Auth.), H. Bockhorn, (Editor) , A. D'Anna, (Editor) , A.F. Sarofim, (Editor). Combustion generated fine carbonaceous particles. Wang H, editor: Universitätsverlag Karlsruhe; 2009.
114. A. Bach-Oller, E. Furusjö, K. Umeki, On the role of potassium as a tar and soot inhibitor in biomass gasification, Applied Energy 254 (2019) 113488.
115. M. Cristofaro, W. Edelbauer, P. Koukouvinis, M. Gavaises, A numerical study on the effect of cavitation erosion in a diesel injector, Applied Mathematical Modelling 78 (2020) 200-16.
116. S. d'Ambrosio, A. Ferrari, Diesel injector coking: optical-chemical analysis of deposits and influence on injected flow-rate, fuel spray and engine performance, Journal of engineering for gas turbines and power 134 (6) (2012).
117. A. Magno, E. Mancaruso, B.M. Vaglieco, S. Florio, G. Gioco, E. Rebesco. Study on spray injection and combustion of fouled and cleaned injectors by means of 2-D digital imaging in a transparent CR diesel engine. SAE Technical Paper; 2013. Report No.: 0148-7191.

118. P. Richards, R. Walker, D. Williams. Fouling of two stage injectors-an investigation into some causes and effects. SAE Technical Paper; 1997. Report No.: 0148-7191.
119. R. Payri, P. Martí-Aldavarí, T. Montiel, A. Viera, Influence of aging of a diesel injector on multiple injection strategies, Applied Thermal Engineering 181 (2020) 115891.
120. M.A. González D, W. Piel, T. Asmus, W. Clark, J. Garbak, E. Liney, M. Natarajan, D.W. Naegeli, D. Yost, E.A. Frame, Oxygenates screening for AdvancedPetroleum-Based Diesel Fuels: Part 2. The Effect of Oxygenate Blending Compounds on Exhaust Emissions, SAE Transactions (2001) 2246-55.
121. X.D. Zhu, M. Mannazhi, N. Palazzo, P.E. Bengtsson, O. Andersson, High-Speed Imaging of Spray Formation and Combustion in an Optical Engine: Effects of Injector Aging and TPGME as a Fuel Additive, Energies 13 (12) (2020).

Printed by Media-Tryck, Lund 2021 NORDIC SWAN ECOLABEL 3041 0903

Faculty of Engineering
Department of Physics
Division of Combustion Physics

Lund Reports on Combustion Physics: LRCP-230
ISRN LUTFD2/TFCP-230-SE
ISBN 978-91-7895-847-4
ISSN 1102-8718